Computational Studies of Catalytic Organic and Bioorganic Reactions

by

Yue Fu

B.Sc, Nankai University, 2016

M.Sc, University of Pennsylvania, 2019

Submitted to the Graduate Faculty of the

Dietrich School of Arts and Sciences in partial fulfillment

of the requirements for the degree of

Doctor of Philosophy

University of Pittsburgh

2022

UNIVERSITY OF PITTSBURGH

DIETRICH SCHOOL OF ARTS AND SCIENCES

This dissertation was presented

by

Yue Fu

It was defended on

August 2, 2022

and approved by

Kenneth Jordan, Richard King Mellon Professor and Distinguished Professor, University of Pittsburgh

Kabirul Islam, Assistant Professor, University of Pittsburgh

Olexandr Isayev, Assistant Professor, Carnegie Mellon University

Dissertation Director: Peng Liu, Associate Professor, University of Pittsburgh

Computational Studies of Catalytic Organic and Bioorganic Reactions

Yue Fu, PhD

University of Pittsburgh, 2022

Understanding reaction mechanisms, rationalizing reactivity and selectivity, and predicting new catalytic transformations are long-standing challenges for synthetic organic chemistry. To provide molecular level understanding of reaction mechanisms and catalyst effects, computational study has emerged as an effective approach. The use of computational methods in mechanistic studies is especially valuable in systems involving complex reaction pathways, reactive intermediates, strong solvent effects, and open-shell transition metal complexes, where experimental techniques for mechanistic investigations are relatively limited.

I applied various computational methods to investigate reaction mechanisms and factors controlling reactivity and selectivity in glycosylation reactions, silver catalyzed C−H amination reactions, and P450-catalyzed bioorganic reactions. In this dissertation (Chapter 2), I use the combination of *ab initio* molecular dynamics (AIMD) metadynamics and Born-Oppenheimer molecular dynamics (BOMD) trajectory simulations to provide metrics (energy, geometry, and timing) to describe the continuum of glycosylation mechanisms (S_N2, S_N2-like, S_Ni, S_N1-like, and S_N1). In Chapter 3, I apply systematic studies to evaluate the sensitivity of regioselectivity to different substrate properties (BDE, tether length, electronic effects, etc) in silver catalyzed C–H amination reactions. Finally, I report a computational study on the mechanism, reactivity, and enantioselectivity in the P450-catalyzed atom transfer radical cyclization (ATRC) (Chapter 4). I discovered a bifunctional biocatalyst, with the heme cofactor enabling atom transfer activity and the Q263 residue introduced in directed evolution serving as a critical hydrogen bond donor,

activating the substrate, and enhancing enantioselectivity. Computational insights derived from these studies were used to facilitate the synthesis of functionalized organic compounds and guide reaction design.

Table of Contents

List of Tables

List of Figures

Preface

I would like to thank my advisor, Prof. Peng Liu, for his guidance and support during my studies at Pitt.

I would like to thank the Andrew Mellon Fellowship for the financial support.

I would like to thank my parents for their love and support.

1.0 Introduction

Catalytic organic and bioorganic reactions are powerful strategies in chemical synthesis of functionalized organic compounds for biomedical and pharmaceutical research. Although tremendous progress has been made in the field of their synthetic methodology development, there are still several challenges that impede the design and discovery of better catalysts for their synthesis. One of the challenges is to elucidate factors that control regio- and stereoselectivity in transition metal-catalyzed reactions and enzyme-catalyzed asymmetric synthesis. This challenge is relevant in many types of reactions, including glycosylation reactions in carbohydrate chemistry,[1] C–H and alkene functionalization reactions.

The standard way of studying reaction mechanisms and selectivity is to use density functional theory (DFT) methods to calculate reaction pathways and produce energy profiles. The resulting reaction energy profiles can be used to identify preferred reaction mechanism, rate- and selectivity-determining steps, and to study ligand and substrate effects on reactivity and selectivity. However, there are several scenarios where this standard approach may be insufficient, including (a) when a reaction is strongly affected by explicit solvent effects that are challenging for commonly used implicit solvent model, (b) when selectivity is affected by a combination of multiple factors originated from the substrate and the catalyst, and (c) in enzyme catalysis because of the conformational flexibility and the size of the catalyst system.

My research focuses on addressing these challenges, including the reaction mechanisms and factors controlling stereoselectivity of glycosylation reaction, origin of the site selectivities for silver catalyzed C−H amination reactions, and the controlling factors for the enantioselectivity of P450-catalyzed bioorganic reactions. These studies involve the use of various computational

methods, including *ab initio* molecular dynamics (AIMD) simulations to study glycosylation reactions involving reactive oxocarbenium intermediates in explicit solvent, DFT calculations to study the reaction silver catalyzed C−H amination reaction mechanisms, coupled-cluster and multireference methods to study the electronic structure of silver complexes. Finally, I applied classical molecular dynamics (MD), hybrid quantum mechanics/molecular mechanics (QM/MM) calculations, and metadynamics simulations to study the mechanism and origin of enantioselectivity engineered P450 atom transfer radical cyclases.

Glycosylation reaction is a fundamental transformation involving carbohydrate molecules. It is extremely difficult to control the stereoselectivity of glycosylation reaction because the reaction outcome is highly sensitive to multiple factors (glycosyl donors, glycosyl acceptors, solvent, temperature, and activators, etc.) that ultimately affect the reaction mechanisms, which may shift within a continuum of S_N1- and S_N2-type mechanistic pathways (Figure 1-1). Experimentally, mechanistic information for glycosylation reactions can be obtained from the stereoselectivity of the products kinetic studies, kinetic isotopic effect (KIE) measurements,[2] and spectroscopic characterization, etc. Due to the practical challenges conducting certain experiments, the understanding of glycosylation mechanism is still lacking.

Previous computational studies were conducted to elucidate conformation and relative stability of oxocarbenium intermediates in solution,[3] transition state structures in glycosylation reactions, etc.[4] However, a general computational approach to reliably predict the mechanism of a given glycosylation reaction is currently still lacking.

In this dissertation (Chapter 2), I establish a protocol using the combination of AIMD metadynamics and Born-Oppenheimer molecular dynamics (BOMD) trajectory simulations to provide metrics (energy, geometry, and timing) to describe the types of glycosylation mechanisms

(S_N2, S_N2-like, S_Ni, S_N1-like, and S_N1) from different perspectives (the number of transition states along the reaction path, synchronicity of transition state structure, and lifetime of the oxocarbenium intermediate). Moreover, the combined metadynamics/BOMD approach will be broadly applied to investigate various glycosylation reactions, as well as other organic reactions involving reactive intermediates and strong solvent effects.

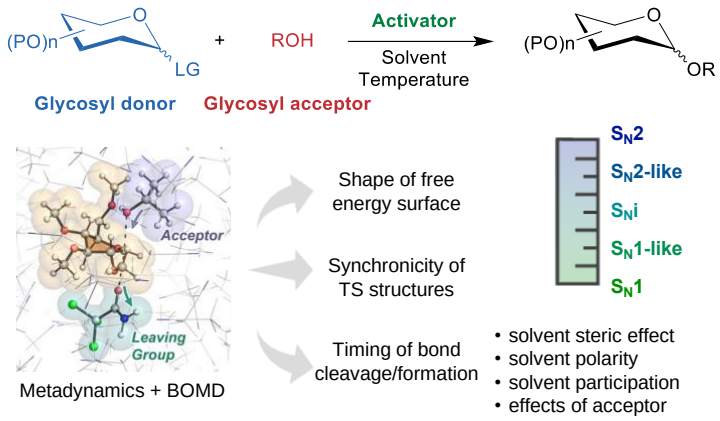

Figure 1-1 Factors that impact the stereochemistry of glycosylation reactions.

Various synthetic methodologies using transition metal catalyst to construct of C–N bond via nitrene transfer has been developed over the years.[5] Among those, the development of silver catalyzed C–H amination via nitrene transfer (NT) has attracted great interest. The diversity of ligands supporting the Ag catalysts results in a broad range of steric and electronic environment around the reacting center, and thus, offers opportunities to achieve catalyst-controlled regio- and enantioselectivities (Figure 1-2).

Numerous examples from Schomaker et al. have demonstrated the use of Ag catalysts for the regiodivergent C–H aminations.[6] Despite these successes, it is still challenging to develop Ag catalyst to effectively distinguish between C–H bonds with similar bond dissociation energies (BDE) and steric environments, override inherent substrate preference to favor a less reactive site, or activate inert C–H bonds. In addition, the reactivity is affected by the electronic,[7] steric,[8] and

tether length effects.[6b] The reaction development usually requires trial-and-error experimental optimization of multiple factors, including ancillary ligands, precursor,[9] counter anions, etc. The lack of thorough understanding the of the interplay of these experimental variables hinders the rational catalyst design for the tunable C–H bond amination.

In order to elucidate the origins of catalyst-controlled selectivity in the Ag-catalyzed regiodivergent C−H amination (Chapter 3), I used a unique computational approach to evaluate the sensitivity to different substrate properties (BDE, tether length, electronic effects, etc.) in reactions with four representative types of Ag nitrenes. These systematic studies on ligand and substrate effects provided a set of practical guidelines for rational selection of suitable ligand and precursor for selective C–H amination based on the properties of the target C–H bond. Through experimental validations, I demonstrated the effective use of these guidelines to realize regiodivergent amination of both β- and γ-aliphatic C–H bonds with similar steric and electronic properties.

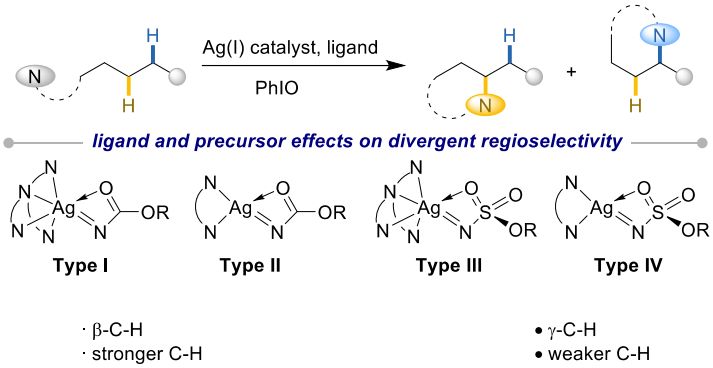

Figure 1-2 Catalyst controled regioselectivity for Ag catalyzed C-H amination via nitrene transfer.

New-to-nature radical biocatalysis has recently emerged as a powerful strategy to tame fleeting open-shell intermediates for stereoselective transformations. Laboratory evolved cytochromes P450 from the Yang group taking advantage of natural enzyme's exquisite stereocontrol and innate redox properties enable new-to-nature enantioselective atom-transfer

radical cyclization (ATRC) (Figure 1-3).[10] Because traditional approach using small-molecule catalysts can lead to the dissociation of the free radical intermediate, the effective stereoinduction of radical-mediated transformations are rare.[11-12] Thus, the enzymatic counterparts provide a new means of taming radical intermediates for a synthetically valuable but underdeveloped class of asymmetric transformations.

Experimentally, protein engineering induced mutants dramatically enhance reactivity and stereoselectivity. However, the active site residues responsible for the enhanced reactivity and enantioselectivity are still not clear. Moreover, the atomic scale simulations of enzymatic transition states and understanding the flexible and complex enzyme-substrate interactions are challenging.

In this dissertation (Chapter 4), I report a computational study on the mechanism, reactivity, and enantioselectivity in the P450-catalyzed atom transfer radical cyclization (ATRC). I discovered the unexpected role of a key glutamine residue (Q263) in enabling this unprecedented enzymatic transformation. Consequently, these previously evolved biocatalysts are bifunctional, with the heme cofactor enabling atom transfer activity and the Q263 residue introduced in directed evolution serving as a critical hydrogen bond donor, activating the substrate, and enhancing enantioselectivity.

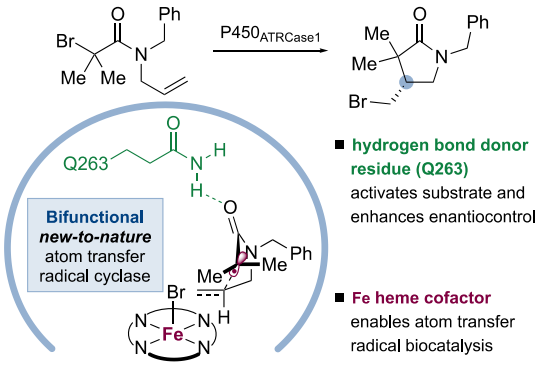

Figure 1-3 Bifunctional engineered P450 atom transfer radical cyclases.

2.0 Ab Initio Molecular Dynamics Simulations of the S_N1/S_N2 Mechanistic Continuum in Glycosylation Reactions

2.1 Introduction

Carbohydrates, the "essential molecule of life",[13] are essential constituents of living organisms and participate in nearly all biological processes. Glycosylation reaction is a fundamental transformation in biological systems to produce carbohydrate products. It involves a mono- or polysaccharide derivative acting as[14] an electrophile ("glycosyl donor") activated with a Lewis or Brønsted acid that couples to a nucleophile ("glycosyl acceptor") to form a C–O bond at the stereogenic anomeric carbon (Figure 2-1).

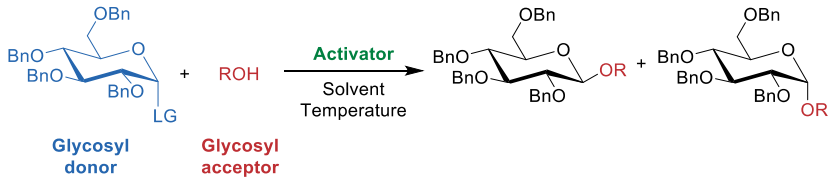

Figure 2-1 Glycosylation reactions.

Although intensive efforts have been directed toward the development of practical methods and strategies for oligo- and polysaccharide synthesis,[15] stereochemical control in the construction of glycosidic linkages remains challenging.[1a-b,15] Experimentally, stereoselectivity of glycosylation reactions is influenced by various factors including the permanent factors (glycosyl donors and glycosyl acceptors) and environmental favors (solvent, temperature, and activators) (Figure 2-2). For example, Seeberger[16] reported that the glycosylation of *i*-PrOH with glucosyl donor **2-1a** is stereoinvertive while the reaction of *i*-PrOH with mannosyl donor **2-1b** is stereoretentive, the stereoretentive product is favored when the acceptor is more steric hindered, while the polar solvent and lower temperature are in favor of producing stereoinvertive product (Figure 2-2), etc.

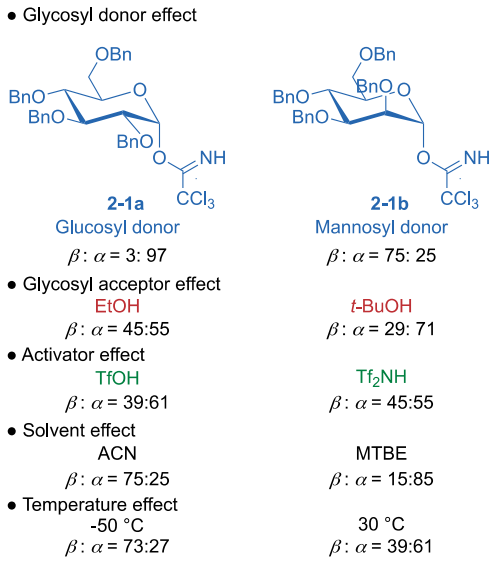

Figure 2-2 Effects of glycosyl donors, acceptors activators, solvent, and temperature on stereoselectivity of glycosylation reactions.

Rationalizing stereoselectivity of glycosylation reactions requires thorough understanding of the mechanisms (Figure 2-3), which is a long-standing challenge in carbohydrate chemistry. These reactions, which involve the nucleophilic substitution of a leaving group in a glycosyl donor with a glycosyl acceptor, can occur via a concerted S_N2 mechanism, a stepwise S_N1 mechanism involving oxocarbenium intermediates, or, in most cases, S_Ni mechanisms involving tightly or loosely associated ion-pairs.[17] There is extensive experimental evidence for the existence of a continuum of mechanisms spanning the two extreme S_N1 and S_N2 pathways, and that the actual mechanism of a given reaction is strongly affected by multiple factors, including the nature of the leaving group, glycosyl donor and acceptor, solvent, activator, and the reaction temperature.[16f,18] Because the mechanisms of glycosylation directly impact the reaction stereospecificity, insights into how these factors promote the concertedness of the reaction can provide useful guidelines for the development of stereoselective glycosylation reactions.

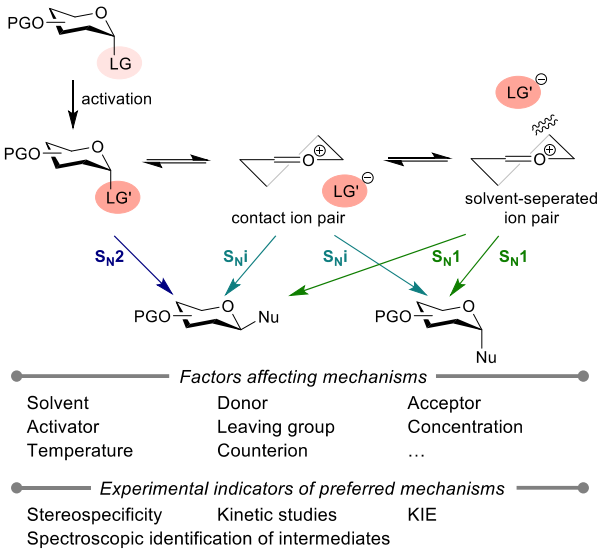

Figure 2-3 Glycosylation mechanisms.

Experimentally, mechanistic information for glycosylation reactions may be obtained from the stereoselectivity of the products, as the S_N2 pathway leads to stereoinversion while the S_N1 pathway can lead to a mixture of two anomers. In addition, kinetic studies, kinetic isotopic effect (KIE) measurements,[2] and attempts to observe glycosyl oxocarbenium intermediates via spectroscopic methods can be used to reveal a number of mechanistic details. These experimental studies present a number of practical challenges, including, for instance, the synthesis of isotopically labeled molecules for KIE measurements.

Computational studies have been used to elucidate the conformation and relative stability of oxocarbenium intermediates in solution (Figure 2-4).[3] Although only a few of them have addressed specifically transition state structures in glycosylation reactions,[4, 19] predicting the stability of oxocarbenium ion in the S_N1 pathways is more challenging because of the strong solvation effect and the effects of the counterion (i.e. leaving group). A general computational approach to reliably predict the mechanism of a given glycosylation reaction within the S_N1/S_N2 continuum is currently still lacking.

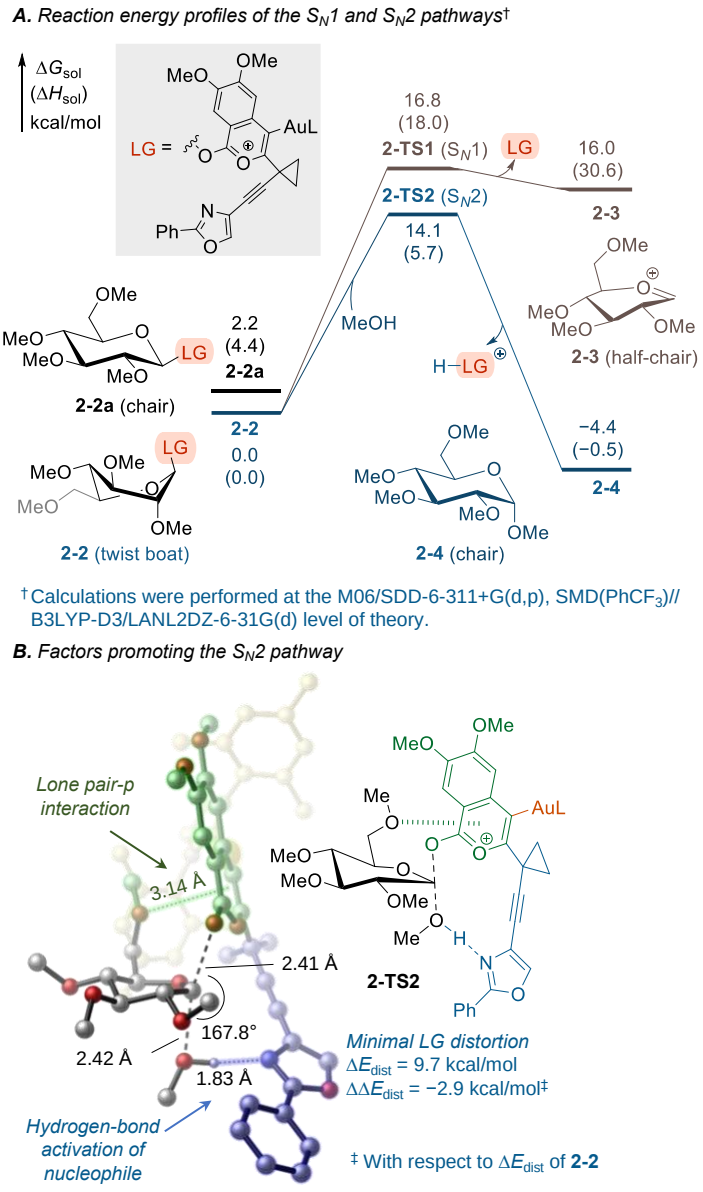

Figure 2-4 Computational mechanistic studies.

Most of the challenges encountered in the computational modeling of glycosylation pathways are associated with the difficulty of describing solvation effects in transition state calculations.[20] Although the widely used continuum polarization models (e.g. SMD, CPCM, etc.) provide reasonable energetics for most reactions in organic solvents,[21] they fail to account for the energy difference of competing SN1/SN2 glycosylation pathways, particularly in situations in which the solvent plays a non-innocent role on the reactivity.[22] The reactivity and stability of the

putative oxocarbenium ion intermediate can be affected not only by electrostatic interactions, but also by the presence of hydrogen bonds and even covalent interactions with solvent molecules.[14b,23]

In this work, we use AIMD simulations, with an explicit molecular treatment of both reactants and solvent, to address these fundamental challenges in the modeling of glycosylation mechanisms. AIMD[24] simulations propagate dynamical trajectories using forces computed with quantum mechanical methods such as DFT. Thus, AIMD can be used to investigate time-resolved mechanisms involving chemical bond breaking, bond forming, and charge transfer events, which are challenging for classical MD simulations. AIMD has been successfully applied to simulate microscopic physical, chemical, and biological processes and has been proven to be very effective in elucidating reaction mechanisms in condense phase.

AIMD simulations performed with an explicit solvent provide a realistic description of both non-covalent and bonding interactions between solvent and solute and their evolution in time.[25] They also provide explicit information about the entropic contribution to free energy profiles (which can be calculated using approaches for rare events,[26] including metadynamics[27]), which are not limited to harmonic oscillator approximations. AIMD simulations can therefore be applied to the prediction of geometries and conformations of intermediates and transition states,[25a,b] free energy surfaces,[26a,b] timing of bond formation/cleavage, and lifetime of intermediates in complex environments, and they can in principle provide quantitative metrics, in the case of glycosylation reactions, to describe the reaction character within the S_N1/S_N2 continuum (Figure 2-5).

Metadynamics[28] is an enhanced sampling method that biased potentials are added to the system to allow for the system to escape minima in order to sample the rest of the free energy surface on a time scale that is accessible by present day computers. The metadynamics approach

is capable of exploring the free-energy surface without prior information about the location of minima or transition states. This technique has been successfully applied to study chemical reactions that take place in condensed phase.

The primary goal of this work is to explore the potential of AIMD-based methods to characterize the nature of glycosylation reactions with different substrates in different solvent environments, and how, in turn, the mechanisms affect the stereospecificity of the reaction. We investigate the glycosylations of a glucosyl trichloroacetimidate donor reacting with different alcohol acceptors in different organic solvents, a reaction that has been extensively studied experimentally by Seeberger.[16] We show that the profile of the free energy surface at reaction temperature, the synchronicity of the transition state structure (*i.e.* the difference between the cleaving and forming bond lengths), and the time-gap between leaving group dissociation and nucleophile association can be used as three complementary indicators to distinguish between S_N1- and S_N2-like mechanisms. The chapter is organized as follows. First, we demonstrate the computational procedures to perform AIMD metadynamics and BOMD trajectory simulations from transition state structures of the glucosyl trichloroacetimidate donor reacting with *i*-PrOH in acetonitrile (ACN). Then, we carry out the same AIMD calculations for reactions in other solvents and with other alcohol acceptors to investigate how these variations affect the reaction mechanisms. Finally, we establish a set of quantitative metrics that can be used to describe the reaction mechanisms within the S_N1/S_N2 continuum.

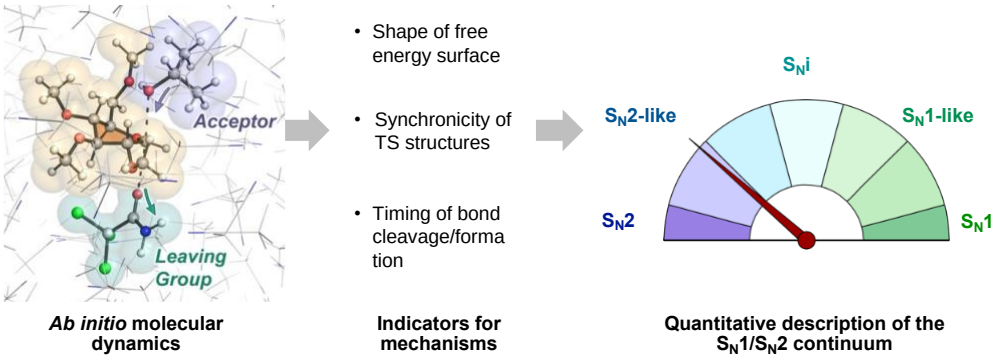

Figure 2-5 Computationally derived quantitative metrics for characterizing mechanisms.

2.2 Computational Methods

2.2.1 Density Functional Theory (DFT) Calculations

DFT is a widely used quantum mechanical method in computational chemistry to investigate the mechanisms of glycosylation reactions. Various DFT methods have been developed for geometry optimizations of ground state and transition state structures as well as property and energy calculations. To balance accuracy and cost, in this work, I applied the dispersion-corrected Perdew-Burke-Ernzerhof (PBE)[29] functional, which is known to give satisfactory accuracy on modeling organic systems[30] with low computational cost to study the mechanisms of glycosylation reactions.

All DFT calculations were performed on Pitt CRC, TACC, and XSEDE[31] supercomputers. To compare the transition state structures obtained from gas-phase and implicit solvation model calculations to those from the AIMD simulations in explicit solvent, we performed DFT calculations using the Gaussian 16 software package[32] to study the static transition state structures optimized in the gas phase at the PBE-D3/6-311+G(d,p)//PBE-D3/6-31G(d) level of theory and in

implicit solvation using the SMD continuum solvation model at the PBE-D3/6-311+G(d,p), SMD (ACN)//PBE-D3/6-31G(d) level of theory. The reported Gibbs free energies and enthalpies in solution include thermal corrections computed at 298 K at the standard concentration (1 mol/L) using GoodVibes.[33] The 3D images of optimized structures were prepared using CYLView.[34]

2.2.2 CREST/GFN2-xTB Conformational Sampling

Conformer–Rotamer Ensemble Sampling Tool (CREST) is a conformer sampling algorithm based on iterative metadynamics and extensive MD sampling to generate conformer–rotamer ensembles[35] followed by geometry optimization and electronic energy calculation using the semiempirical tight-binding based quantum chemistry method, GFN2-xTB.[36] I applied CREST/GFN2-xTB to generate input structures for DFT calculations of conformationally flexible glycosyl intermediates and transition states.

The conformational sampling was performed by constraining the C^1–O^{LG} and C^1–O^{Nu} bond distances at the transition state geometry (2.18 and 2.73 Å, respectively, for TS geometries optimized in the gas-phase; 2.14 and 2.70 Å, respectively, for TS geometries optimized in implicit solvation model) with a force constant of 0.5 hartree/bohr².[37] The conformational sampling of transition states leads to 395 unique conformers in gas phase and 312 unique conformers in implicit acetonitrile. The structures obtained from conformational sampling were further optimized without constraints at the DFT level.

2.2.3 AIMD Simulations

AIMD runs were performed using the QUICKSTEP module of the CP2K package.[38] The liquid solution structure was modeled using an orthorhombic periodic cell of dimensions 20.0 Å × 16.0 Å × 16.0 Å, containing 49 acetonitrile (ACN) molecules. In the simulations in dichloromethane (DCM) and methyl *tert*-butyl ether (MTBE) solvents, the periodic cell contains 44 DCM and 21 MTBE molecules, respectively. The box dimension was chosen to correspond to the density of pure ACN (0.786 g/cm^3), DCM (1.327 g/cm^3), and MTBE (0.740 g/cm^3), respectively. Atomic forces were estimated using DFT calculations with the PBE exchange-correlation functional.[29a] The Kohn-Sham orbitals were described with hybrid Gaussian/plane-wave basis functions.[39] DZVP basis sets[40] and Goedecker-Teter-Hutter pseudopotentials[41] were employed for all atoms. The auxiliary plane-wave basis set was expanded up to a 280 Ry cutoff. The Grimme D3 approximation was used to describe dispersion forces.[29b] A convergence of 10^{-5} hartree was imposed for the ground state energy. The atomic positions were propagated using the BOMD scheme[42] with a time-step of 0.5 fs. The simulation temperature was controlled through a Nosé-Hoover thermostat[43] with a time constant of 1 ps.

2.2.4 Free Energy Calculations with Metadynamics

Metadynamics simulations were performed at 298 K to obtain the free energy profile for a given glycosylation process.[44] We used coordination numbers (CNs),[45] given by $CN = [1 - (d/d_0)^6]/[1 - (d/d_0)^{12}]$, where d is the distance between two atoms and d_0 is a reference distance (2.5 Å), as collective variables. The first collective variable, CN1, follows the bond breaking between the anomeric carbon in the pyranose ring (C^1) and the oxygen atom on the

trichloroacetimidate leaving group (O^{LG}). The second collective variable, CN2, follows the bond formation between C^1 and the oxygen atom on the nucleophile (i.e. the alcohol acceptor) (O^{Nu}). Repulsive Gaussian-shaped potential hills with a height of 0.3 kcal/mol and a width of 0.1 were added to the potential every 50 molecular dynamics steps for the two collective variables.

2.2.5 BOMD Trajectory Simulations

This approach, similar to the methods described in prior computational studies,[46] was used to estimate decay rates of intermediates or transition states in the course of the reaction. BOMD trajectory simulations, as one type of AIMD simulations, were carried out with CP2K/QUICKSTEP, using the same computational parameters used in the metadynamics simulations. Trajectory propagation was initialized at stationary points (S_N2 transition states in concerted pathways and oxocarbenium intermediates in stepwise S_N1 pathways) determined from metadynamics simulations. The simulation temperature (298 K) was controlled through a Nosé-Hoover thermostat. Stationary points with different solvent configurations were obtained by equilibrating the system with the C^1–O^{LG} and C^1–O^{Nu} distances constrained at the corresponding bond lengths. After a preliminary equilibrium of 3 ps, structures and velocities were extracted from the equilibrating system at intervals of 0.1 ps and propagated with no constraints.

2.2.6 Solvent/solute Interaction Energies

Solvent/solute interaction energies ($\Delta E_{\text{sol-interaction}}$)[47] were calculated at the PBE-D3/6-311+G(d,p) level of theory according to the equation $\Delta E_{\text{sol-interaction}} = E_{\text{box}} - E_{\text{solvent}} - E_{\text{solute}}$, where E_{box} is the electronic energy of the solvation box, E_{solvent} and E_{solute} are the electronic energies of

solvent molecules and solute in the same geometries as those in the solvation box (Figure 2-6). The geometries of the solute and solvent molecules in the solvation box were relaxed with constraining the C^1–O^{LG} and C^1–O^{Nu} bond distances. Geometry relaxations were carried out with CP2K/QUICKSTEP, using the same computational parameters used in the AIMD simulations. $\Delta E_{\text{sol-interaction}}$ was calculated from the average of five snapshots from an equilibrating AIMD run. A more negative $\Delta E_{\text{solvation}}$ indicates greater stabilizing interactions between the solute and the solvent.

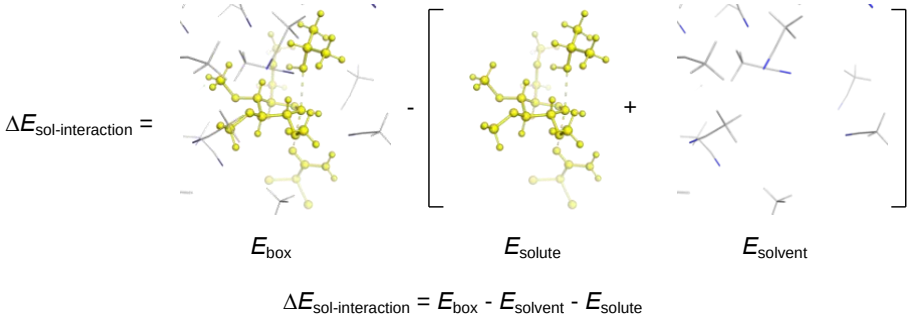

Figure 2-6 Solvent/solute interaction energies in different explicit solvents.

2.3 Results and Discussion

2.3.1 Free Energy Surface Calculations

To establish a general computational approach to describe the concertedness of glycosylation reactions, we first performed AIMD simulations of the glycosylation of a fully methylated glucosyl α-trichloroacetimidate (TCA) donor **2-5**[48] and *i*-PrOH as the acceptor in explicit ACN solvent. This model reaction was chosen because TCA is one of the most widely used leaving groups in glycosylations. Factors affecting the stereoselectivity of reactions with

TCA-substituted glucosyl donor **2-5** have been carefully examined experimentally by Seeberger (Table 2-1).[16] The reaction of **2-5** and *i*-PrOH in ACN favors the stereoinverted β product with a 75:25 ratio, while the reaction favors the stereoretentive α product in DCM and MTBE. Because both β and α products can be formed via the S_N1 pathway, it is unclear whether the observed variations of stereoselectivity are due to a shift from an S_N2-like to an S_N1-like mechanism.

Table 2-1 Experimental stereoselectivity of the glycosylation reaction of glucosyl α-trichloroacetimidate 2-5 with alcohol acceptors.[16]

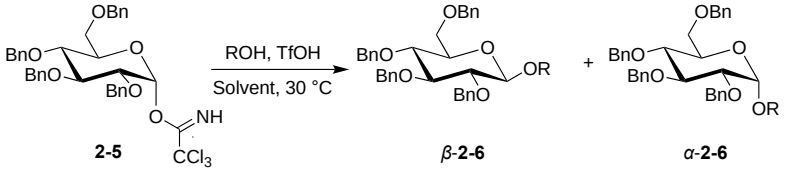

2-5 *β*-**2-6** *α*-**2-6**

Entry	Solvent	Acceptor (ROH)	Yield (%)[a]	*β*-**2-6** : *α*-**2-6**[a]
1	ACN	*i*-PrOH	76	75:25
2	DCM	*i*-PrOH	82	39:61
3[b]	DCM	*i*-PrOH	76	45:55
4[b]	DCM	EtOH	82	55:45
5	DCM	*t*-BuOH	81	29:71
6	MTBE	*i*-PrOH	65	15:85

[a] All experimental results were reported in ref. 16. Experiments were performed with **2-5** (10 mM, 1.2 equiv), acceptor (1 equiv), and TfOH (0.2 equiv) as activator. [b]Reactions were activated using $HNTf_2$ (0.2 equiv).

Low temperature NMR studies from Pedersen and coworkers have revealed that the protonated TCA donor is the active complex and non-nucleophilic conjugate anions in the activator (e.g. NTf_2^-) do not participate in the reaction.[49] Therefore, we carried out metadynamics simulations using the *N*-protonated acetimidate **2-7** in an ACN solvent box[50] in the absence of a counterion.[51] The initial configuration for the AIMD simulations was determined by equilibrating **2-7** and an *i*-PrOH molecule separated by 4.0 Å in the solvent box. In the metadynamics simulations, we introduced a bias potential on the coordination number following the cleaving of C^1–O^{LG} and the formation C^1–O^{Nu} bonds, which were used as collective variables (Figure 2-7). A bias potential was added gradually to allow the entire free energy surface (FES), including the transition state and product regions, to be sampled during the simulation. Therefore, this enhanced

sampling method allows for exploring the glycosylation reaction pathways without prior knowledge of the landscape of the FES.[52]

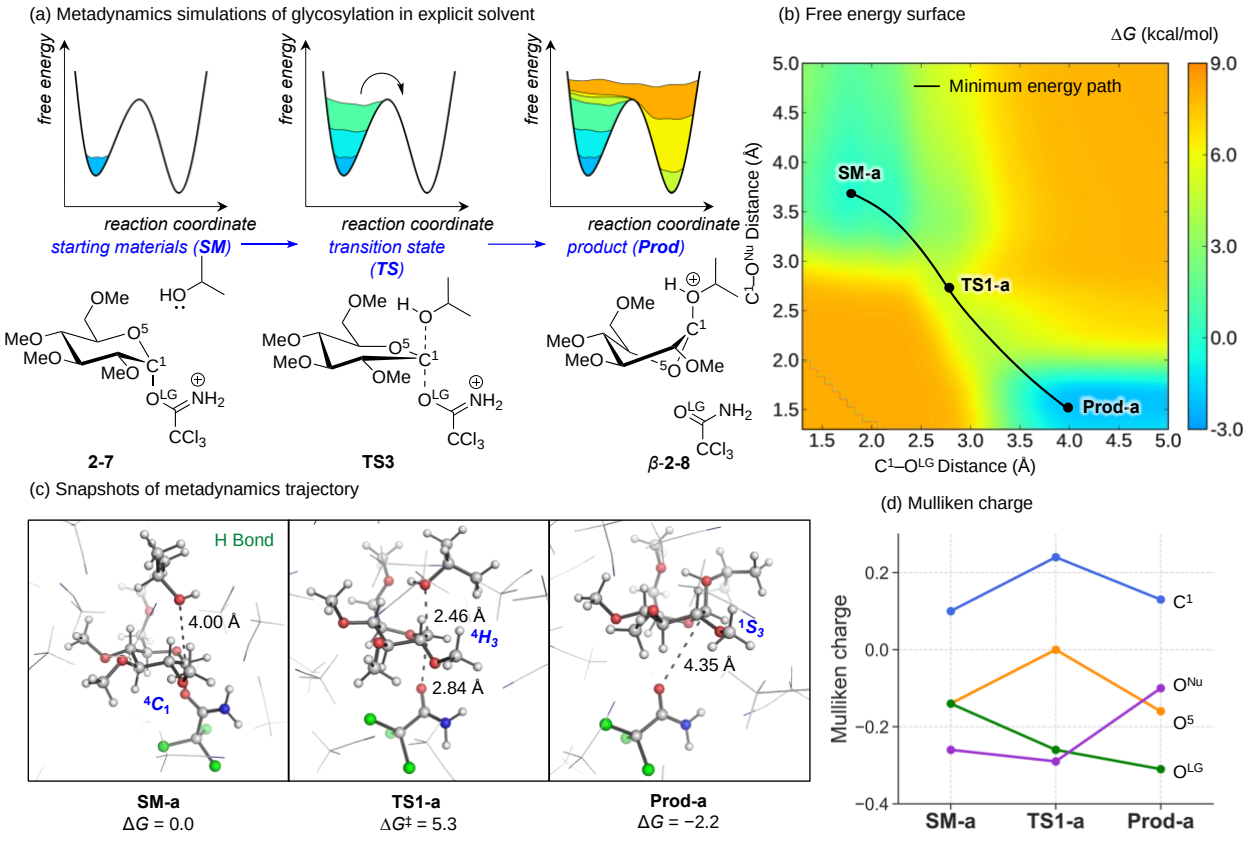

Figure 2-7 AIMD metadynamics simulations of the glycosylation of 2-7 and isopropanol in ACN.

The FES obtained using this procedure is shown in Figure 2-7b and it is consistent with a concerted S_N2 reaction path. The S_N2 transition state (**TS1-a**) has an activation free energy of 5.3 kcal/mol with respect to the activated donor (**SM-a**). The minimum energy path (MEP) on the surface indicates that the C^1–O^{LG} bond cleavage and the C^1–O^{Nu} bond formation occur synchronously without formation of an oxocarbenium intermediate.

Representative snapshots of structures in the regions of the activated donor starting materials (**SM-a**), S_N2 transition state **TS1-a**, and alkyloxonium ion product (**Prod-a**) in the metadynamics trajectory are shown in Figure 2-7c. In **TS1-a**, both the cleaving and forming C–O bonds are relatively long (2.84 and 2.46 Å for C^1–O^{LG} and C^1–O^{Nu}, respectively)[53] and the

pyranose ring adopts a $^4H_3$ (half-chair) conformation. These structural features are consistent with a loose transition state that has been proposed based on experimental ^{13}C KIEs of concerted S_N2 reactions of glycosides.[54] On the other hand, DFT-optimized S_N2 transition states in the gas phase and with an implicit solvation model (SMD) both significantly underestimate the C−O bond distances and lead to more compact transition state structures (Figure 2-8).

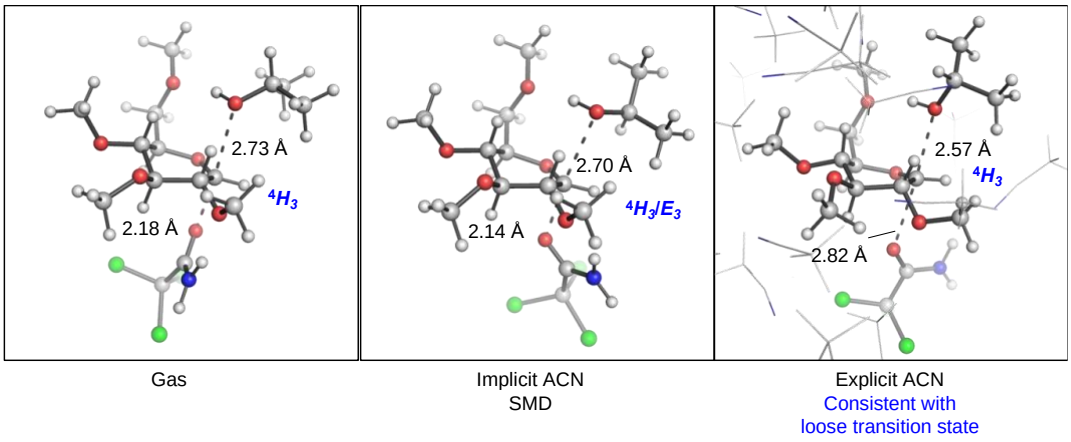

Figure 2-8 3D structures of the most stable transition state structures located in the gas phase, using the SMD implicit solvation model in ACN solvent, and from the metadynamics simulations in explicit ACN solvent.

Monitoring the charge transfer along the S_N2 path can shed light onto the role of solvent effects in the stabilization of the transition state. The computed Mulliken charges (Figure 2-7d) indicate that both the anomeric carbon (C^1) and the endocyclic oxygen (O^5) are noticeably more positively charged in **TS1-a** than those in the reactant and the product. The charge of the oxygen atoms on the nucleophile (O^{Nu}) and on the leaving group (O^{LG}) in **TS1-a** are comparable to those in the reactant and product, respectively. These atomic charges are consistent with an oxocarbenium character in the S_N2 transition state. Therefore, the polar ACN solvent is expected to stabilize the partial positive charge accumulating on the anomeric C atom (see later for a detailed analysis of solvent/solute interactions and of the effects of varying the solvent).

In addition to the electrostatic effects of the solvent, hydrogen bonding interactions between the trichloroacetamide leaving group and ACN solvent molecules are observed during the reaction (Figure 2-7c). These hydrogen bonds promote the departure of the leaving group at the transition state. Because solute-solvent hydrogen bonds are absent in calculations in the gas phase and in implicit solvent, these calculations overestimated the strengths of the *intra*molecular hydrogen bonds between the leaving group and O^2 and between the incoming nucleophile and O^6 and predicted much earlier transition state structures than the explicit solvation calculations.

We also performed metadynamics calculations for the FES of the S_N1-type dissociation of the leaving group from the activated glucosyl donor **2-7** in explicit ACN (Figure 2-9). In these calculations, the AIMD simulations were performed in the absence of the alcohol acceptor, using the C^1–O^{LG} distance as a collective variable. This S_N1 pathway (**S_N1-TS**, $\Delta G^{\ddagger}$ = 5.9 kcal/mol) requires a slightly higher energy barrier than the S_N2 transition state (**TS1-a**). These results indicate that although the S_N2-type mechanism is more favorable for this reaction, the competing S_N1-type pathway cannot be completely ruled out, especially at low acceptor concentrations. The relatively low activation energy difference between the S_N1 and S_N2 pathways is consistent with the moderate stereoselectivity (75:25) observed in experiment. [16]

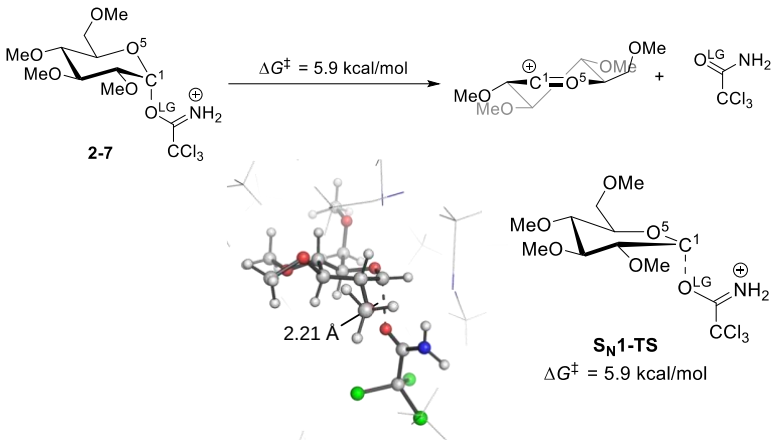

Figure 2-9 Metadynamics simulations of the activation free energies of the leaving group dissociation of 2-7 in the absence of acceptors.

2.3.2 Estimating Time-gaps between Bond Cleavage and Bond Formation

BOMD simulations are a powerful approach to obtain insights into time-resolved reaction mechanisms.[55] They have been used to study the concertedness of cycloaddition reactions by evaluating the time-gap between two bond formation events[56] and the lifetime of putative reactive intermediates. Reactions with smaller than 60 fs time-gap, such as simple Diels-Alder reactions, have been referred to as "dynamically concerted" and those with longer time-gaps as "dynamically stepwise".[46b-d] To date, BOMD simulations have yet to be performed to study mechanisms of glycosylation reactions. A significant challenge for the BOMD simulations is the computational cost associated with including explicit solvent molecules in the trajectory calculations. Albeit highly time-depending, explicit solvation is expected to be essential in the proper treatment of solvation effects.[55f,g,57] In this study, we performed BOMD simulations using the CP2K software to study the time-resolved glycosylation mechanisms in explicit solvents (Figure 2-10). These BOMD simulations are expected to reveal the timing of leaving group dissociation versus nucleophile attack, to provide estimates of the lifetime of the putative oxocarbenium intermediates,

and to give insights into the potential solvent participation in the reaction and into the conformational change of the pyranose ring along the reaction trajectory.[58] In our simulations, the entire system, including the solute and all solvent molecules, was treated using DFT. The BOMD trajectories were initiated by sampling the geometry and velocity of transition state structures and solvent molecules obtained from snapshots of a pre-equilibrated 3ps AIMD simulation with the C^1–O^{LG} and C^1–O^{Nu} distances constrained at 2.83 Å and 2.56 Å, respectively. These distances are determined from the transition state structure (**TS1-a**) obtained from metadynamics simulations (*vide supra*). From these initial saddle point geometries, 77 independent BOMD trajectories were propagated without constraints. In all initial geometries, the pyranose ring adopts the $^4H_3$ (half-chair) conformation. Within 1 ps, all of the propagating trajectories form either the starting materials (**SM-a**) with a $^4C_1$ (chair) conformation (37 of the 77 trajectories) or the alkyloxonium ion product (**Prod-a**) with the pyranose ring in the $^1S_3$ (skew boat) conformation (40 of the 77 trajectories).[59]

To estimate the time-gap between the bond cleavage and bond formation events, we calculated the median time from the C^1–O^{LG} bond cleavage (defined by the time when the C^1–O^{LG} distance becomes longer than 2.3 Å) to the transition state (124 fs) and the median time from the transition state to C^1–O^{Nu} bond formation (defined by the time when the C^1–O^{Nu} distance becomes shorter than 2.3 Å) (114 fs). We define the time to traverse the "transition zone" as the time between the C^1–O^{LG} bond cleavage and C^1–O^{Nu} bond formation events. The median time to traverse the transition zone can be considered as the lifetime of the putative oxocarbenium intermediate. This time-gap (238 fs) is considerably longer than those of dynamically concerted reactions, such as simple Diels-Alder reactions that typically have a time-gap of less than 30 fs.[24c,33] This relatively long time gap is consistent with a loose S_N2 transition state structure with

weak C^1–O^{Nu} and C^1–O^{LG} bonding interactions. Nonetheless, because no local minimum was observed on the FES and the lifetime of oxocarbenium-like structures is much shorter than those in S_N1-type processes (*vide infra*), this reaction pathway should be considered as an "energetically concerted" [46c, 60] S_N2-type process and high levels of stereospecificity are therefore expected. The C^1–O^{Nu} and C^1–O^{LG} bond distances along the BOMD trajectories (Figure 2-10b) and geometries of representative snapshots (Figure 2-10d) also indicate a highly synchronous C^1–O^{LG} bond cleavage and C^1–O^{Nu} bond formation process.

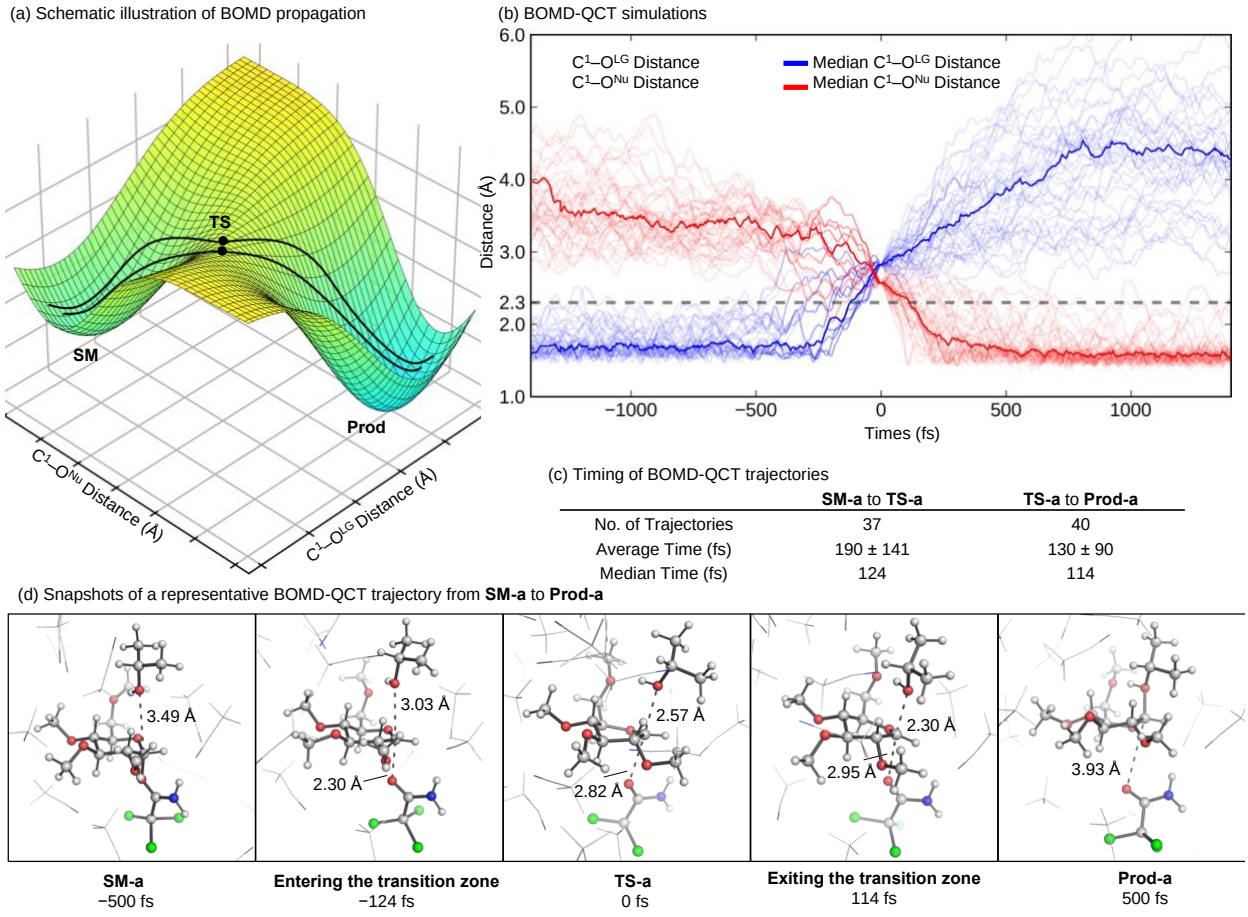

Figure 2-10 BOMD simulations of the glycosylation of 2-7 and i-PrOH in ACN.

Taken together, the metadynamics and BOMD simulations provide several criteria for distinguishing between S_N2- and S_N1-like mechanisms, including (1) shape of the FES, (2) synchronicity of transition state structures, in particular, the C^1–O^{Nu} and C^1–O^{LG} bond distances,

and (3) time-gap between leaving group dissociation and C^1–nucleophile bond formation (*i.e.* lifetime of the oxocarbenium intermediate). We surmise that the same computational procedures can be applied to study glycosylation reactions with other solvents, acceptors, and donors, and therefore they can provide a general understanding of how these individual factors affect the preference of S_N1 versus S_N2 mechanisms. In the following sections, we will provide support to this claim on the basis of metadynamics and BOMD simulations for reactions occurring in the presence of different alcohol acceptors and in different solvents.

2.3.3 Solvent Effects on the Glycosylation Mechanism

Solvent effects have been recognized as one of the most important factors on the mechanism and stereospecificity of glycosylation reactions.[14b,23,61] However, the understanding of solvent effects on glycosylation is still very limited and the selection of solvent is mostly based on trial-and-error. The complexity of solvent effects arises from multiple distinct types of interactions with solvent molecules, including long- and mid-range electrostatic interactions that stabilize charged species (e.g., oxocarbenium intermediates) in polar solvents, hydrogen bonding interactions with solvent molecules, and explicit solvent coordination (*e.g.* with nitrile solvents) to the anomeric carbon of the oxocarbenium cation.[62] In addition, the solvent can also affect the conformation of the oxocarbenium cation and the tightness of the ion pair intermediate.[14b,23]

It has been observed experimentally that the glycosylation of glucosyl donor **2-5** with *i*-PrOH in ACN favors the stereoinversion product (Table 2-1). This S_N2-type selectivity is consistent with the preference for the S_N2 pathway indicated by our AIMD simulations. On the other hand, the same reaction favors the stereoretentive α product in other solvents, such as DCM and MTBE, which supports an S_N1-type mechanism. To probe these solvent effects on the

mechanism of glycosylation, we performed AIMD simulations in explicit DCM and MTBE solvents. First, we modeled the stereoinversion pathways using metadynamics. The simulations were set up in a similar fashion as those carried out in ACN. In the initial geometry of the metadynamics simulations, the *i*-PrOH acceptor was placed at the opposite sides of the leaving group at a distance of 4 Å from the donor **2-7** The FES from the metadynamics simulations indicate an S_N1-type mechanism in both DCM and MTBE solvents (Figures 2-11a and 2-13a). In these reactions, an oxocarbenium intermediate and two stepwise transition states, one involving $C–O^{LG}$ dissociation and the other involving $C–O^{Nu}$ formation, are present in the minimum energy path (MEP).

The reaction in DCM initiates via a low-barrier transition state for the leaving group dissociation (**TS1-b**) with a $C^1–O^{LG}$ distance of 2.13 Å (Figure 2-11b). The relatively long $C^1–O^{Nu}$ distance (3.19 Å) is consistent with the S_N1 character of the leaving group dissociation TS. This transition state leads to oxocarbenium intermediate **Int-b**, which corresponds to a shallow local minimum on the FES. The subsequent $C^1–O^{Nu}$ bond formation occurs via **TS2-b**, which is 5.0 kcal/mol higher in energy than **Int-b**. The $C^1–O^{Nu}$ bond formation is exergonic and involves an early transition state with a relatively long $C^1–O^{Nu}$ distance (2.66 Å). The S_N1-character of the reaction is further corroborated by the Mulliken charges of the stationary points along the MEP. Both C^1 and the endocyclic oxygen (O^5) are more positively charged in **TS1-b**, **Int-1b**, and **TS2-b** than those in the starting material (**SM-b**) and the alkyloxonium product (**Prod-b**), indicating an oxocarbenium character in both transition states and the intermediate.

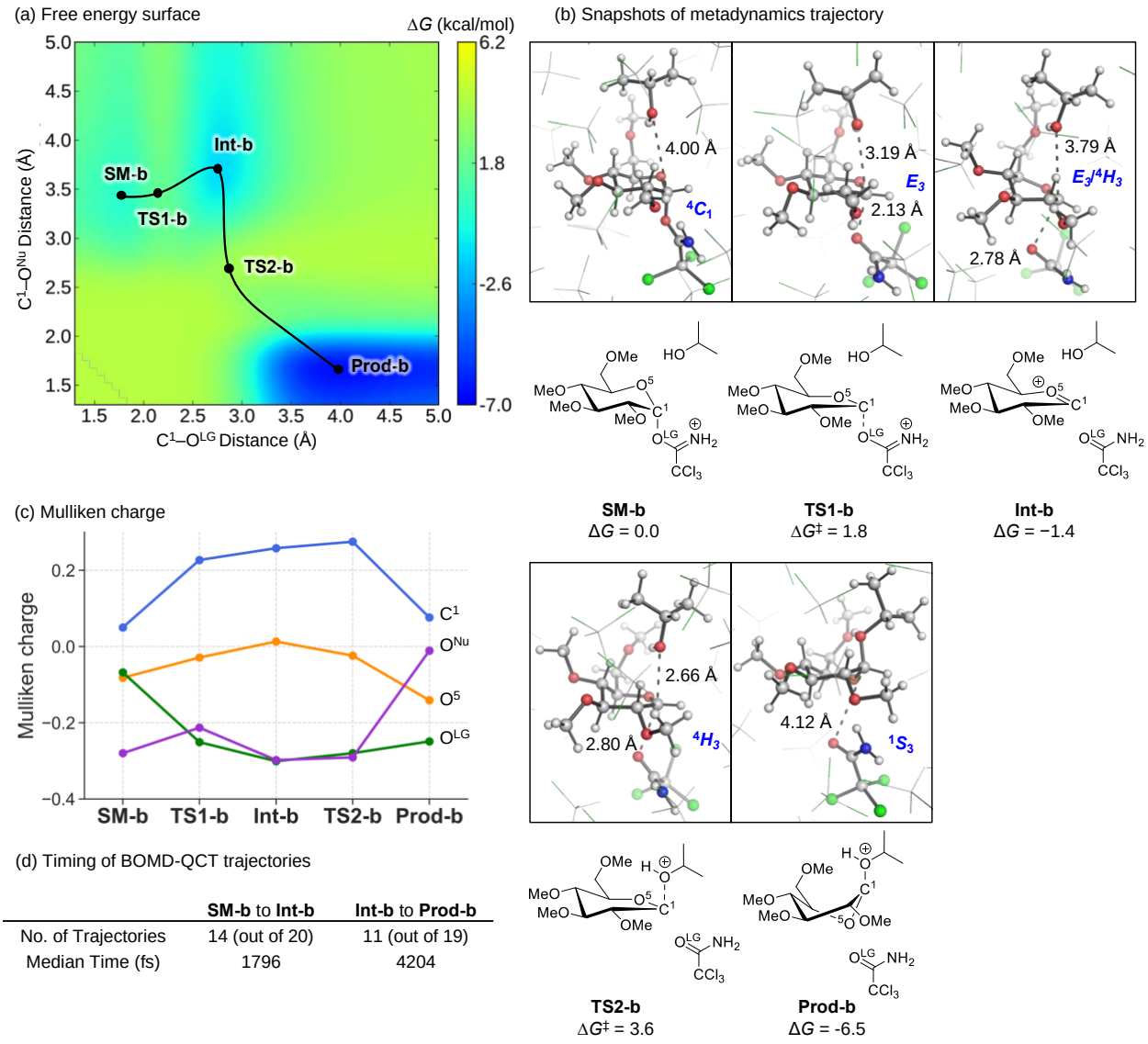

(d) Timing of BOMD-QCT trajectories

	SM-b to **Int-b**	**Int-b** to **Prod-b**
No. of Trajectories	14 (out of 20)	11 (out of 19)
Median Time (fs)	1796	4204

Figure 2-11 AIMD metadynamics simulations of the glycosylation of 2-7 and i-PrOH giving a stereoinversion product in DCM.

We then performed BOMD simulations starting from **Int-b** to evaluate the lifetime of the oxocarbenium intermediate in DCM. The BOMD calculations were initiated by sampling the geometry and velocity of intermediate structures and solvent with the C^1–O^{LG} and C^1–O^{Nu} distances constrained at 2.80 and 3.77 Å, respectively (Figure 2-12). These trajectories required a much longer time to convert the oxocarbenium intermediate to either the starting material or the alkyloxonium product. Out of the 20 "backward" trajectories that form the initial reactants, only

14 formed the C^1–O^{LG} bond within the 5 ps simulation; the other six remained at the oxocarbenium intermediate. Among the "forward" trajectories toward the alkyloxonium product, only 11 out of 19 formed the C^1–O^{Nu} bond within 5 ps. The time to traverse the "transition zone", calculated from the sum of the median time from C^1–O^{LG} bond cleavage to **Int-b** and the median time from **Int-b** to the C^1–O^{Nu} bond formation, is 6.0 ps.[63] This value, which can be considered an estimate of the lifetime of the oxocarbenium ion, is close to the experimentally determined value of 10^{-12} s (1 ps) for the glycosyl cation in aqueous solution.[64] The relatively long lifetime of the oxocarbenium compared to the lifetime of oxocarbenium-type structure in ACN (238 fs) further confirmed that the reaction in DCM occurs via an S_N1-type mechanism.

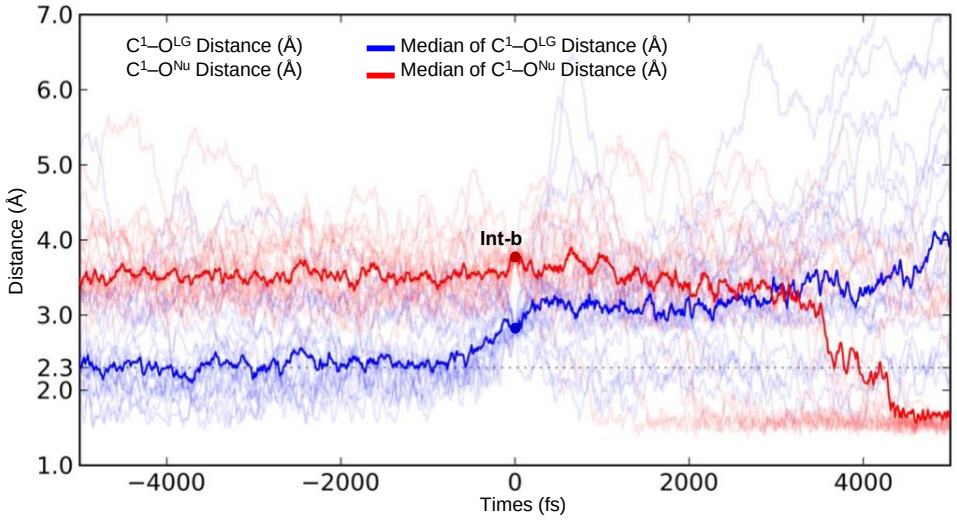

Figure 2-12 BOMD simulations of the glycosylation of 2-7 and i-PrOH in DCM solvent.

The FES of the stereoinversion pathway in MTBE also indicates a stepwise, S_N1-type mechanism (Figure 2-13a), but the free energy landscape is substantially different from that in DCM. Similar to the reaction in DCM, the C^1–O^{LG} dissociation requires a low barrier from the activated donor **2-7**. The dissociation transition state (**TS1-c**) also has a long C^1–O^{Nu} bond distance (3.70 Å) that is consistent with an S_N1-character. In MTBE, the oxocarbenium ion (**Int-c**) is

significantly more stable than the starting material (ΔG = −6.7 kcal/mol with respect to **SM-c**). The subsequent nucleophilic attack transition state (**TS2-c**) requires a high barrier of 16.8 kcal/mol with respect to **Int-c**. This is much less favorable than the C^1–O^{Nu} bond formation in DCM ($\Delta G^{\ddagger}$ = 5.0 kcal/mol with respect to **Int-b**). The high barrier of **TS2-c** suggests that the C^1–O^{Nu} bond formation most likely occurs via other mechanisms, such as the stereoretention pathway to form the α-product (*vide infra*) and an alternative stereoinversion pathway where the trichloroacetamide leaving group escapes from the solvent cage before the nucleophilic attack of the acceptor occurs.

The metadynamics and BOMD simulations discussed above reveal distinct mechanistic scenarios for the three different solvents. Whereas the glycosylation in ACN occurs via an S_N2-type mechanism, the reactions in DCM and MTBE favor the S_N1-type mechanism. Besides, the oxocarbenium intermediate is more stable in MTBE (*i.e.* the reaction is more S_N1-like in MTBE than in DCM). To provide a quantitative measure of the solvent effects, we calculated the solvent/solute interaction energies ($\Delta E_{\text{sol-interaction}}$) for the S_N2-type transition states and oxocarbenium ion intermediates in ACN and MTBE (Figure 2-13d).47 In order to compare solvent stabilization effects on structures in different regions of the FES, we calculated $\Delta E_{\text{sol-interaction}}$ for structures with the same C^1–O^{LG} and C^1–O^{Nu} distances in explicit ACN and MTBE. Specifically, two sets of $d(C^1–O^{LG})$ and $d(C^1–O^{Nu})$ were analyzed, including structures with $d(C^1–O^{LG})$ = 2.84 Å and $d(C^1–O^{Nu})$ = 2.56 Å to mimic the S_N2-type transition state structure (i.e. **TS1-a**) and structures with $d(C^1–O^{LG})$ = 3.74 Å and $d(C^1–O^{Nu})$ = 3.68 Å to mimic the oxocarbenium ion intermediate (i.e. **Int-c**). The computed $\Delta E_{\text{sol-interaction}}$ values indicate that the stabilization by ACN is comparable in the S_N2-TS and oxocarbenium regions of the FES (c.a. 73-77 kcal/mol). On the other hand, the MTBE solvent has greater stabilizing interaction with the oxocarbenium ion intermediate ($\Delta E_{\text{sol-interaction}}$ = −70.9 kcal/mol) than that with the S_N2 transition state ($\Delta E_{\text{sol-interaction}}$

= −53.5 kcal/mol). These results suggest that the different mechanisms of glycosylation in ACN and MTBE are due to the different solvent/solute interactions with the S_N2 transition state.

On the FES of MTBE, the region corresponding to the S_N2 TS is much higher in energy (ΔG = 11.4 kcal/mol) than **Int-c** (ΔG = −6.7 kcal/mol), owing to the ineffectiveness of the MTBE solvent in stabilizing the S_N2 transition state.

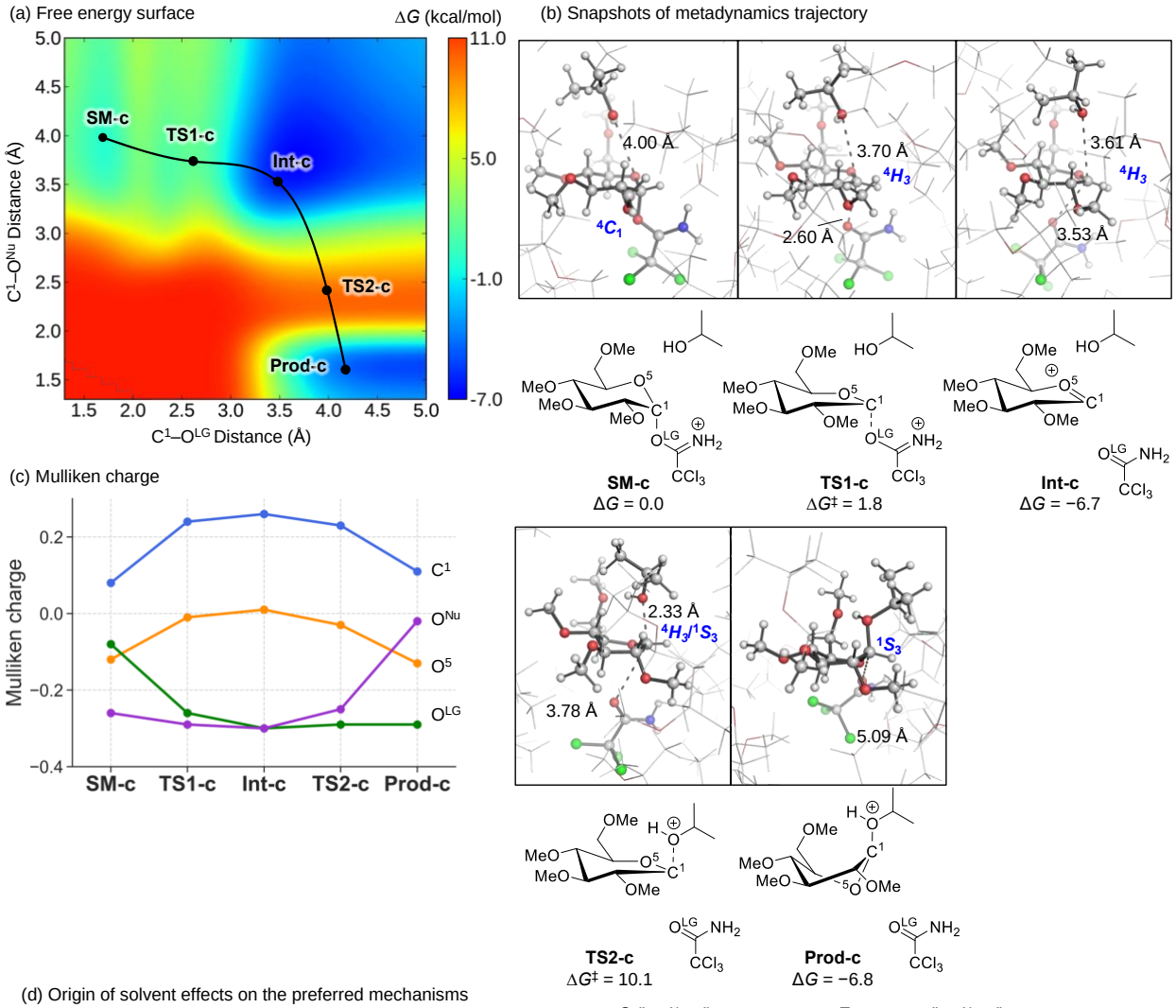

(d) Origin of solvent effects on the preferred mechanisms

Region on FES	$d(C^1–O^{LG})$ (Å)	$d(C^1–O^{Nu})$ (Å)	ΔG (kcal/mol)		$\Delta E_{sol\text{-}interaction}$ (kcal/mol)	
			ACN	MTBE	ACN	MTBE
S_N2 TS	2.84	2.56	5.3	11.4	−73.2	−53.5
Oxocarbenium	3.74	3.68	7.5	−6.7	−77.0	−70.9

Figure 2-13 AIMD metadynamics simulations of the stereoinversion pathway in the glycosylation of 2-7 and *i*-PrOH in explicit MTBE.

The different solvent/solute interaction is likely to originate from solvent steric effects. Because the positive charge of the S_N2-type transition state is mainly located on the anomeric carbon and the endocyclic oxygen (Figure 2-14), the sterically encumbered MTBE solvent molecules cannot effectively stabilize the positive charge in the S_N2 transition state due to repulsions with both the leaving group and the alcohol acceptor. On the other hand, ACN is a

privileged polar solvent for stabilizing the positive charge in the S_N2 transition state. Because the negatively charged "tip" of ACN molecules is small, the solvent molecules can approach the anomeric carbon and stabilize the partial positive charge.

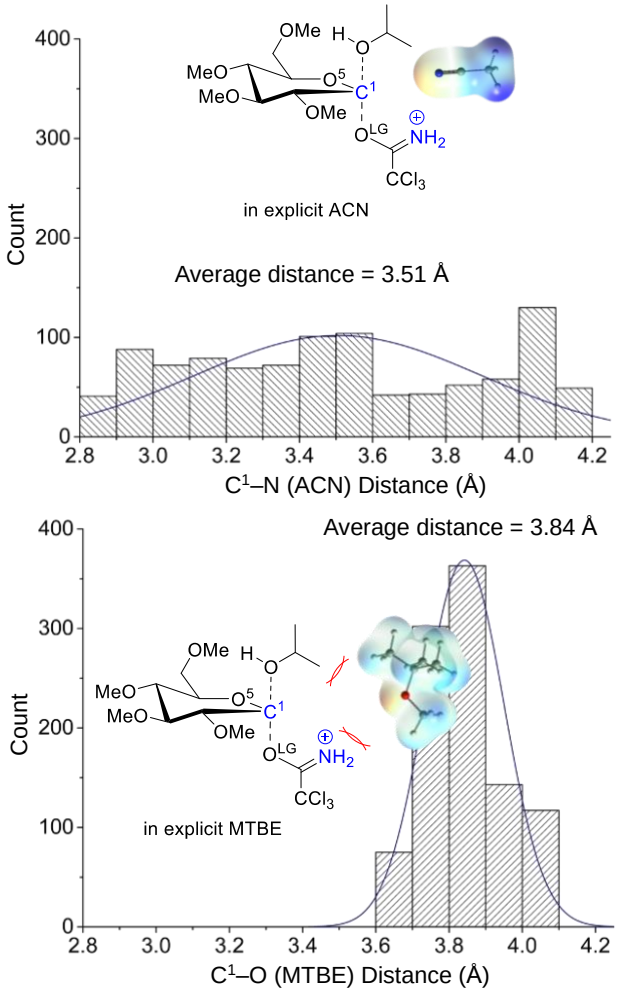

Figure 2-14 Solvent/solute interaction energy calculations.

Next, we performed metadynamics simulations on the stereoretention pathway in explicit MTBE (Figure 2-15). These calculations were initiated by placing the *i*-PrOH acceptor 4 Å away from **2-7** but on the same side as the leaving group. The FES indicates a stepwise S_N1 mechanism, where the leaving group dissociation (**TS1-d**) occurs in a similar fashion to the stereoinversion pathway and leads to a stable oxocarbenium ion ($\Delta G = -8.7$ kcal/mol with respect to the activated

donor complex, **SM-d**). The C^1–O^{Nu} bond formation occurs via transition state **TS2-d,** which requires a barrier of 9.2 kcal/mol with respect to **Int-d**. This barrier is 7.6 kcal/mol lower than the C^1–O^{Nu} bond formation TS (**TS2-c**) where the leaving group and the *i*-PrOH acceptor are on opposite sides of the pyranose ring. Here, **TS2-d** is stabilized by hydrogen-bonding interaction between the carbonyl oxygen of the amide leaving group and the *i*-PrOH. A similar leaving group-assisted frontside nucleophilic substitution mechanism has been previously proposed in enzymatic systems and solvolysis reactions.[65] Solvent/solute interaction energies ($\Delta E_{\text{sol-interaction}}$) were calculated to investigate solvent effects in this stereoretention pathway in explicit MTBE (Figure 2-13d).[66] Due to similar solvent steric effects, MTBE stabilizes the oxocarbenium intermediate much more effectively than the sterically encumbered "front-side" S_N2-transition state like structure. The solvent/solute interaction with the oxocarbenium intermediate in the stereoretention pathway is slightly weaker than that in the stereoinversion pathway ($\Delta E_{\text{sol-interaction}}$ = −67.4 and −70.9 kcal/mol respectively), indicating the greater stability of the oxocarbenium intermediate in the stereoretention pathway (**Int-d**) compared to **Int-c** in the stereoinversion pathway is due to the hydrogen bond between the amide leaving group and the *i*-PrOH, rather than solvent effects.

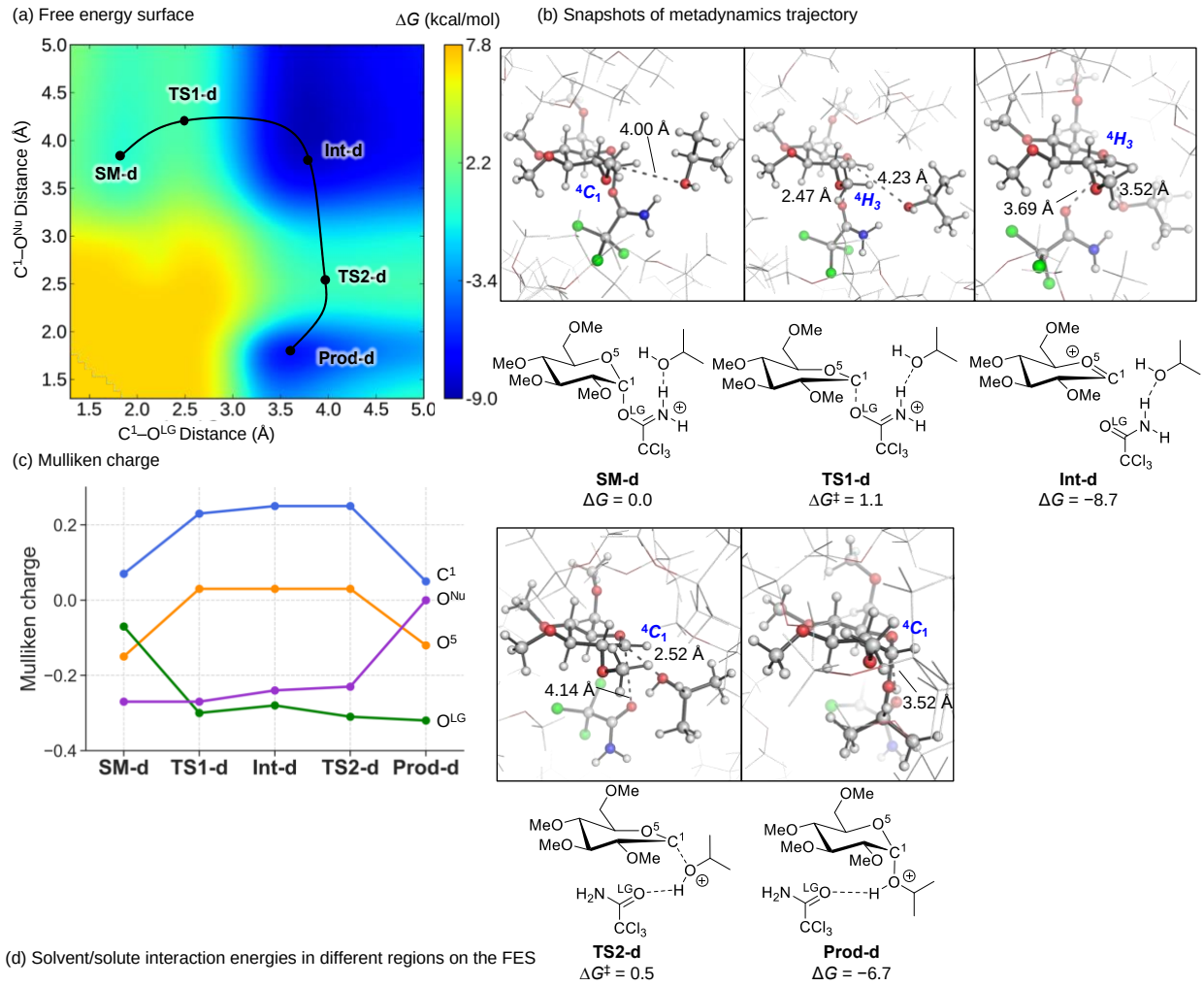

(d) Solvent/solute interaction energies in different regions on the FES

Region on FES	$d(C^1–O^{LG})$ (Å)	$d(C^1–O^{Nu})$ (Å)	ΔG (kcal/mol)	$\Delta E_{sol\text{-}interaction}$ (kcal/mol)
S_N2 TS	2.84	2.56	6.6	−49.9
Oxocarbenium	3.74	3.68	−8.0	−67.4

Figure 2-15 AIMD metadynamics simulations of the stereoretention pathway in the glycosylation of 2-7 and i-PrOH in explicit MTBE.

Next, we performed BOMD simulations starting from **Int-d** in MTBE (Figure 2-16). More than 50% of these trajectories were still trapped in the oxocarbenium intermediate after 5 ps simulations. These results suggest that the lifetime of the oxocarbenium intermediate is much longer in MTBE solvent than in ACN and DCM.[67]

(a) BOMD-QCT simulations initiate from **Int-d**

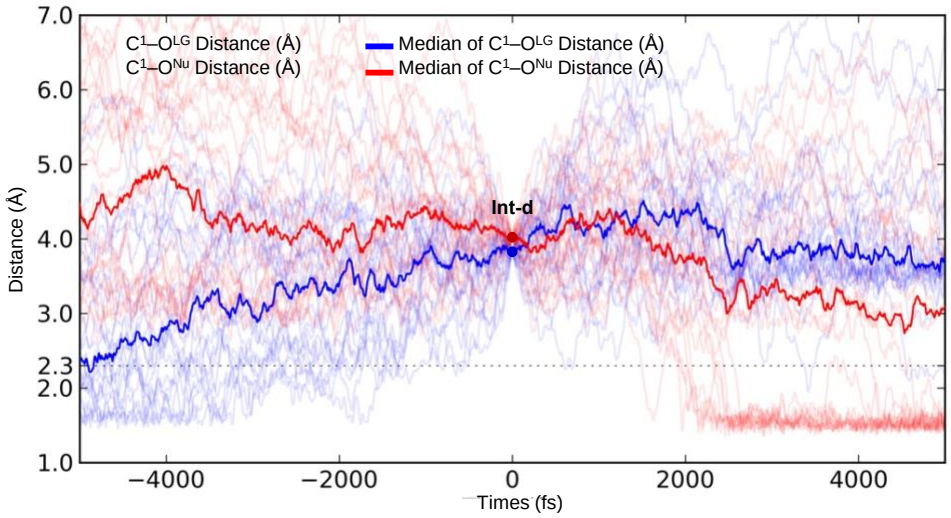

(b) Timing for BOMD-QCT simulations

	Trajs to **SM-d**	Trajs to **Prod-d**
No. of Trajs	13 (out of 26)	11 (out of 24)
Median Time	> 5ps	> 5ps

Figure 2-16 BOMD simulations of the glycosylation of 2-7 and i-PrOH in explicit MTBE solvent.

2.3.4 Steric Effects of Acceptor on the Mechanisms and Time-gap between Bond Cleavage and Bond Formation

Identity of the acceptor also plays important roles on the mechanisms and stereochemical outcomes of glycosylation. In comparison to the well-documented electronic effects,[68] the steric effects of acceptor on the glycosylation mechanism are less well understood. We surmised that even subtle changes in the acceptor steric properties may affect the shape of the FES and the lifetime of the oxocarbenium intermediate, and thus shift the mechanism within the S_N1/S_N2 continuum. As we showed that the sterically less hindered ACN solvent promotes the S_N2-like mechanism in the reaction of **2-7** with *i*-PrOH, it is also interesting to consider whether the reaction is also sensitive to the steric properties of the acceptor. Using the same computational approach described above, we performed metadynamics and BOMD simulations on the backside attack

pathways in reactions of the glucosyl donor **2-7** with *t*-BuOH and EtOH in ACN (Figure 2-17). Similar to the reaction with *i*-PrOH (Figure 2-5), the metadynamics simulations point to an S_N2-like mechanisms for the backside attack with *t*-BuOH and EtOH, as the putative oxocarbenium intermediate is not a local minimum on these FESs. Although the S_N2 transition state with EtOH (**TS1-e**) is earlier than **TS1-a** (with *i*-PrOH) and has a shorter C^1–O^{LG} distance and a longer C^1–O^{Nu} distance, the activation free energy for EtOH is comparable to that for *i*-PrOH. The BOMD simulations revealed similar time-gaps between C^1–O^{LG} cleavage and C^1–O^{Nu} formation with these two acceptors. We conclude that the reactions with both EtOH and *i*-PrOH show a preference for the concerted S_N2 reaction path and high stereospecificities are therefore anticipated. On the other hand, the S_N2 reaction path with *t*-BuOH as acceptor has a higher activation energy barrier (10.1 kcal/mol). In addition, the transition state region on the FES is much flatter (Figure 2-17d). The "caldera"[69] on the FES suggests longer times for the trajectories to traverse the transition state region (*i.e.* a longer time between C^1–O^{LG} cleavage and C^1–O^{Nu} formation). BOMD simulations indicate that a much longer time (1064 fs) is required to traverse the transition zone when *t*-BuOH is used as an acceptor. The computed solvent/solute interaction energies ($\Delta E_{\text{sol-interaction}}$) for the S_N2 transition states with the three acceptors suggest that the higher-energy and flatter TS region is caused by a reduced solvent stabilization of the S_N2 transition state with the sterically encumbered *t*-BuOH acceptor ($\Delta E_{\text{sol-interaction}}$ = −73.8, −73.2, and −57.4 kcal/mol for the S_N2 TSs with EtOH, *i*-PrOH, and *t*-BuOH, respectively). The higher free energy barrier required to access the backside S_N2 TS and the longer time-gap between C^1–O^{LG} cleavage and C^1–O^{Nu} formation suggest that the stereoselectivity of the reaction can decrease, because the competing S_N1-type pathways become kinetically more favorable. Although no experimental data is available concerning the stereoselectivity of the reactions with EtOH and *t*-BuOH in ACN, our results concerning the

acceptor steric effects are consistent with what has been observed in the glycosylation of **2-5** in DCM, in which higher ratios of stereoinversion products are obtained with more hindered alcohol acceptors (entries 2−5, Table 1).

(a) Reaction scheme

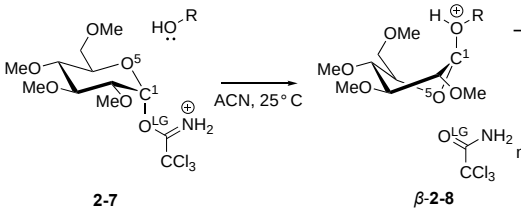

2-7 **β-2-8**

(b) Summary of metadynamics and BOMD-QCT simulations

Acceptor	EtOH	*i*-PrOH	*t*-BuOH
$\Delta G^{\ddagger}$ (kcal/mol)	6.3 (**TS1-e**)	5.3 (**TS1-a**)	10.1 (**TS1-f**)
$d(C^1–O^{LG})$ (Å)	2.43	2.83	2.69
$d(C^1–O^{Nu})$ (Å)	2.69	2.56	2.43
median time to traverse the transition zone (fs)	255	238	1064
$\Delta E_{sol\text{-}interaction}$ (kcal/mol)	−73.8	−73.2	−57.4

(c) Metadynamics simulations (left) and BOMD-QCT simulations (right) using EtOH as acceptor

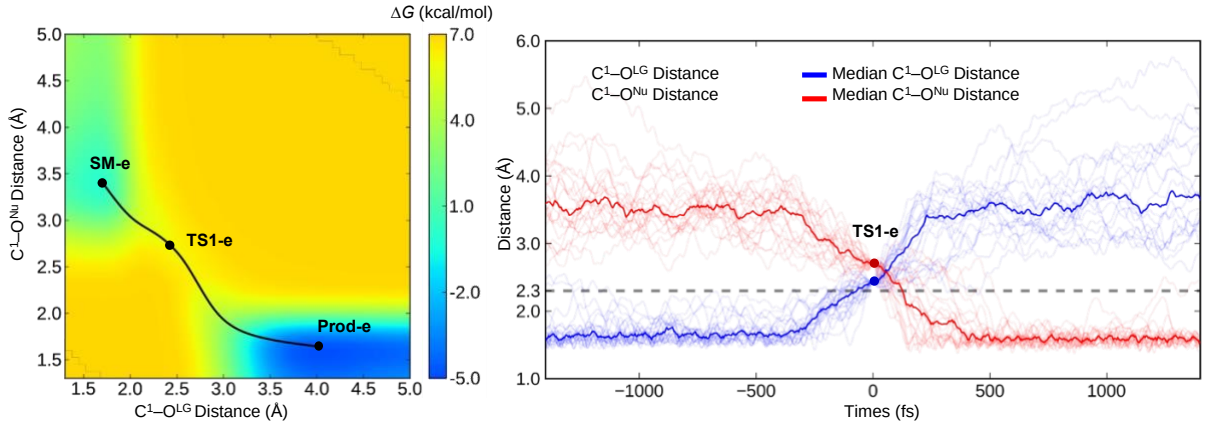

(d) Metadynamics simulations (left) and BOMD-QCT simulations (right) using *t*-BuOH as acceptor

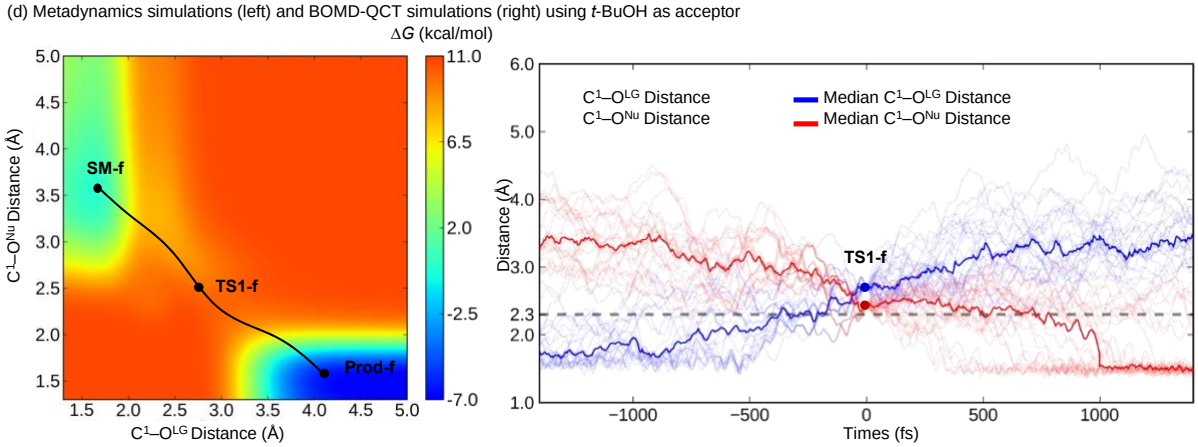

Figure 2-17 Acceptor effects on glycosylation reactions of 2-7 with *t*-BuOH, *i*-PrOH, and EtOH as acceptors in ACN solution.

2.3.5 Metrics for Describing the S_N1/S_N2 Mechanistic Continuum

The simulations discussed above provide a considerable amount of information concerning the real-time mechanisms of glycosylation reactions in different solvents. To establish a standard approach for describing the glycosylation mechanisms in the S_N1/S_N2 continuum, we propose three metrics that are relatively straightforward to obtain from the simulations described in this work. First, the number of transition states (*i.e.* saddle points) on the minimum (free) energy path (MEP) provides a direct measure for distinguishing energetically concerted and stepwise mechanisms.[46c] Second, the synchronicity of the transition state structure, which can be identified with the difference between the lengths of the forming and cleaving bonds in the transition state, provides geometry-based distinction between S_N1- and S_N2-like transition states. Finally, the time required to cross the transition zone, which can be calculated from the median time-gap between leaving group dissociation and acceptor association in BOMD simulations, describes the lifetime of the putative oxocarbenium intermediate. These three metrics for the different glycosylation reactions investigated in this study are summarized in Table 2-2. For stepwise reactions involving an oxocarbenium intermediate on the MEP (*e.g.* entries 4 and 5 in Table 2-2), an additional metrics, the C^1–O^{LG} distance in the oxocarbenium, may be used to distinguish between S_Ni- (contact ion pair) and S_N1-(solvent-separated ion pair) like mechanisms. These descriptors provide a complementary and consistent description of competing glycosylation mechanisms.

Table 2-2 Indicators of glycosylation mechanisms from metadynamics and AIMD simulations of backside attack pathways.

Entry	Solvent	Acceptor	Number of TSs on MEP	Synchronicity of TS Structure (Bond Distances in Å)	Time to Traverse Transition Zone (ps)[a]	Glycosylation Mechanism
1	ACN	EtOH	1	**TS1-e** *(synchronous)* 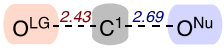	0.24	S_N2
2	ACN	*i*-PrOH	1	**TS1-a** *(synchronous)* 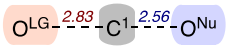	0.26	S_N2
3	ACN	*t*-BuOH	1	**TS1-f** *(synchronous)* 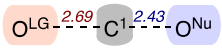	1.1	S_N2-like
4	DCM	*i*-PrOH	2	**TS1-b** *(asynchronous)* 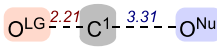 **TS2-b** *(synchronous)* 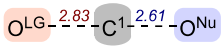	6.0	S_Ni/S_N1 [b]
5	MTBE	*i*-PrOH	2	**TS1-c** *(asynchronous)* 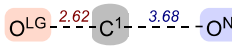 **TS2-c** *(asynchronous)* 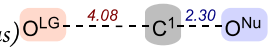	> 10	S_N1 [b]

[a] Median time-gap between C^1–O^{LG} dissociation and C^1–O^{Nu} bond formation. For S_N1-type mechanisms, this time-gap can be considered as the lifetime of the oxocarbenium intermediate. [b] The C^1–O^{LG} distances in the oxocarbenium intermediate (2.80 and 3.74 Å for entries 4 and 5, respectively) are used to distinguish between S_Ni- and S_N1-like mechanisms.

2.4 Conclusion

We used AIMD simulations, including free-energy metadynamics and BOMD calculations, to study the effects of acceptor and solvent on the mechanism of glycosylation reactions. All simulations were carried out with explicit solvent. We considered the reactions of an activated glucosyl α-trichloroacetimidate donor (**2-7**) with three acceptors (EtOH, *i*-PrOH, and *t*-BuOH) in three solvents (ACN, DCM, and MTBE). Consistent with experimental stereospecificity data, we found that the reaction of **2-7** with *i*-PrOH in ACN occurs via a concerted S_N2 mechanism without an oxocarbenium-type intermediate in the minimum energy path. The

relatively large gap between the times of the dissociation of the leaving group and of the formation of a C–O bond with the acceptor (238 fs) is consistent with a loose transition state structure characterized by weak bonding interactions. This reaction can therefore be considered as an "energetically concerted" S_N2-type process with expected high levels of stereospecificity. The analogous reactions carried out in DCM and MTBE exhibit a more marked S_N1 character with the formation of an oxocarbenium intermediate, which is considerably more stable in MTBE than in DCM. The tendency of MTBE to disfavor the S_N2 mechanism can be explained by its inability to stabilize the positive charge in the S_N2 transition state, due to solvent steric effects. We also examined the dependence of the reaction mechanism on the nature of the acceptor. The sterically hindered *t*-BuOH acceptor not only increases the free energy barrier of the S_N2 pathway but it also makes the transition state region flatter. This "caldera"-type free energy surface leads to longer times to traverse the transition zone in the "dynamically stepwise" trajectories.

Based on the metadynamics and BOMD simulation results, we identified three metrics to quantitatively describe the nature of the glycosylation mechanism within the S_N1/S_N2 continuum for a given reaction: 1) the number of transition states in the MEP; 2) the synchronicity of the transition state geometry (*i.e.* the difference between the forming and cleaving bond distances); 3) the time-gap between the leaving group dissociation and the acceptor association (*i.e.* the lifetime of the putative oxocarbenium intermediate). These metrics can be obtained for wide varieties of glycosylation conditions using the computational approaches described in this work and can be used to study the effects of different factors on the mechanism of glycosylation reactions in solution.

3.0 Origins of Catalyst-controlled Selectivity in the Ag-catalyzed Regiodivergent C−H Amination

3.1 Introduction

C–H bond amination via nitrene transfer enables efficient construction of new C–N bonds from C–H bonds. It is of great interest due to the prevalence of amines in pharmaceuticals, agrochemicals, and bioactive natural products. Many different transition metal catalysts including first- (Co, Fe, Mn, and Cu), second- (Ru, Rh, Pd, and Ag), and third-row transition metals (Ir, Au) are capable of promoting C–H bond amination (Figure 3-1).[5,70]

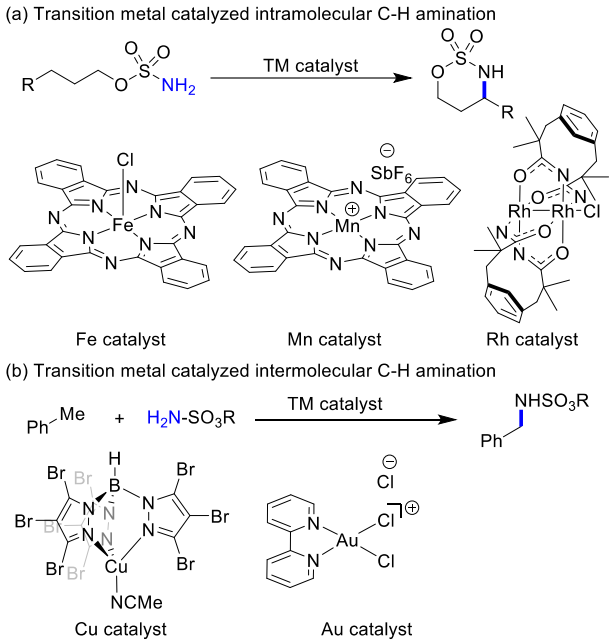

Figure 3-1 Selected examples for transition metal catalyzed intra- and intermolecular C–H amination.

There are numerous computational studies on the mechanisms of transition metal catalyzed C–H amination reactions (Figure 3-2). Computational studies revealed two-state or multi-state reactivity in which spin crossover might be involved in the reaction process.[71] Moreover, depending on the existing of the discrete radical intermediates, the reaction can proceed through concerted (in the absence of radical intermediate) or stepwise mechanism (in the presence of short lifetime radical intermediate for first type of stepwise mechanism or with a long-lived radical intermediate for the second type of stepwise mechanism). The concertedness (i.e. concerted or

stepwise mechanism) of C–H cleavage and nitrene insertion events is heavily dependent on the choice of metal catalyst, electronic structure of the metal complex, and the nitrene precursors, etc.[72] Some closed-shell singlet transition metal (e.g. Cu, Rh dimer,[73] and Ru[74]) nitrene complexes were reported to undergo concerted C−H insertion transition state (TS). Several open-shell (doublet, triplet, etc.) transition metal complexes (Cu,[75] Co,[76] Rh dimer, Fe,[77] or Ru_2[78]) were shown to favor stepwise mechanisms, where a radical intermediate is generated from H atom transfer transition state. There are also studies suggesting both concerted and stepwise mechanisms can be involved at the same time. Computational and experimental mechanistic study on a copper-catalyzed benzylic amination by Barman et al.[79] suggests that, in the rate-limiting step, the triplet pathway dominates with a minor singlet pathway. The triplet pathway proceeds via a stepwise pathway whereas the singlet pathway proceeds via a concerted pathway.

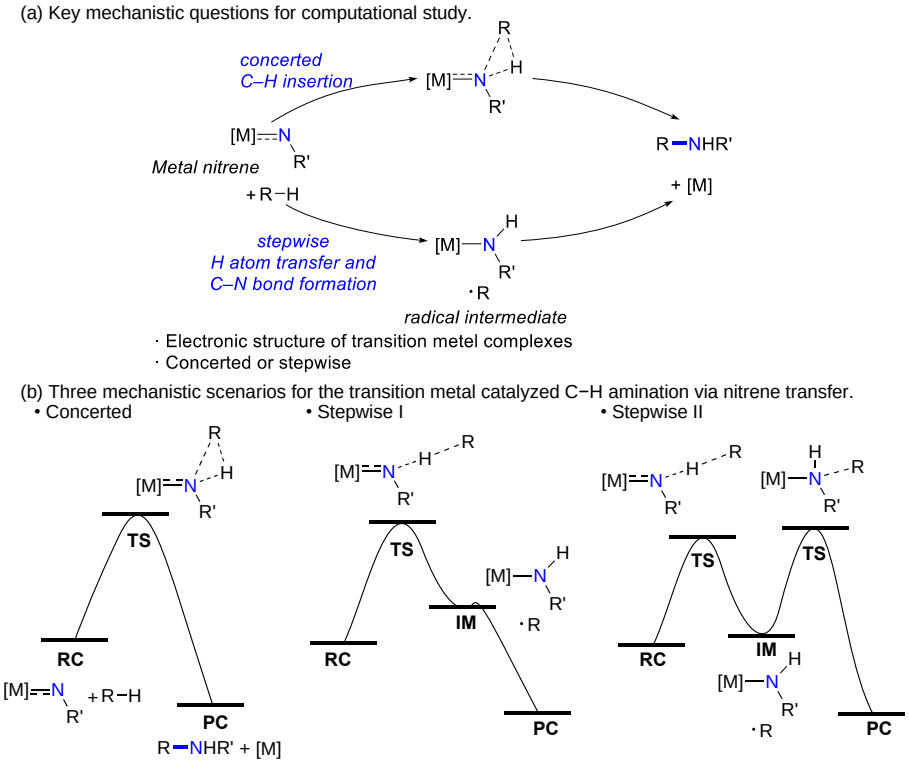

Figure 3-2 Computational study on the mechanisms of transition metal catalyzed C–H amination reactions.

In addition to the complicated nature of the reaction mechanism, understanding how the selectivity is controlled and can be predicted is one of the key challenges in developing selective C–H functionalization. Predictive model [80] is a powerful tool to establish a mathematical relationship to predict reaction outcome (regioselectivities, yield, and rates, etc.) based on readily determined variables (molecular properties and reaction conditions, etc.). [81] Previous computational predictive models developed by Houk[82] demonstrated activation energies of C–H oxidations correlate with BDEs of the reacting C–H bonds. On the other hand, studies by White[83] have elucidated the strong substrate electronic bias on the Fe-catalyzed C–H oxidation and Mn-catalyzed C–H aminations. However, effective predictive model for catalyst-controlled selectivity that enhances or overturns the substrate's inherent selectivity preference is rare.

In this context, the development of Ag-catalyzed nitrene transfer (NT) (Figure 3-3) has attracted recent attention. The diversity of ligands able to support Ag catalysts results in a broad range of steric and electronic environments around the reactive center, offering unique opportunities to achieve catalyst-controlled regio- and enantioselectivities.

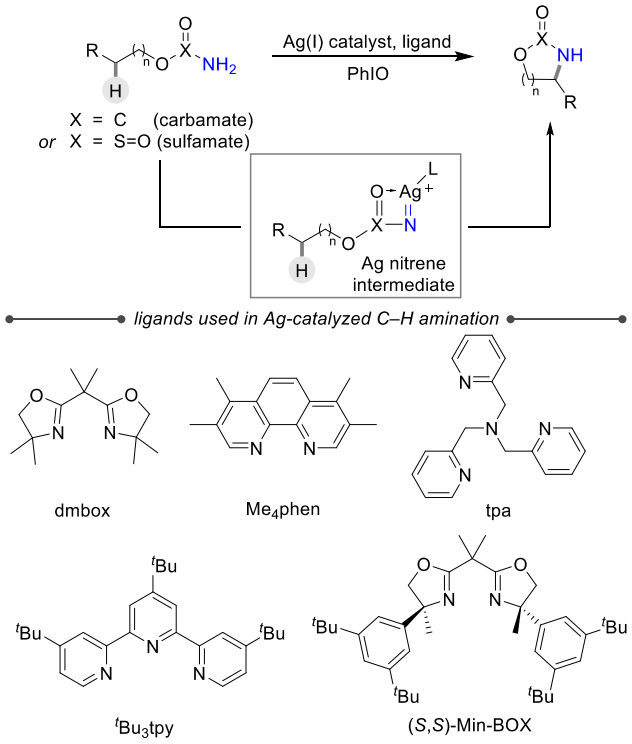

Figure 3-3 Ag-catalyzed C–H amination via nitrene transfer (NT)

Schomaker et al. have demonstrated that the expected regioselectivity of Ag-catalyzed C–H amination can be modulated, and sometimes completely reversed, by the electronic and steric properties of the substrate, as well as the identity of the ancillary ligands on the metal (Figure 3-4).[6] In addition, reactions applying precursors with different nitrogen protecting groups (e.g. carbamate and sulfamate) may yield complete reversal in regioselectivities. These reactions provide access to both 1,2- and 1,3-difunctionalized amine products after removal of the *N*-protecting group.

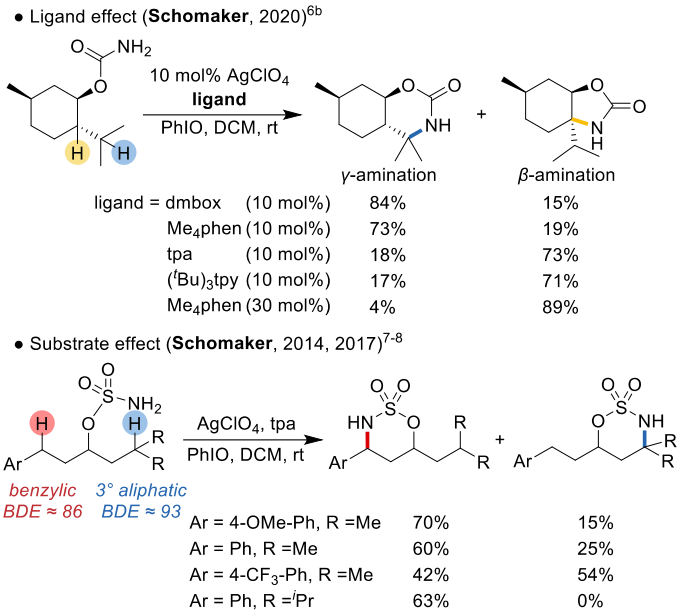

Figure 3-4 Tunable regioselectivities in the Ag-catalyzed C–H amination. BDEs are in kcal/mol.

Despite these interesting observations, the origin of the catalyst and substrate effects on regioselectivity is still not well-understood. Previous computational study by Berry and Schomaker[84] on the intermolecular C–H amination reaction (Figure 3-5) suggested a stepwise triplet pathway is more favorable than the concerted singlet pathway based on DFT calculations. However, this conclusion may be affected by the choice of DFT methods and the experimental systems (In this study, I focused on intramolecular C–H amination) used in the calculations.

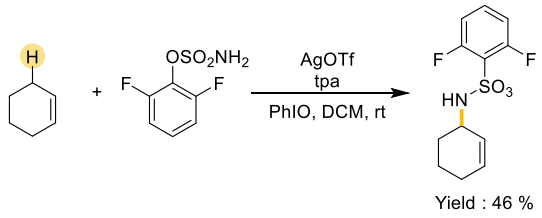

Figure 3-5 Previous computational study on an intermolecular C–H amination reaction.

Considering the drastic differences between these systems and questions to be studied, I studied the reaction mechanism using high level computational methods and evaluated different factors that might affect the regioselectivities. The regioselectivity appears to be controlled by the

combination of several factors, including bond dissociation enthalpy (BDE), electronic properties and the steric environment of the C–H bonds, tether length, the ancillary ligands on the Ag, and the identity of the precursors.[6b,7-9,85] We surmised that a holistic understanding of the interplay of these different factors would offer practical guidance to broaden the scope of the regioselective amination, develop Ag catalysts to effectively distinguish between C–H bonds with similar BDEs and steric environments, and override inherent substrate preference to favor less reactive sites. Herein, we report a computational study to understand the reaction mechanism of the Ag-catalyzed amination and gain insights into the origin of reactivity and regioselectivity. We analyze why different catalyst systems favor different types of C–H bonds through the lens of their differing sensitivities to BDEs, tether length, electronic effects, and ligand–substrate steric repulsions (Figure 3-6). We establish an approach to rationally select the most effective Ag catalyst and precursor group for a desired regioselective amination, based on the intrinsic electronic and steric properties of the C–H bonds. Experimental studies were performed to validate the computationally-predicted regioselectivity trends in different catalyst systems. This mechanistically-guided approach was applied to achieve catalyst-controlled regiodivergent amination of alkyl C–H bonds that display similar steric and electronic environments.

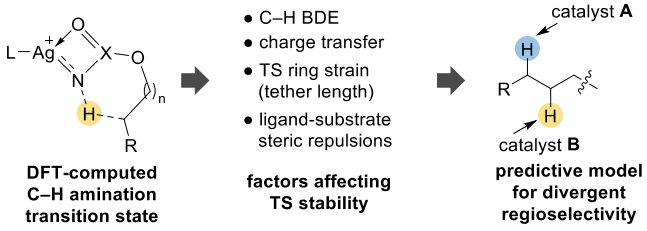

Figure 3-6 Mechanistically driven approach for regioselectivity prediction.

3.2 Computational Methods

3.2.1 DFT Calculations

DFT calculations, including geometry optimization and single-point energy calculations, were performed with the Gaussian 16 software package.[32] Geometries were optimized in the gas phase using the ωB97X-D[86] functional and a mixed basis set of def2-TZVPP for Ag and def2-SVP for other atoms. Single-point energies were calculated using ωB97X-D and the def2-TZVPP basis set for all atoms in dichloromethane (DCM) using the SMD solvation model.[21b] Conformers of each ground state and transition state structure were studied by manual conformational search and automated conformational sampling using CREST[35] and GFN2-xTB.[36] Low-energy conformers from the CREST/xTB conformational sampling were then re-optimized using DFT at the aforementioned level of theory. The reported Gibbs free energies and enthalpies in solution include thermal corrections computed at 298 K at the standard concentration (1 mol/L) using GoodVibes.[33] The 3D images of optimized structures were prepared using CYLView.[34] Bond dissociation enthalpy (BDE) and transition state ring strain energy (ΔH_s) were also calculated at the ωB97X-D/def2-TZVPP, SMD(DCM)//ωB97X-D/def2-SVP–def2-TZVPP(Ag) level of theory.

3.2.2 PNO-LCCSD(T)-F12

The explicitly correlated local coupled cluster with pair natural orbitals, PNO-LCCSD(T)-F12, [87] is a reasonable reliable method for energetics of systems with weak to moderate multireference character. Recent benchmark studies showed PNO-LCCSD(T)-F12 provides good

agreement with the canonical CCSD(T) results for open-shell transition metal systems,[88] and thus can be used as references to benchmark DFT methods.

PNO-LCCSD(T)-F12 benchmark calculations were performed using Molpro 2020.2.[89] The open-shell PNO-RCCSD(T)-F12[90] method was used for triplet complexes. In the local coupled-cluster theory calculations, the ECP28MDF effective core potential and the AWCVTZ basis set were used for Ag, aug-cc-pV(T+d)Z was used for S, VDZ was used for H, and VDZ-F12 was used for other atoms. The aug-cc-pVTZ-PP/JKFIT (Ag), AVTZ+/JKFIT (S), VTZ/JKFIT (H), and AVTZ/JKFIT (other atoms) fitting auxiliary basis sets were used to compute the Fock matrix and as the RI basis set. For the density fitting of all other two-electron integrals, the aug-cc-pVTZ-PP/MP2FIT (Ag), aug-cc-pVTZ/MP2FIT (S), VDZ/MP2FIT (H), and AVDZ/MP2FIT (other atoms) basis sets were used. These basis sets are similar to those used by Werner et al. in recent computational studies.[90-91] T1/D1 diagnostic values were calculated for all structures in the PNO-LCCSD(T)-F12 benchmark study and compared with the criteria recommended by Wilson et al. for 4d transition metals (T1 < 0.045 and D1 < 0.12).[92] The computed T1 values were all smaller than 0.045 and the D1 values were in the range of 0.10−0.20, suggesting small or moderate multireference character.

3.2.3 CASPT2

Complete active-space second-order perturbation theory (CASPT2) is one of the most commonly used multireference methods to calculate electronic structure of large transition metal complexes[93] when multiconfigurational character might be involved and has been applied to spin state energy calculations. It overcomes the inherent limitation of single determinant theory, such as KS DFT, etc.

CASPT2(10,10) benchmark calculations were performed using OpenMolcas[94] using the ANO-RCC-VTZP basis set. An active space of 10 electrons in 10 orbitals (10,10) was selected to include one N 2s, three N 2p orbitals, the Ag d_{z2} orbital, and extra d shell orbitals. All PNO-LCCSD(T)-F12 and CASPT2 calculations were performed in the gas phase using the DFT-optimized geometries.

3.3 Results and Discussion

3.3.1 Reaction Mechanisms of the Ag-catalyzed C–H Amination via Nitrene Transfer

The proposed mechanism (Figure 3-7) of the Ag-catalyzed C–H amination involves formation of Ag nitrene species **B** from Ag(I) pre-catalyst **A** and an iminoiodinane formed by the condensation of the carbamate or sulfamate substrate with PhIO. The subsequent C–H insertion with the Ag nitrene may involve two possible mechanisms: (a) an H-atom transfer to the Ag nitrene to form an alkyl radical intermediate **C**, followed by radical recombination to form the C–N bond in the final product **D**; and (b) a concerted C–H insertion process where the alkyl radical is not involved.[6,70,95] Experimental mechanistic studies, including radical clock and stereospecificity experiments, appear to support a concerted mechanism without long-lived radical intermediates in both the (tpa)Ag(OTf)-catalyzed intramolecular amination of sulfamates and the (dmbox)Ag(ClO_4)-catalyzed amination of carbamates.[6b,7-8] However, these previous studies cannot rule out the possibility of a stepwise pathway involving short-lived radical intermediates and rapid radical rebound to form the new C–N bond.

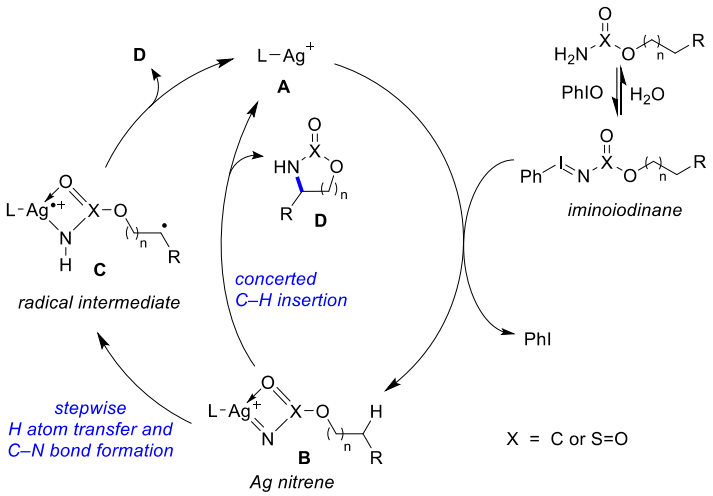

Figure 3-7 Proposed mechanisms of the Ag-catalyzed C–H amination.

To investigate the most favorable amination mechanism, we first calculated the reaction energy profile of the (dmbox)Ag(ClO_4)-catalyzed benzylic C–H amination of carbamate **1** at the ωB97X-D/def2-TZVPP, SMD(DCM)//ωB97X-D/def2-SVP–def2-TZVPP(Ag) level of theory (Figure 3-8). The reaction initiates via condensation of substrate **3-1** with PhIO to form an iminoiodinane, which coordinates to the Ag(I) pre-catalyst to form the dative complex **3-3**. The nitrene formation via PhI dissociation (**3-TS1**) requires an activation free energy of 25.7 kcal/mol. The resulting Ag nitrene **3-4** is a closed-shell singlet and is 14.6 kcal/mol less stable than **3-3**. The singlet Ag nitrene (**3-4**) favors a four-coordinate square planar geometry with strong coordination of the carbonyl oxygen to the Ag center.[96] The most favorable C–H amination pathway involves C–H insertion via an open-shell singlet transition state **3-TS2** with a relatively low barrier of 8.2 kcal/mol with respect to **3-4**.

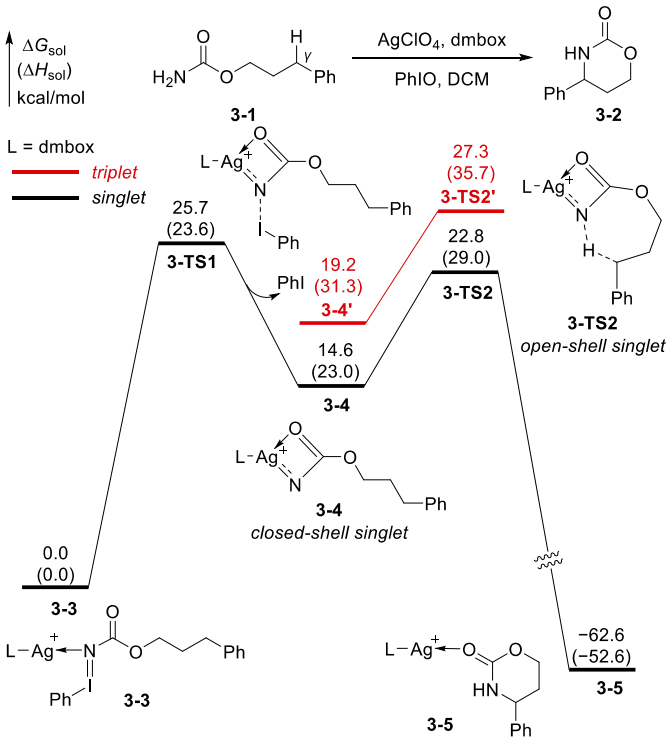

Figure 3-8 Reaction energy profile of the (dmbox)Ag(ClO4)-catalyzed C–H bond amination of carbamate 1.

Intrinsic reaction coordinate (IRC) calculations indicate that the C–H insertion (**3-TS2**) is a concerted process (Figure 3-9)—after the H-atom transfer, the C–N bond is formed spontaneously to furnish the amination product complex **3-5,** while the open-shell character rapidly diminishes. Because **3-TS2** is lower in energy than **3-TS1**, the rate-determining step of the catalytic cycle is the nitrene formation via **3-TS1**.[97] The endergonicity of nitrene formation and the high reactivity of the Ag nitrene complex in C–H insertion is consistent with the challenges associated with the isolation and characterization of Ag nitrene intermediates.[98]

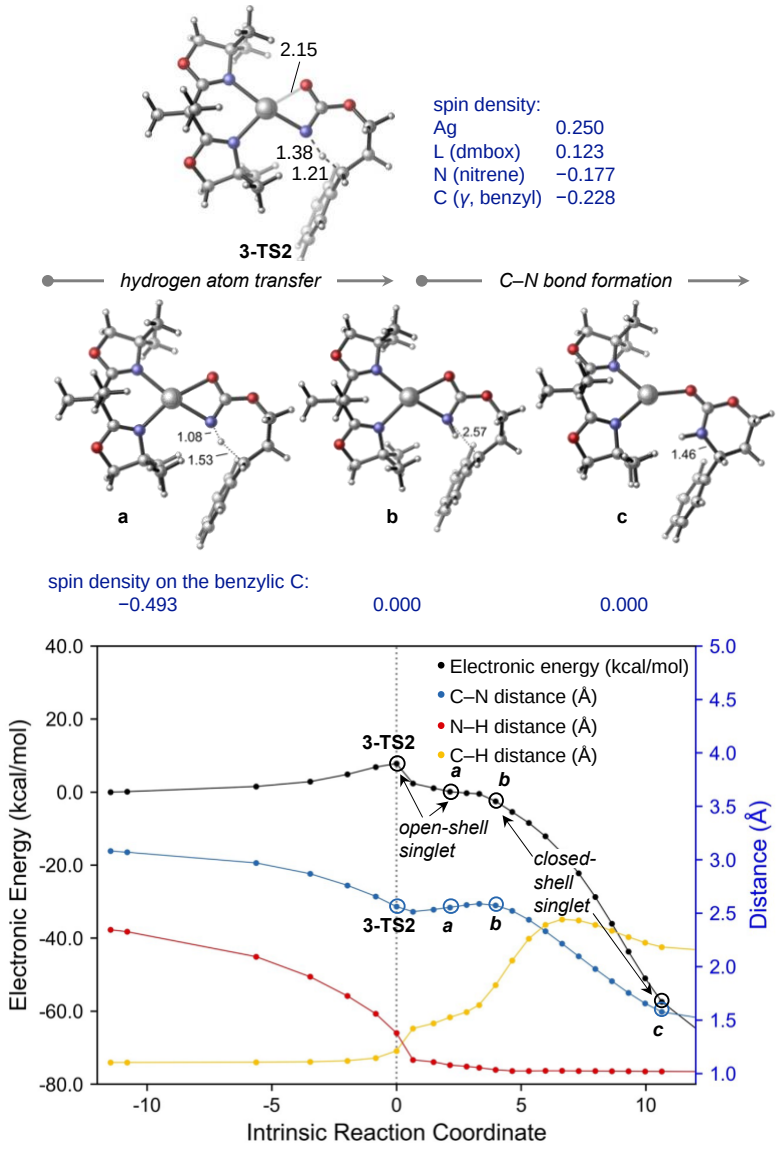

Figure 3-9 Intrinsic reaction coordinate (IRC) calculations to confirm the concerted C–H insertion process in the (dmbox)Ag(ClO4)-catalyzed C–H bond amination of carbamate 3-1.

Because previous computational studies indicated that both singlet and triplet Ag nitrene complexes may be involved in the C–H amination and alkene aziridination reactions,[84, 99] we studied the spin states of the Ag nitrene intermediate and the C–H insertion transition state using different levels of theory, including several DFT methods, explicitly correlated local coupled cluster [PNO-LCCSD(T)-F12] and complete active-space second-order perturbation theory (CASPT2) calculations (Figure 3-10). These calculations predicted that the singlet Ag nitrene (**3-**

4) and the C–H insertion transition state (**3-TS2**) are more stable than the corresponding triplet structures. At the ωB97x-D level of theory, the triplet C–H insertion transition state (**3-TS2'**) is 4.5 kcal/mol higher in energy than the open-shell singlet transition state (**3-TS2**) in the (dmbox)Ag(ClO_4)-catalyzed amination of carbamate **3-1**. The energy difference between singlet and triplet C–H insertion pathways is affected by the ancillary ligand on the Ag, as well as the identity of the nitrene precursor. Nonetheless, our PNO-LCCSD(T)-F12 and CASPT2 calculations suggest that the singlet C–H insertion pathway is more favorable for four types of Ag nitrenes supported by dmbox and tpa ligands and derived from carbamate and sulfamate precursors. Therefore, only singlet C–H insertion pathways are considered in the present study.

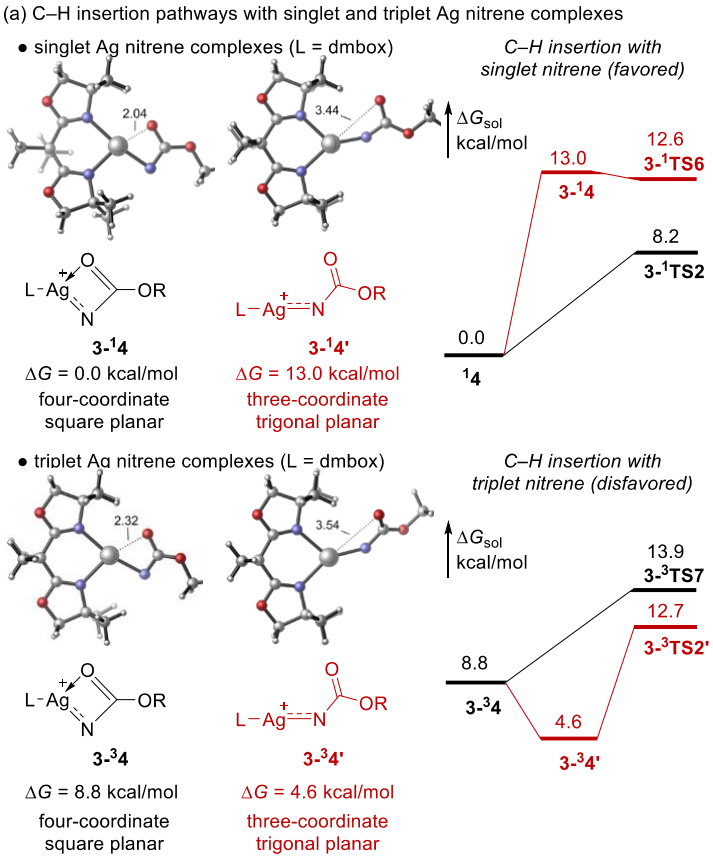

All energies are with respect to **3-^{1}4**. Part of the substrate is omitted for clarity.

(b) PNO-LCCSD(T)-F12 and CASPT2 benchmark calculations

	Δ*E* (kcal/mol)			
	3-^{1}4	**3-^{1}TS2**	**3-^{3}4'**	**3-^{3}TS2'**
ωB97X-D	0.0	5.4	7.4	15.7
B3LYP-D3	0.0	1.4	7.5	13.7
BP86-D3	0.0	−4.0	15.6	14.0
PNO-LCCSD(T)-F12	0.0	10.3	21.0	34.8
CASPT2(10,10)	0.0	8.4	31.0	36.9

Figure 3-10 Benchmark of DFT methods for of spin state energies of Ag nitrene complexes and C–H insertion transition states.

3.3.2 Catalyst-controlled Regiodivergent C–H Amination of *n*-Butyl Carbamate — A Case Study

After establishing the favored mechanism of the Ag-catalyzed intramolecular C–H amination, we chose the Ag-catalyzed C–H amination of *n*-butyl carbamate **3-6** as a model reaction

to identify factors affecting the regioselectivity. This carbamate substrate was chosen because tunable regioselectivity has been achieved experimentally for carbamate starting materials with sterically and electronically unbiased *β*- and *γ*-C–H bonds. For example, amination of a menthol-derived carbamate yielded *γ*-product selectively with a dmbox-supported Ag catalyst, while the regioselectivity is completely reversed to yield *β*-selectivity with tpa and ^{t}Bu$_3$tpy supported Ag catalysts (Figure 3-4).[6b] Although experimental studies of **3-6** have not been reported, we surmised that due to the similar steric and electronic environment of its *β*- and *γ*-C–H bonds, catalyst-controlled divergent regioselectivity may be achieved. Indeed, our DFT calculations predict that the reaction is selective for *γ*-C–H amination ($\Delta\Delta G^{\ddagger}$ = 1.5 kcal/mol) when a dmbox ligand is used, while the same reaction favors the *β*-C–H amination product ($\Delta\Delta G^{\ddagger}$ = −1.0 kcal/mol) when a tpa ligand is used instead. This computationally predicted regioselectivity trend is consistent with the catalyst-controlled selectivity in aminations of other carbamate substrates and was later validated experimentally (*vide infra*). Careful analysis of the C–H insertion transition states (**3-TS3, 3-TS4**) revealed that the main reason for the catalyst-controlled divergent regioselectivity is the different steric properties of the bidentate dmbox ligand compared to the more crowded multidentate tpa ligand. In the dmbox-supported C–H insertion transition states (**3-TS3-*γ*** and **3-TS3-*β***), ligand-substrate steric repulsions are not observed. The preference for *γ*-C–H amination can be attributed to the slightly weaker *γ*-C–H bond compared to the *β*-C–H bond (BDE = 96.8 and 98.0 kcal/mol respectively) or the difference between ring-strain energies of the six- and seven-membered cyclic transition states (see later for detailed discussion about ring strain effects). In contrast, when the more crowded tpa ligand is used, the *γ*-C–H insertion transition state (**3-TS4-*γ***) suffers from greater ligand-substrate steric repulsions as compared to the *β*-C–H insertion transition state (**3-TS4-*β***). **3-TS4-*γ*** is destabilized by steric repulsion between the carbamate carbonyl oxygen and one of the

pyridine arms on the tpa ligand (d(O···H) = 2.39 Å). The ligand–substrate steric repulsion is diminished in **3-TS4-*β***, where the carbamate carbonyl is placed further away from the ligand due to the sterically less demanding six-membered ring as compared to the seven-membered ring in **3-TS4-*γ***.

Although the ligand steric effects nicely explained the origin of divergent regioselectivity in the amination of **3-6**, a more general regioselectivity model is still needed to understand the regioselectivity control with other substrates and ancillary ligands. This is due to several other factors that may also affect the transition state stability, and thus the regioselectivity. These factors include substrate properties, such as the BDE and electronic properties of the C–H bond being activated, as well as the electronic effects of the ancillary ligand on the Ag nitrene. In particular, the donor ability of the ancillary ligand affects the amount of electron transfer from the C–H bond to the Ag nitrene and the early/lateness of the C–H insertion transition state. For example, transition states **3-TS4-*γ*** and **3-TS4-*β*** with the more electron-rich tpa ligand involve less electron transfer from the C–H bond and shorter bond distances of the cleaving C–H bond than transition states with dmbox (**3-TS3-*γ*** and **3-TS3-*β***) (Figure 3-11). Therefore, reactions with these different ligands may have different sensitivities to substrate properties, such as BDE and electronic effects.

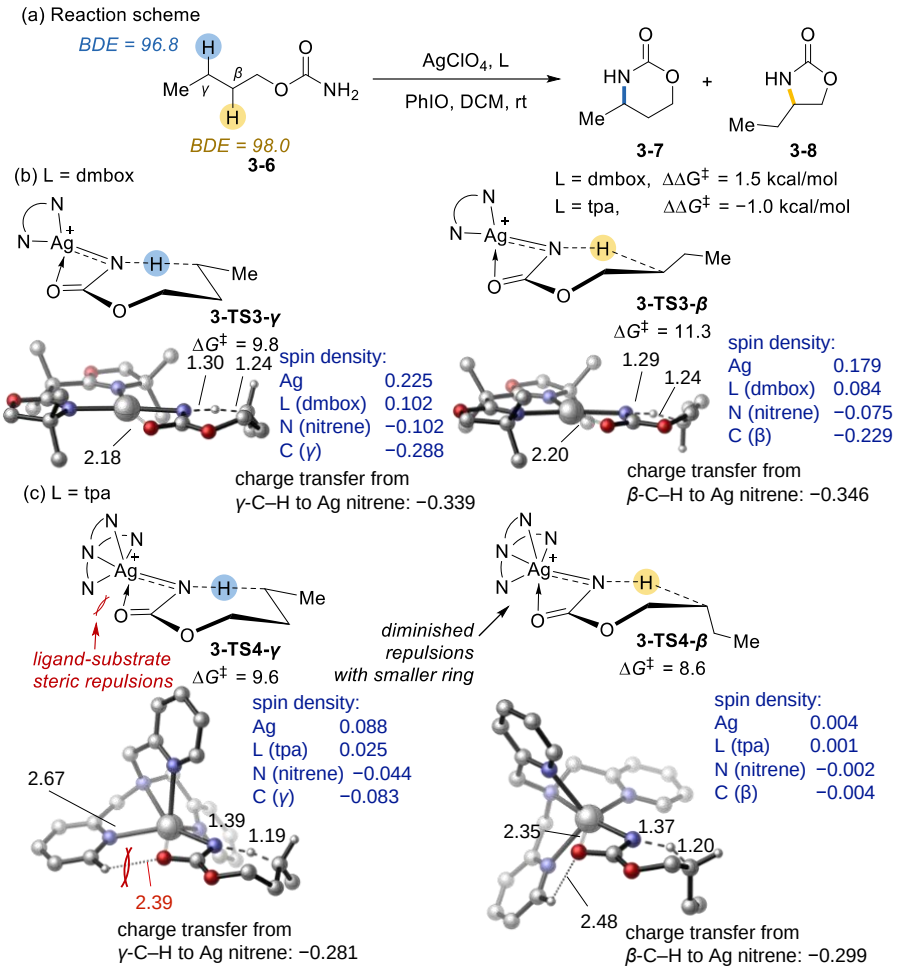

Figure 3-11 Ligand effect on regioselectivities in the Ag-catalyzed C–H amination of carbamate 3-6.

Another question that needs to be carefully evaluated is why the identity of the nitrene precursor has such a dramatic impact on the regioselectivity. While there are several examples of regiodivergent amination of either *β*- or *γ*-C–H bonds in carbamate precursors, reactions with sulfamates are often highly *γ*-selective, regardless of the ligand used. Changing the nitrene precursor from carbamate to sulfamate may affect the ring strain energy difference between the seven- and six-membered cyclic transition states [100], the catalyst-substrate non-covalent interactions, or the strength of the coordination of the carbonyl and sulfonyl groups to the Ag center. These multifaceted interactions between the Ag nitrene and the C–H bond pose a significant challenge to rationally predict the regioselectivity of the amination. On the other hand, they also

offer promising opportunities to achieve catalyst-controlled regioselectivity by fine-tuning the electronic and steric properties of the Ag nitrene. These initial computational analyses promoted us to perform a detailed investigation on how these individual factors affect the reactivity of the C–H insertion with different Ag nitrene complexes.

3.3.3 Effects of Bond Dissociation Enthalpy (BDE) on Reactivity

We computed the C–H insertion activation free energies of four different types of Ag nitrene species (**Types I-IV**) undergoing reaction with C–H bonds in substrates with various BDE values (Figure 3-12). These four types of Ag nitrenes were chosen because they include ancillary ligands with different denticities (dmbox, bidentate and tpa, tetradentate) and precursors with planar (carbamate) and tetrahedral-shaped (sulfamate) groups attached to the nitrenes. We surmised that these factors may impact the transition state geometry and ligand–substrate interactions. Here, only γ-C–H bonds are included to study BDE effects and avoid the potential impacts of tether length (the effects of tether length will be discussed later).

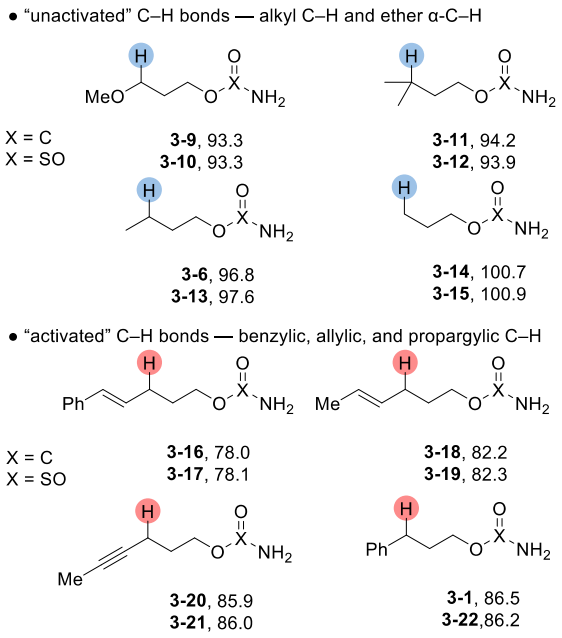

Figure 3-12 C–H bond BDEs (in kcal/mol) in carbamate (X = C) and sulfamate (X = S=O) precursors.

BDE values are often recognized as the primary factor affecting the reactivity of C–H bonds in hydrogen atom abstraction reactions, [83a,101] including nitrene transfer.[102] However, the computed activation free energies do not show good overall correlations with C–H BDE in any of the four types of Ag nitrenes studied (Figure 3-13). Instead, bimodal relationships were observed. The reactivity of alkyl and ether α-C–H bonds (named "unactivated" C–H, **3-6**, **3-9**-**3-15**) correlates well with their BDEs with moderate-to-large slopes (0.42 ~ 0.80). In contrast, the reactivity of C–H bonds adjacent to a sp^2 or sp carbon center, such as allylic, propargylic, and benzylic C–H bonds (named "activated" C–H, **3-1**, **3-16**-**3-22**), are much less sensitive to BDE (slope = −0.12 ~ 0.18). Although similar bimodal correlations have been observed in C–H oxidations using DMDO and CumO•,[103,104] the extremely low sensitivity of activated C–H bonds to BDE is a unique feature of the Ag-catalyzed amination, as transition-metal catalyzed C–H hydroxylation reactions involving metal oxo species are generally more sensitive to BDE.[103] For example, the slopes of the DMDO- and CumO•-mediated HAT with "activated" C–H bonds are 0.35 and 0.23, respectively, much larger than those in the Ag-catalyzed amination. The lower

sensitivity to BDE in reactions of activated C–H bonds with Ag nitrenes can be explained by the Hammond postulate—the highly exergonic reactions have more reactant-like transition states, in which the stability of the alkyl radical plays a less prominent role on the reaction barriers. It should be noted that the carbamate-derived Ag nitrenes (Figure 3-13, **Types I** and **II**) are completely insensitive to the BDE in reactions with activated C–H bonds. The lack of a strong influence of BDE suggests that the regioselectivity of the Ag-catalyzed amination of these activated C–H bonds is modulated by other factors, such as ligand–substrate steric repulsions or dispersion interactions, to override the intrinsic preference for reaction based on simple bond strengths.

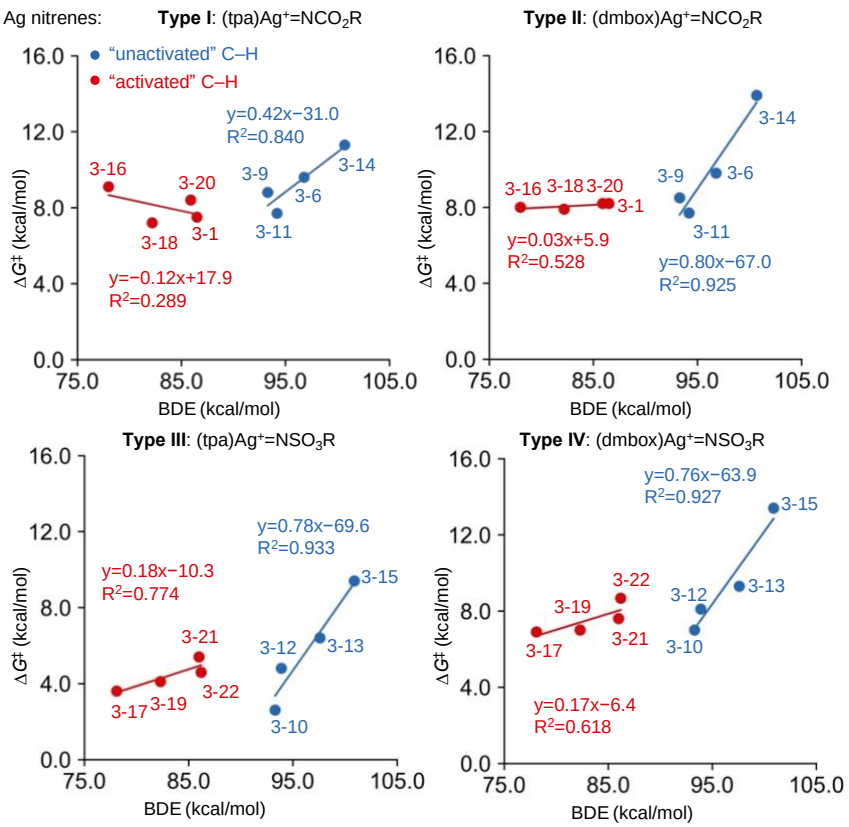

	Type I	Type II	Type III	Type IV
ligand	tpa	dmbox	tpa	dmbox
precursor	carbamate	carbamate	sulfamate	sulfamate
sensitivity to BDE of "unactivated" C–H bonds†	0.42	0.80	0.78	0.76
sensitivity to BDE of "activated" C–H bonds†	−0.12	0.03	0.18	0.17

† Sensitivity is derived from the slope of the correlation between $\Delta G^{\ddagger}$ and C–H BDE.

Figure 3-13 Effects of C–H BDE on the activation free energies of C–H insertion with different Ag nitrene complexes derived from carbamate and sulfamate precursors.

In reactions with unactivated C–H bonds, the reactivity is more sensitive to C–H BDEs as these reactions are less exergonic and generally have later transition state structures with longer C–H bond distances (Table 3-1). Another interesting trend revealed by Figure 3-13 is that the reactions with tpa-supported Ag nitrenes derived from carbamate precursors (**Type I**) are the least sensitive to C–H BDE in reactions with unactivated C–H bonds. In these reactions, a moderate slope of 0.42 was obtained, compared to the slopes of ~0.8 in the reactions of unactivated C–H

bonds with the other three types of Ag nitrenes (**Types II-IV**). These results suggest that the Ag(tpa)-catalyzed reactions with carbamates are less sensitive to the strength of unactivated C–H bonds. Thus, this catalyst system offers the best chance to override the BDE effect to selectively activate a stronger unactivated C–H bond and promote reactivity of primary C–H bond amination by fine-tuning other factors controlling the TS stability.

Table 3-1 C−H bond distances in the C−H insertion transition states.

Type I: (tpa)Ag^{+}=NCO_2R		**Type II**: (dmbox)Ag^{+}=NCO_2R		**Type III**: (tpa)Ag^{+}=NSO_3R		**Type IV**: (dmbox)Ag^{+}=NSO_3R	
Mol	$d_{C\text{-}H}$(**TS**)	Mol	$d_{C\text{-}H}$(**TS**)	Mol	$d_{C\text{-}H}$(**TS**)	Mol	$d_{C\text{-}H}$(**TS**)
3-9	1.16	**3-9**	1.20	**3-10**	1.16	**3-10**	1.19
3-11	1.17	**3-11**	1.20	**3-12**	1.17	**3-12**	1.21
3-6	1.19	**3-6**	1.24	**3-13**	1.18	**3-13**	1.23
3-14	1.27	**3-14**	1.31	**3-15**	1.21	**3-15**	1.27
3-16	1.16	**3-16**	1.19	**3-17**	1.15	**3-17**	1.18
3-28	1.17	**3-28**	1.20	**3-19**	1.15	**3-19**	1.19
3-20	1.20	**3-20**	1.23	**3-21**	1.18	**3-21**	1.22
3-1	1.18	**3-1**	1.21	**3-22**	1.16	**3-22**	1.20

[a]Bond distances are in Å.

3.3.4 Effects of Tether Length on Reactivity and Selectivity

Next, we investigated the effects of tether length, i.e. whether the C–H bond is located at the *β*- or *γ*-position of the carbamate or sulfamate precursor, on the regioselectivity of C–H insertion. Although the computed regioselectivity of the amination of *n*-butyl carbamate **3-6** is strongly influenced by the ligand (Figure 3-11), the amination of *n*-butyl sulfamate **3-13** is

predicted to be highly γ-selective in reactions with both tpa- and dmbox-supported Ag nitrenes ($\Delta\Delta G^{\ddagger}$ = 3.9 and 6.8 kcal/mol, respectively). As the β-C–H bond in **3-13** is only 1.2 kcal/mol stronger than the γ-C–H bond, the slopes of the correlations between $\Delta G^{\ddagger}$ and C–H BDE in these two types of reactions (0.78 and 0.76 with "unactivated" C–H bonds in **Types III** and **IV** Ag nitrenes, Figure 3-12) predict a moderate γ-regioselectivity ($\Delta\Delta G^{\ddagger} \approx 1.0$ kcal/mol) as a result of the BDE effects. Clearly, factors other than the BDE difference dominate the γ-selectivity for the reaction with sulfamate **3-13**. The effectiveness of sulfamates in facilitating a seven-membered ring 1,6-HAT to selectively functionalize γ-C–H bonds[105] prompted us to evaluate how the geometrical features of the sulfamate affect the stability of the six-[106] and seven-membered TS in the β- and γ-C–H amination pathways, respectively. In C–H insertion transition states with sulfamate-derived Ag nitrenes (*e.g.* **3-TS5-*γ*** and **3-TS5-*β***, Figure 3-14), the seven- and six-membered rings adopt chair-like and envelop-like geometries, respectively. While the chair-like seven-membered ring in **3-TS5-*γ*** is not strained, substantial strain is present in the envelop-like six-membered ring in **3-TS5-*β***. In particular, in **3-TS5-*β***, the N–H bond in the six-membered ring is not co-planar with the Ag nitrene, furnishing a non-ideal angle for the nitrene C–H abstraction. In addition, the envelop conformation in **3-TS5-*β*** leads to greater repulsion with the Ag center because of the concave shape of the bicyclic structure.[107] The strain of the concave bicyclic system in **3-TS5-*β*** causes partial dissociation of the sulfonyl coordination to Ag (d(O···Ag) = 2.28 Å, whereas d(O···Ag) is 2.18 Å in **3-TS5-*γ***). In transition states with the carbamate-derived Ag nitrenes (Figure 3-10), because of the planar geometry of the carbamate group, the seven- and six-membered rings in **3-TS3-*γ*** and **3-TS3-*β*** are nearly co-planar with the Ag catalyst. Thus, the strain in the fused bicyclic system involving carbamate is diminished.

Taken together, the computed transition state structures and energies indicate that high γ-selectivity in the Ag-catalyzed amination of *n*-butyl sulfamate **3-13** is due to destabilization of the β-C–H insertion transition state by the ring strain of the fused bicyclic structure with the six-membered ring. In contrast, ring strain effects are diminished in the amination with *n*-butyl carbamate **3-6** because the planar geometry of the carbamate leads to small ring strain in both the β- and γ-C–H insertion transition states.

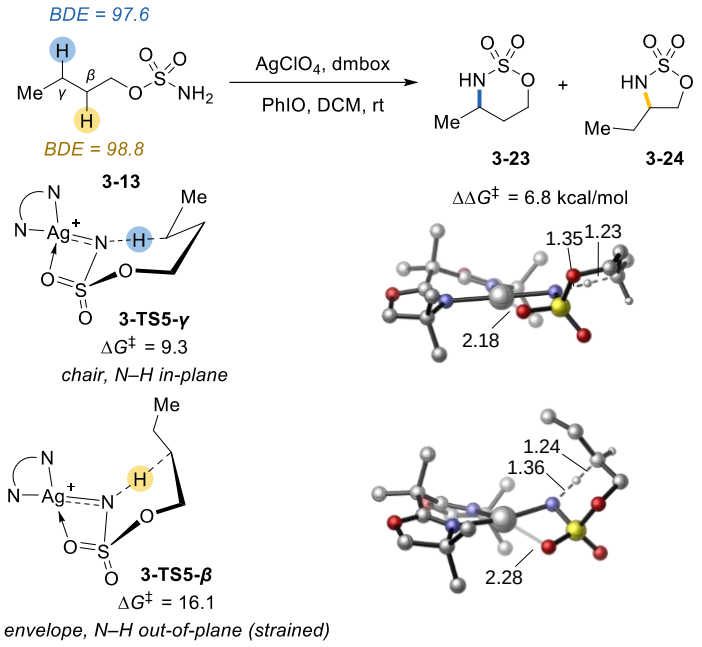

Figure 3-14 Effects of tether length on the regioselectivity of C−H amination of sulfamate 3-13 catalyzed by a dmbox-supported Ag catalyst.

To investigate whether the different tether length effects between carbamate and sulfamate precursors are applicable to other substrates and to explore whether the ancillary ligand on Ag influences the tether length effect, we computed the C–H insertion activation free energies with various β- and γ-C−H bonds in **Type I-IV** Ag nitrene complexes. These substrates include secondary alkyl C–H bonds and "activated" C–H bonds, where the C–H BDEs have small effects on their relative reactivities. For each intramolecular C–H insertion transition state, we also computed a hypothetical, unstrained acyclic C–H insertion transition state (Figure 3-15). In this

manner, we can use the reaction enthalpies of the homodesmotic reactions[108] shown in Figure 3-15 to compute the ring strain energy (ΔH_s) of each cyclic C–H insertion transition state.

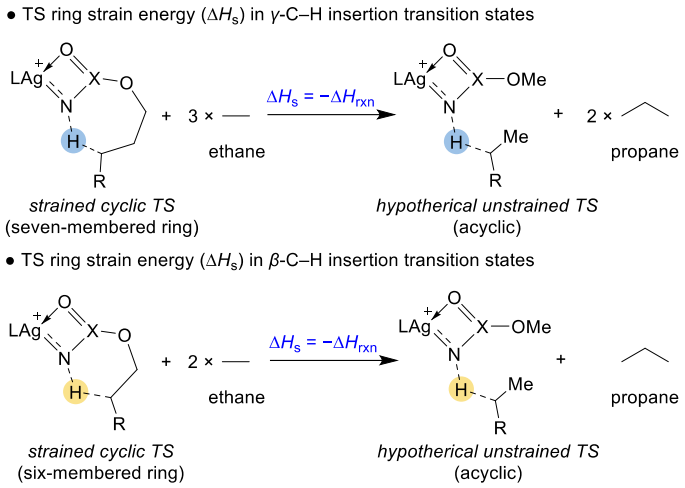

Figure 3-15 Homodesmotic reactions to calculate ring strain energies (ΔHs) of cyclic C–H insertion transition states.

The computed activation free energies and transition state ring strain energies (Figure 3-16) indicate that the γ-C–H insertion is often favored, but the γ-selectivity is significantly affected by both the identity of the precursor and the ancillary ligand on Ag. Among the four types of Ag nitrenes, (dmbox)Ag nitrenes derived from sulfamates (**Type IV**) have the greatest γ-selectivity—the β-C−H insertion transition states with these complexes suffer from significant ring strain energies ($\Delta H_{s(\text{ave-}\beta)}$ = 8.6 ± 2.0 kcal/mol), while the γ-C−H insertion transition states are not strained ($\Delta H_{s(\text{ave-}\gamma)}$ = 0.3 ± 0.5 kcal/mol). In the reactions with tpa-supported sulfamate-derived Ag nitrenes (**Type III**) and dmbox-supported carbamate-derived Ag nitrenes (**Type II**), the γ-selectivity is lower, due to decreased ring strain in the β-C−H insertion transition states. Finally, the preference for γ-C−H insertion is completely diminished in tpa-supported carbamate-derived Ag nitrenes (**Type I**), because the β- and γ-C−H insertion transition states have comparable ring strain energies. The good correlations between ΔH_s and $\Delta G^{\ddagger}$ in the reactions with **Types II-IV** Ag nitrenes indicate that ring strain in the cyclic transition states plays a significant role on the

reactivity and regioselectivity of C–H insertion. Based on the slopes of the correlations between ΔH_s and $\Delta G^{\ddagger}$ (i.e., sensitivity to ΔH_s) and the average ΔH_s for β- and γ-C−H insertion transition states, we can estimate the average preference for γ-C−H insertion is 8.0 kcal/mol for **Type IV**, 3.8 kcal/mol for **Types II-III**, and 0.0 kcal/mol for **Type I** Ag nitrenes. This general trend suggests that the magnitude of tether length effects is affected by both the ancillary ligand and the precursor. While **Type IV** nitrenes have the greatest preference for γ-C−H insertion because of the strain of the concave bicyclic β-C−H insertion TS with this type of Ag nitrene, the β-C−H insertion TS is less strained when the bidentate dmbox ligand is replaced with a multidentate tpa ligand in **Type III** nitrenes, which weakens the sulfonyl−Ag coordination. For nitrenes containing the planar carbamate group (**Types I and II**), the β-C−H insertion TSs are also less strained because they do not have the concave geometry. The lack of ring strain effects in the reactions with **Type I** Ag nitrenes makes this type of reactions especially promising for activating β-C–H bonds. These system-dependent tether length effects, combined with other factors that promote selective β-C–H amination, such as ligand-substrate steric repulsions with multidentate ligands (*vide supra*),[109] provide a general platform for regiodivergent C–H amination for a broad range of substrates.

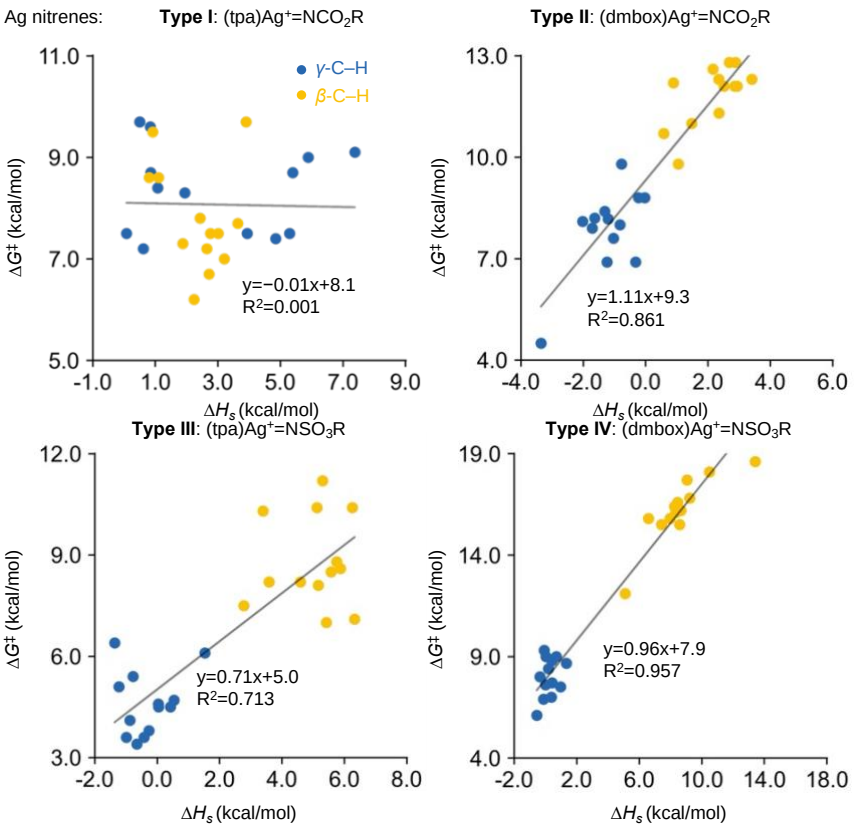

		no preference		*strongly favor γ*	
		Type I	**Type II**	**Type III**	**Type IV**
ligand		tpa	dmbox	tpa	dmbox
precursor		carbamate	carbamate	sulfamate	sulfamate
sensitivity to transition state ring strain (ΔH_s)†		−0.01	1.11	0.71	0.96
Average ΔH_s in *β*-C–H insertion TS ($\Delta H_{s(ave\text{-}\beta)}$)		2.4 ± 1.0	2.2 ± 0.9	5.0 ± 1.1	8.6 ± 2.0
Average ΔH_s in *γ*-C–H insertion TS ($\Delta H_{s(ave\text{-}\gamma)}$)		3.0 ± 2.5	−1.2 ± 0.9	−0.3 ± 0.8	0.3 ± 0.5
Average preference for *γ*-C–H insertion $\Delta\Delta G^{‡}$ = sensitivity × ($\Delta H_{s(ave\text{-}\beta)} - \Delta H_{s(ave\text{-}\gamma)}$)		0.0	3.8	3.8	8.0

† Sensitivity is derived from the slope of the correlation between $\Delta G^{‡}$ and ΔH_s

Figure 3-16 Effects of tether length on transition state ring strain energy (ΔH_s) and activation free energies ($\Delta G^{‡}$) of the β- and γ-C–H insertion with different Ag nitrene complexes.

3.3.5 Electronic Effects of the C–H Bond on Reactivity

The charge transfer from the C–H bond to the Ag nitrene in the C–H insertion transition states (Figure 3-17) indicates an electrophilic C–H amination mechanism that favors more

electron-rich C–H bonds.[110] To evaluate whether the different types of Ag nitrenes have different sensitivity to the electronic effects, we computed the activation free energies of a series of benzylic C–H bonds with **Types I-IV** Ag nitrenes (Figure 3-17). The four different types of Ag nitrenes all react faster with more electron-rich C–H bonds. Correlations of computed relative rate constants with the σ^+ parameters gave comparable slopes for all four types of nitrenes. These results indicate that the different Ag nitrenes have similar electrophilicity when reacting with the C–H bonds. The computationally-derived slope for **Type III** Ag nitrenes (−0.68) is in good agreement with the experimental Hammett studies with the (tpa)Ag(OTf)-catalyzed intramolecular competition of diaryl sulfamates, which gave a ρ of −0.69 using σ_p^+ parameters.[8,111]

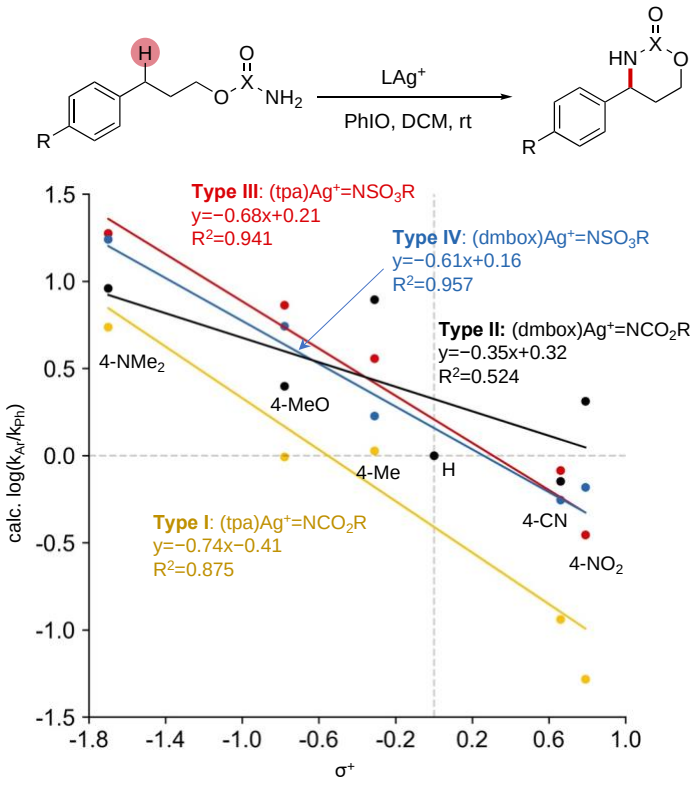

Figure 3-17 Hammett plot

Good correlations between the computed activation free energies and NPA charges of the benzylic H atoms (Figure 3-18) suggest that the partial atomic charges of the substrates may be

used to describe the reactivity preference for more electron-rich C–H bonds in the amination reactions.

	NPA charge (H)	
	X = C	X = S=O
R = NMe_2	0.214 (**3-25**)	0.215 (**3-26**)
MeO	0.216 (**3-27**)	0.217 (**3-28**)
Me	0.214 (**3-29**)	0.215 (**3-30**)
H	0.215 (**3-1**)	0.216 (**3-22**)
CN	0.220 (**3-31**)	0.222 (**3-32**)
NO_2	0.221 (**3-33**)	0.222 (**3-34**)

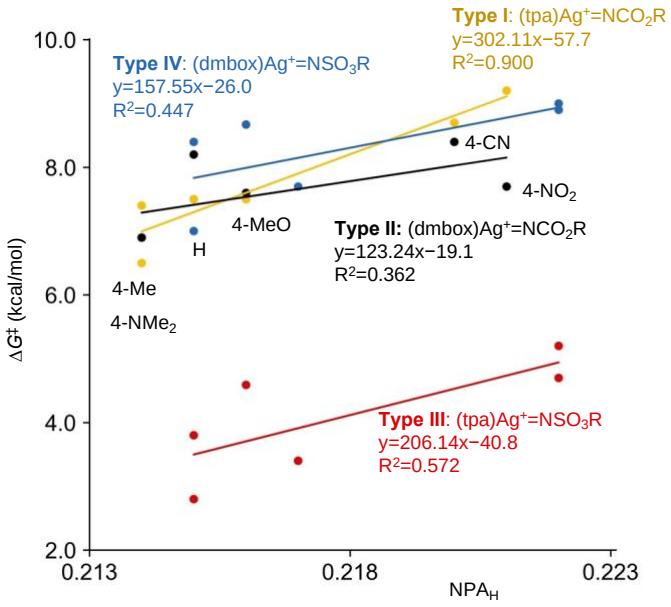

Figure 3-18 Correlation between activation free energy and NPA charge of the H atom

3.3.6 Summary of Catalyst-Dependent Factors on Reactivity and Regioselectivity

The computational results discussed above revealed that the regioselectivity of the Ag-catalyzed C–H amination is controlled by various factors, including BDE and electronic properties of the C–H bonds, tether length, and ligand–substrate steric repulsions. We summarized the sensitivity to each of these effects for the four different types of Ag nitrenes (Figure 3-19). Understanding the effects of different substrate parameters on regioselectivity with a given type

of Ag nitrenes is valuable for the design of regiodivergent C–H aminations. For example, although all four types of Ag nitrenes prefer "unactivated" C–H bonds with lower BDEs, the lower sensitivity in reactions with tpa-supported carbamate-derived Ag nitrenes (**Type I**) makes them the best catalyst system to pursue the selective functionalization of relatively strong unactivated C–H bonds. By contrast, amination of "activated" C–H bonds is not sensitive to BDE when carbamate precursors are used (**Types I-II**). This offers plenty of opportunities to override the BDE preference to aminate a relatively strong C–H bond in the presence of a weaker "activated" C–H bond. The strong preference for *γ*-selectivity using **Type IV** Ag nitrenes makes the (dmbox)Ag(I)-catalyzed reactions of sulfamates suitable for *γ*-C–H amination. By contrast, the tpa-supported carbamate-derived Ag nitrenes (**Type I**) favor amination of *β*-C–H over *γ*-C–H bonds, if other factors are equal, due to ligand steric effects. Finally, more electron-rich C–H bonds are preferred, regardless of the ancillary ligand and the nitrene precursor. As discussed above, the different reactivities of the Ag nitrenes are mainly affected by the ligand denticity and whether a sp^2-hybridized trigonal planar atom or a sp^3-hybridized tetrahedral atom is attached to the nitrene. Therefore, we expect that the same reactivity trends should also apply in Ag-catalyzed C–H amination with other ancillary ligands and precursors.

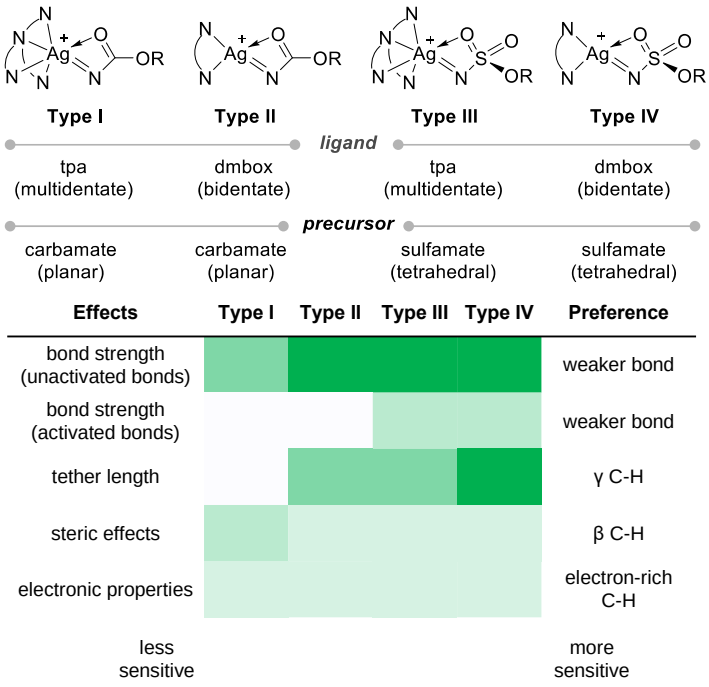

Figure 3-19 Catalyst-dependent sensitivity of C–H insertion barriers to different substrate properties.

3.3.7 Experimental Validation of Factors Affecting Regioselectivity

To validate the different selectivity-determining factors summarized in Figure 3-18, we analyzed the regioselectivity of various Ag-catalyzed C–H amination reactions reported in the literature. Our collaborator, Emily E. Zerull from the Schomaker's group, performed new experiments when the regioselectivity results were not available. We compared the *β*/*γ*-selectivity in the amination of *n*-butyl carbamate (**3-6**), *n*-butyl sulfamate (**3-13**) (Figure 3-20), and menthol-derived carbamate (**3-35**) and sulfamate (**3-36**) (Figure 3-20). In these substrates, the *β*-C–H bonds have slightly higher BDE than the *γ*-C–H bonds. According to the factors shown in Figure 3-19, *γ*-C–H amination is expected to be strongly preferred in the (dmbox)Ag-catalyzed reactions with sulfamates (**Type IV**), due to ring strain energy effects, while *β*-C–H amination should be preferred in the (tpa)Ag-catalyzed reaction with carbamates (**Type I**) due to ligand–substrate steric

repulsions. Indeed, the experimentally observed product ratios agree well with this general selectivity trend and the computationally predicted regioselectivities. The amination of *n*-butyl carbamate (**3-6**) using tpa ligand gave excellent *β*-selectivity ($\gamma : \beta < 1 : 20$). The regioselectivity with the same substrate is completely reversed to favor *γ*-amination product in a 6:1 ratio when dmbox ligand is used in place of tpa (see Figures 3-11 and 3-14 for computed TS structures and the origin of the catalyst-controlled divergent regioselectivity).

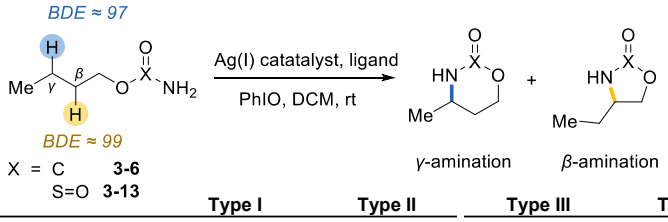

	Type I	Type II	Type III	Type IV
precursor	carbamate (**3-6**)		sulfamate (**3-13**)	
ligand	tpa	dmbox	tpa	dmbox
exp. ratio (γ : β)	< 1 : 20	6 : 1	-	-
$\Delta\Delta G_{DFT}^{\ddagger}$ (kcal/mol)	−1.0	1.5	3.9	6.8
Dominant factors:	*ligand-substrate steric repulsion*			*tether length BDE*
Selectivity preference:	*favor β*			*favor γ*

Figure 3-20 Experimental and computational studies of catalyst-controlled regiodivergent *β*/*γ*-selectivity. Experimental studies were performed by Emily Zerull at the University of Wisconsin.

Although reactions using *n*-butyl sulfamate (**3-13**) under standard conditions failed to give the desired amination product due to substrate decomposition and side reactions, in the reactions with menthol-derived sulfamate (**3-36**), excellent *γ*-selectivity was obtained (Figure 3-21). These new experimental results confirmed the strong preference for *γ*-amination products for **Types III** and **IV** Ag nitrenes. The computational results also agree with the previously reported catalyst-controlled regiodivergent amination of carbamate **3-35**[6b]—when bidentate ligands such as dmbox and Me_4phen are used, the **Type II** Ag nitrenes gave moderate *γ*-selectivity; in contrast, reactions using multidentate tpa **Type I** Ag nitrenes) favored *β*-product. The effect of ligand-to-Ag ratio on the regioselectivity with Me_4phen-supported Ag catalyst is also consistent with this trend—when

a 1:1 ratio of Me_4phen:Ag was used, the **Type II** Ag nitrene supported by the bidentate ligand (**3-38**) gave *γ*-product; when an excess of Me_4phen ligand is used, two Me_4phen ligands are expected to bind to the Ag, and thus a **Type I** Ag nitrene (**3-37**) would lead to preferred *β*-amination product. These validation experiments supported the strategies discussed above to achieve catalyst-controlled tunable *β*-/*γ*-regioselectivity by altering the ligand denticity and precursor identity.

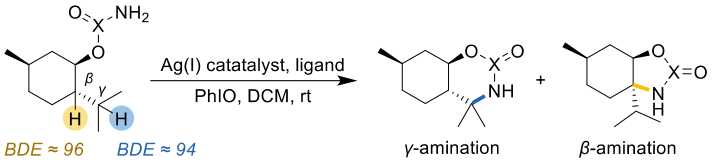

	Type I		Type II		Type III	Type IV
precursor	carbamate (**3-35**)				sulfamate (**3-36**)	
ligand	bis(Me_4phen) (**3-37**)	tpa	Me_4phen (**3-38**)	dmbox	tpa	dmbox
ligand denticity	4	4	2	2	4	2
exp. ratio (γ : β)	< 1: 20	1 : 4	4 : 1	6 : 1	> 20 : 1	> 20 : 1
$\Delta\Delta G_{DFT}^{\ddagger}$ (kcal/mol)	−2.5	−2.4	0.2	0.1	5.6	7.4
Dominant factors:	*ligand-substrate steric repulsion*					*tether length BDE*
Selectivity preference:	*favor β*					*favor γ*

Ag nitrenes supported by one and two Me_4phen ligands

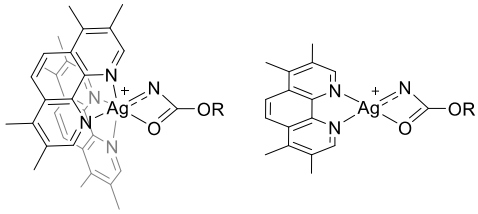

3-37 **3-38**

Figure 3-21 Experimental and computational studies of catalyst-controlled regiodivergent *β*/*γ*-selectivity. Experimental studies were performed by Emily Zerull at the University of Wisconsin.

Next, we compared the computed substrate BDE and electronic effects on reactivity with experimental results. Intramolecular competition experiments have been reported to study the reactivities of benzylic and other "activated" C–H bonds in the (tpa)Ag(OTf)-catalyzed amination of sulfamates that involve **Type III** Ag nitrenes (Figure 3-22).[8, 85] These reactions are expected to have small-to-moderate sensitivity to the BDE and electronic properties of the C–H bonds (Figure 10). Both the experimentally observed regioselectivity (Figure 3-22a-b) and the computationally

predicted activation free energies support these conclusions. A good agreement between the experimental and DFT-calculated regioselectivity was obtained (Figure 3-22c).

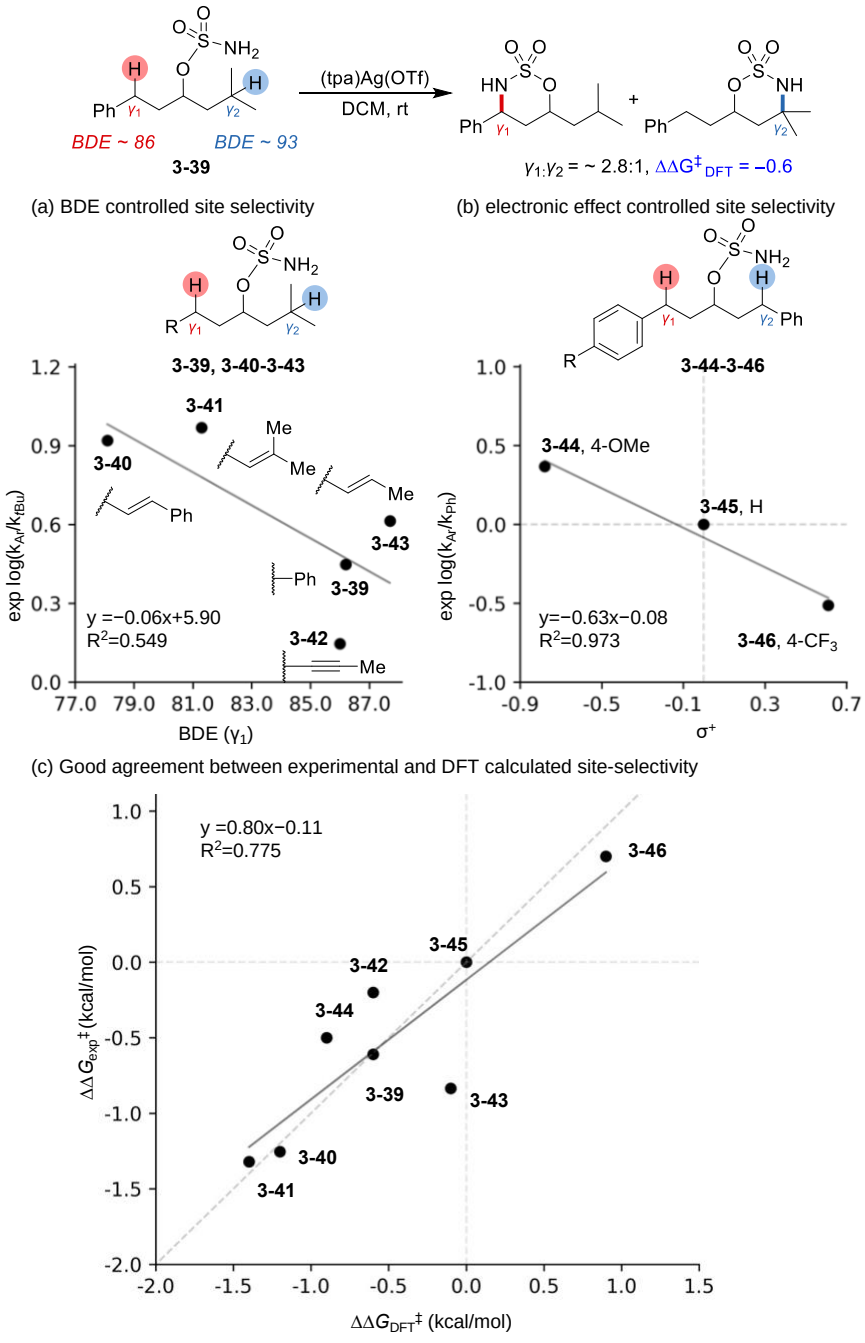

Figure 3-22 Validation of substrate BDE and electronic effects on regioselectivity.

3.4 Conclusion

A combined computational and experimental study was performed to investigate why different types of Ag nitrene intermediates lead to different regioselectivities in the Ag-catalyzed C–H amination. These insights can be used to predict regiodivergent amination of a diverse range of C–H bonds. The computational studies indicated that the Ag-catalyzed intramolecular C–H amination reaction proceeds via a concerted H-atom transfer/C–N bond formation process involving singlet Ag nitrene intermediates. The ancillary ligand and the identity of the nitrene precursor (carbamate vs sulfamate) affect the transition state geometry, and thus ring strain in the intramolecular C–H insertion and ligand–substrate steric repulsions. These transition state geometry differences lead to distinct sensitivities of C–H insertion barriers to the different substrate properties, such as tether length, BDE and electronic effects of C–H bonds, and steric repulsions.

The sensitivities to these different effects were investigated for four representative types of Ag nitrenes supported by either a bidentate (i.e. dmbox) or a multidentate (i.e. tpa) ligand and derived from precursors with either a trigonal planar (i.e. carbamate) or a tetrahedral (i.e. sulfamate) atom attached to the nitrene nitrogen. We demonstrated how these reactivity rules can be used to select the best catalyst system to achieve the desired regioselectivity. For example, the Ag-catalyzed aminations with the bidentate dmbox ligand and sulfamate precursors strongly favor γ-C–H bonds. This regioselectivity is reversed by using a tpa-supported Ag catalyst with carbamate precursors. In addition, the (tpa)Ag(OTf)-catalyzed amination of unactivated C–H bonds in carbamate precursors is the least sensitive to the BDE effect. Therefore, this is the most effective catalyst system to promote amination of C–H bonds with stronger BDEs in the present of weaker BDE C–H bonds.

Overall, this study revealed how the ancillary ligand and precursor affect the stability of the C–H amination transition state and thus can be rationally selected to control the regioselectivity in the Ag-catalyzed C–H aminations. We expect that the interplay of these ring strain, electronic, and steric effects can offer unique insights to guide future design of regiodivergent functionalization strategies and facilitate the catalyst design on challenging C–H amination reactions.

4.0 Engineered P450 Atom Transfer Radical Cyclases Are Bifunctional Biocatalysts: Reaction Mechanism and Origin of Enantioselectivity

4.1 Introduction

Due to their ability to exert exquisite stereocontrol over challenging chemical reactions, enzymes are excellent catalysts for asymmetric synthesis in applications that range from small-scale synthesis to industrial manufacturing.[112] Traditional biocatalysis research focuses on the discovery, engineering, and application of naturally existing enzyme functions of outstanding synthetic value. However, compared to the immensely diverse range of organic reactions discovered and optimized by synthetic chemists, only a small subset of these reactivity patterns is found in natural enzymology and are currently being utilized by biocatalysis practitioners, thus imposing a major limitation on the utility of contemporary enzyme technologies. The implementation of unnatural chemistries by repurposing naturally existing enzymatic machineries promises to expand the reaction space of biocatalysis, thereby significantly augmenting the synthetic chemist's toolbox.[113]

Recently, the Yang group at the University of California, Santa Barbara reported experimental studies to repurpose naturally occurring metalloenzymes to catalyze unnatural stereoselective radical reactions using a metalloredox mechanism.[10] Almost 50% of naturally occurring proteins are metalloproteins,[114] among which redox-active first-row transition-metal cofactors such as Fe(II)/Fe(III),[115] Co(I)/Co(II),[116] and Cu(I)/Cu(II)[117] are ubiquitous. Cognizant of the tremendous synthetic potential of these metalloproteins in facilitating redox-mediated radical reactions, the Yang group recently repurposed cytochromes P450, a class of promiscuous metalloenzymes with numerous applications,[115a-b,118-119] to catalyze new-to-nature atom transfer radical cyclization (ATRC) in an enantio- and diastereodivergent fashion (Figure 4-1).[10] Due in large part to the difficulties in maintaining a tight association with the free radical intermediate and/or the unfunctionalized olefin, inducing high levels of stereocontrol for free radical-mediated

olefin functionalization reactions continues to pose a formidable challenge for chiral small-molecule catalysts.[11] In particular, catalytic asymmetric ATRC reactions remain rare.[12] Thus, the evolved P450 atom transfer radical cyclases provide a new means of taming radical intermediates for a synthetically valuable but underdeveloped class of asymmetric transformations. This metalloredox strategy is complementary to the elegant work of Hyster[120] and Zhao[121] on reductive C–C bond forming photoredox transformations using flavoenzymes, as the metallocofactor in this work allows redox-neutral atom transfer reactions to proceed with excellent stereocontrol.

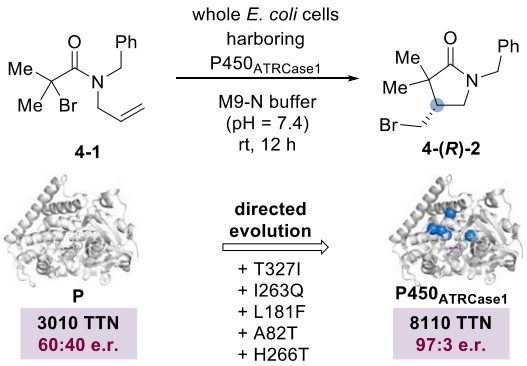

Figure 4-1 P450-catalyzed enantioselective atom transfer radical cyclization (ATRC).

To further advance this recently developed mode of metalloredox radical biocatalysis, it is imperative to gain further understanding of reaction mechanism and origin of enzyme-controlled stereoselectivity. The proposed mechanism of this enzymatic ATRC reaction involves radical initiation via bromine atom transfer from the substrate to the heme cofactor, enantioselective radical cyclization, and bromine atom rebound to form the product (Figure 4-2a). However, several key mechanistic questions remain unaddressed. First, previous work from the Yang group showed that evolved P450 radical cyclases displayed substantially faster kinetics and higher total turnover numbers relative to free cofactor in promoting this ATRC process,[10] but the origin of this enhanced activity is unclear. Second, the mode of enantioinduction for this radical-mediated olefin functionalization is potentially distinct from those of other types of well-established natural and

unnatural enzymatic reactions and remains to be uncovered. How these enhancements in reactivity and stereoselectivity relate to key evolved structural elements of the ATRCase needs to be elucidated.

Stereocontrol of many enzymatic olefin functionalization reactions has been rationalized through π-facial selectivity models based on ground-state structure of enzyme–substrate complexes,[121a, 122] where the rotational freedom of the olefin is greatly reduced and the two prochiral π-faces are easily differentiated. Such intuitive substrate binding models obtained from experimental X-ray structures and computational substrate docking and/or classical MD simulations have been widely used in biocatalysis and protein engineering. Nevertheless, an increasing number of studies underscored the importance of interrogating transition-state models to gain an accurate understanding of enzymatic stereoselectivities,[123-124] especially when the reactive functional group of the substrate (e.g., an olefin) does not strongly interact with the protein scaffold and is flexible in the enzyme–substrate complex (Figure 4-2b). In this situation, substrate binding models become ineffective, and computational models based on transition-state analysis are critical to describe the origin of enzymatic stereocontrol. In the recently developed biocatalytic enantioselective ATRC, it is not clear which enantioinduction scenario is operative. Depending on the conformational flexibility of the olefin moiety and the carbon-centered radical in the enzyme active site, the enantioselectivity may be rationalized by substrate binding conformation or by the π-facial selectivity of the radical cyclization transition state (Figure 4-2b).

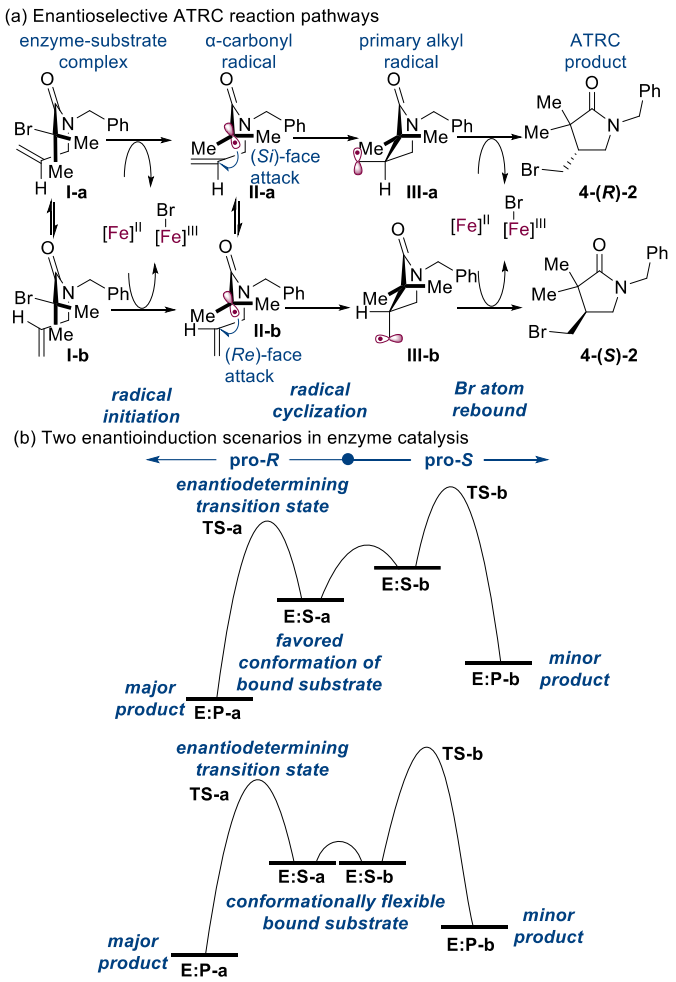

Figure 4-2 Possible mechanisms of enantioinduction in enantioselective ATRC reaction

Herein, we performed computational studies to investigate the reaction mechanism and key factors promoting this new-to-nature atom transfer radical cyclization and to explore the origin of enantioselectivity. We studied how interactions with active site residues facilitate the substrate activation step, leading to faster radical initiation. To compare the two enantioinduction scenarios (Figure 4-2b), we examined substrate binding modes and conformational flexibility of the olefin in the enzyme–substrate complex and the radical intermediate via classical MD simulations and hybrid quantum mechanics/molecular mechanics (QM/MM) metadynamics simulations. These ground state behaviors are compared with transition state enantiocontrol by computing the selectivity-determining radical cyclization transition states via QM/MM-optimizations and

QM/MM metadynamics[27,44] simulations. Our work revealed the highly flexible nature of the olefin in the enzyme–substrate complex, clearly demonstrating that enantiocontrol is governed by transition-state stability and not substrate conformational control upon binding.

This study unveiled the unexpected role of a glutamine residue (Q263) acting as the hydrogen bond donor[20a,121a,125] to activate the substrate toward radical initiation and enhance the enantioselectivity in radical cyclization (Figure 4-3). The importance of this key residue in promoting reactivity and selectivity was then validated experimentally using enzyme variants derived from site-directed mutagenesis. Together, these studies showed that the directed evolution efforts from the Yang group led to the serendipitous discovery of a bifunctional biocatalyst, wherein the heme cofactor enables atom transfer radical biocatalysis and the hydrogen bond donor residue further activates the substrate and enhances the enantioselectivity.

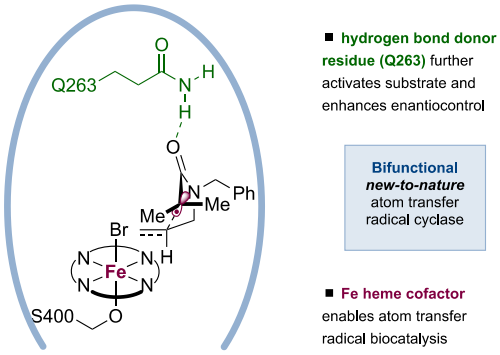

Figure 4-3 Key activation and enantiocontrol modes of P450$_{ATRCase1}$

4.2 Computational Methods

4.2.1 DFT Calculations

All density functional theory (DFT) calculations were carried out using the Gaussian 16 program.[32] Geometries of intermediates and transition states were optimized using the dispersion-corrected (U)B3LYP-D3 functional[126] with a mixed basis set of LANL2DZ for Fe and 6-31G(d) for other atoms in the gas phase. Vibrational frequency calculations were performed for all stationary points to confirm if each optimized structure is a local minimum or a transition state structure. All optimized transition state structures have only one imaginary (negative) frequency, and all minima (reactants, products, and intermediates) have no imaginary frequencies. The (U)B3LYP-D3 functional with a mixed basis set of LANL2TZ(f)[127] for Fe and 6-311+G(d,p) for other atoms was used for single-point energy calculations in solution. Solvation energy corrections were calculated in chlorobenzene (ε=5.6968) solvent with the SMD continuum solvation model[21b] based on the gas-phase optimized geometries. The solvent environment was chosen based on recommendations from previous computational studies of enzymatic reactions to mimic the relative permittivity in enzyme active sites.[128] The C–Br and Fe–Br bond dissociation enthalpies (BDEs) at 298 K were calculated at the same level of theory [(U)B3LYP-D3/LANL2TZ(f)-6-311+G(d,p)/SMD//(U)B3LYP-D3/LANL2DZ/6-31G(d)]. The reported Gibbs free energies and enthalpies in solution include thermal corrections computed at 298 K at the standard concentration (1 mol/L) using GoodVibes.[33] The 3D images of optimized structures were prepared using CYLView.[34]

4.2.2 PNO-LCCSD(T)-F12

The explicitly correlated local coupled cluster method, PNO-LCCSD(T)-F12, was used as references to benchmark DFT methods. The PNO-LCCSD(T)-F12 calculations were performed using Molpro 2020.2.[89] In the PNO-LCCSD(T)-F12 calculations, a mixed basis set of aug-cc-pwCVTZ for Fe, ECP10MDF effective core potential along with aug-cc-pwCVTZ-PP for Br, and VDZ-F12 for other atoms. Def2-TZVPP/JKFIT (Fe), aug-cc-pVTZ/JKFIT (Br), and AVTZ/JKFIT (other atoms) were used as the fitting auxiliary basis to compute the Fock matrix and as the RI basis set. For the density fitting for other calculations of all other 2-electron integrals, the aug-cc-pwCVTZ/MP2FIT (Fe), aug-cc-pVTZ/MP2FIT (Br), and AVDZ/MP2FIT (other atoms) basis sets were used. These basis sets are similar to those used by Werner *et al.* in recent computational studies.[90-91] In the PNO-LCCSD(T)-F12 calculations of the Fe complex, four outer core orbitals (Fe, 3*s*3*p*) were correlated.[90] T1/D1 diagnostic values were calculated in all PNO-LCCSD(T)-F12 calculations in the benchmark study to evaluate the multireference character of these complexes. According to the criteria recommended by Wilson *et al.* for 3d transition metals, T1 values smaller than 0.05 and D1 values smaller than 0.15 would suggest that the single reference PNO-LCCSD(T)-F12 method is adequate to describe the molecular ground state.[92] The computed T1/D1 diagnostic values of most complexes in the present study are smaller than the recommended thresholds (see later for details), indicating that the multireference character of these complexes is not important, and thus the coupled cluster method should predict reliable energetics.

In the DFT and PNO-LCCSD(T)-F12 calculations, porphine was used as a model for the porphyrin ligand and methoxy (OMe) was used as the model for the axial serine ligand. Similar model systems have been used in previous computational studies of heme-containing enzymes.[129] For each Fe complex and transition state, three different spin states were calculated (high-spin,

quintet or sextet; intermediate-spin, triplet or quartet; and low-spin, doublet or singlet). Wavefunction stability tests were carried out with the "stable=opt" keyword to ensure all the open-shell calculations adopted stable wavefunctions. The stability test suggested that the closed-shell singlet wavefunctions of Fe complexes are unstable. All singlet Fe complexes in this study are open-shell singlet without α/β symmetries.

4.2.3 Classical MD Simulations

Classical MD simulations[130] propagate trajectories of atoms and molecules based on solving equations of motion defined in classical (i.e., Newtonian) mechanics. The forces between the particles and their potential energies are calculated force-field based molecular mechanics. Classical MD simulations is widely used to investigate the time evolution of conformations of proteins or other macromolecules.

In this study, we focused on the enzymatic reaction catalyzed by $P450_{ATRCase1}$, an (*R*)-product forming enzyme. The initial geometry of $P450_{ATRCase1}$ used in the modelling was generated by modifying the available X-ray crystal structure of a closely related P450 variant (PDB ID: 4H23).[131] Six mutations (A82T, L181F, I263Q, H266T, T327I, and T438S) were introduced into 4H23 using the mutagenesis tool in PyMOL[132] to prepare $P450_{ATRCase1}$. Classical MD simulations were carried out using the pmemd module of the GPU-accelerated Amber 20 package.[133] Force field parameters for the iron–porphyrin complex were generated using the MCPB.py module[134] with the general Amber force field (gaff).[135] Parameters for substrate **4-1** were generated using the gaff force field, whereas the Amber ff14SB force field[136] was used for standard residues and TIP3P for solvent water molecules. First, three replicas[137] of independent 500 ns MD simulations were performed in the holo state of $P450_{ATRCase1}$ in the absence of substrate **4-1**. Clustering analysis

based on the root-mean-square deviation (RMSD) of backbone was carried out using the cpptraj module[138] to identify the most populated protein conformation in the MD simulations of all three replicas. A representative snapshot of the most visited structure was used for docking calculations with substrate **4-1** using the AutoDock package.[139] Then, MD simulations of substrate-bound $P450_{ATRCase1}$ were performed with and without restraints to study substrate binding poses. In the unrestrained MD simulations, three replicas of 500 ns simulations were performed without including external forces. In the restrained MD simulations, three replicas of 500 ns MD simulations were performed by restraining the Fe–Br distance (2.7–4.0 Å) by applying a harmonic potential of 500 kcal·mol^{-1}·Å^{-2}. These restraints were applied to simulate substrate near attack conformation (NAC) in the inner-sphere bromine atom transfer pathway. This strategy is similar to those applied in previous studies.[122f,140] The restrained distance range used (2.7–4.0 Å) was determined based on the Fe–Br distance observed in a DFT-optimized dative complex using Fe–porphine as a model, which has a Fe–Br distance of 3.80 Å (see Figure S5 of the SI for details). Additional restrained classical MD simulations where both the Fe–Br distance and the hydrogen bond distance between the carbonyl group of the substrate and the amide of the Q263 residue were restrained (the $H^{Q263}\cdots O^{sub}$ distance was restrained in the range of 1–3 Å with a harmonic potential of 200 kcal·mol^{-1}·Å^{-2}). The most representative snapshots from the restrained MD simulations, based on protein backbone RMSD analysis, were used as the initial geometries for QM/MM calculations and QM/MM metadynamics simulations.

4.2.4 QM/MM Calculations of Reaction Energy Profiles

Combined quantum-mechanics/molecular-mechanics (QM/MM) approach[141] is widely used to model reactions in biomolecular reaction in which a QM method is used to treat the crucial

part of an enzyme that affects the reaction mechanism and other electronic processes (e.g., substrates and co-factors in an enzymatic reaction), while a classical force field (MM) is used for the rest. This method enables the modeling of reactive biomolecular systems at a reasonable computational effort with necessary accuracy.

The ONIOM algorithm[142] implemented in Gaussian 16[33] was used in QM/MM calculations to characterize the stationary points (intermediates and transition states). Water molecules and counterions within 5 Å from the enzyme were included in the QM/MM calculations. Several conformers of the substrate were considered for each intermediate and transition state (see Figure S9 of the SI for higher energy conformers). The QM region includes the heme cofactor, the side chain of the Fe-binding serine residue (S400), the substrate, and boundary hydrogen atoms. This includes a total of 77 atoms in the QM region. For the QM region, the dispersion-corrected B3LYP-D3[126]/6-31G(d)–LANL2DZ(Fe) level of theory was used in geometry optimization and vibrational frequency calculations, and the B3LYP-D3/6-311+G(d,p)–LANL2TZ(f)(Fe) level of theory was used in single-point energy calculations. This level of theory has been shown to provide good agreement with PNO-LCCSD(T)-F12 benchmark results.[10] For the MM region, the same force field parameters from the classical MD simulations discussed above were used. The quadratic coupled algorithm[143] and the mechanical embedding scheme were used in geometry optimization. Residues greater than 6 Å away from the QM region were kept fixed during geometry optimization. Single-point energy calculations were performed with the electronic embedding scheme, which better describes electrostatic interactions between QM and MM regions.[144] Open-shell singlet, triplet, quintet, and septet spin[145] states for each structure were considered. Wavefunction stability of all structures was confirmed by using the "stable=opt" keyword.

4.2.5 QM/MM Metadynamics Simulations

QM/MM Metadynamics Simulations is an enhanced sampling method that combine metadynamics and QM/MM techaniques. This technique has been successfully applied to study chemical reactions that take place in biomolecular systems.

All QM/MM Born Oppenheimer MD metadynamics simulations were performed with the CP2K 7.1 package, combining the QM program QUICKSTEP[38] and the MM driver FIST. In this program, a real-space multigrid technique is used to compute the electrostatic coupling between the QM and MM regions.[146] The heme cofactor, the side chains of F181, Q263 (two key active site residues identified by protein engineering), and the Fe-binding S400, the substrate, and boundary hydrogen atoms were included in the QM region. This leads to 137 atoms in the QM region. The remaining part of the system was modelled at the MM level using the same parameters as in the classical MD simulations. The QM region was treated at the DFT (BLYP-D3) level,[29b, 147] employing the Gaussian and plane waves method (GPW) that combines Gaussian-type basis functions and plane-waves as an auxiliary basis. The DZVP basis set[40] and Goedecker-Teter-Hutter pseudopotentials[41] were employed. The auxiliary plane-wave basis set was expanded up to a 280 Ry cutoff. Trajectories starting from different initial geometries, obtained from snapshots of the restrained classical MD simulations, were simulated in the QM/MM metadynamics calculations. All QM/MM metadynamics simulations were performed in the NVT (constant number of atoms, volume, and temperature) ensemble using an integration time step of 0.5 fs. First, the system was equilibrated without any restraint for 2.0 ps. Then, the metadynamics method[17] was used to compute the free energy profiles. In the simulations of the radical cyclization pathways, one collective variable was defined as the distance of the forming C–C bond between the radical center and the alkenyl carbon of the substate. In the simulations to study the flexibility

of the *N*-allyl group in the radical intermediate, two collective variables were defined as dihedral angles about the allylic C–C (ϕ) and N–C(allyl) (θ) bonds. Repulsive Gaussian-shaped potential hills with a height of 0.3 kcal/mol and a width of 0.1 bohr for distance and 0.1 rad for dihedral angle were added to the potential every 20 molecular dynamics steps.

4.3 Results and Discussion

4.3.1 Reaction energy profile of the model system for biocatalytic atom transfer radical addition

At the outset of the computational study, we performed DFT calculations using a model system[10,148] for the axial serine-ligated P450 catalyst to elucidate the reaction mechanism and the origin of the biocatalyst's activity calculations (Figure 4-4). DFT calculations showed that the quintet Fe(II) catalyst (**4-^{5}3**) is 13.5 and 20.1 kcal/mol more stable than the triplet (**4-^{3}3**) and singlet (**4-^{1}3**), respectively. Similarly, the high-spin sextet ferric bromide intermediate (**4-^{6}4**) is 5.1 and 2.8 kcal/mol more stable than the quartet (**4-^{4}4**) and doublet (**4-^{2}4**), respectively. Thus, in this newly developed biocatalytic ATRC process, the Fe porphyrin catalyst remains high-spin throughout the catalytic cycle. This contrasts with the previously studied native oxene transfer[115b] and analogous nitrene transfer[148] chemistry of P450 enzymes, wherein spin crossover is involved. With the model system, the radical initiation step (**4-TS1**) has a relatively low activation barrier ($\Delta G^{\ddagger}$) of 17.7 kcal/mol. Considering that the enzyme environment may further facilitate this process by promoting substrate binding to form complex **4-5**, this Fe-catalyzed radical initiation is expected to be kinetically facile. The electron-rich nature of the Fe center allows for the facile

single electron reduction of the substrate, as evidenced by the substantial electron transfer (0.44 e^-) from **4-3** to **4-1** in **4-TS1**. After the selective 5-*exo*-trig cyclization (**4-TS2-*exo***) to form the primary carbon radical **4-7**, the bromine rebound step (**4-TS3**) is highly exergonic with a low activation barrier of 13.1 kcal/mol. The fast trapping of this newly formed carbon radical via bromine atom transfer renders the C–C bond formation step irreversible and enables kinetic control of reaction stereochemistry. The bromine rebound reactivity is promoted by the conversion of a weaker Fe–Br bond in the ferric bromide species (**4-4**) to a stronger primary C(sp^3)–Br bond in **4-1**. Therefore, the unique ability of the Fe porphyrin system to promote both radical initiation and bromine rebound steps makes it an effective ATRC biocatalyst.

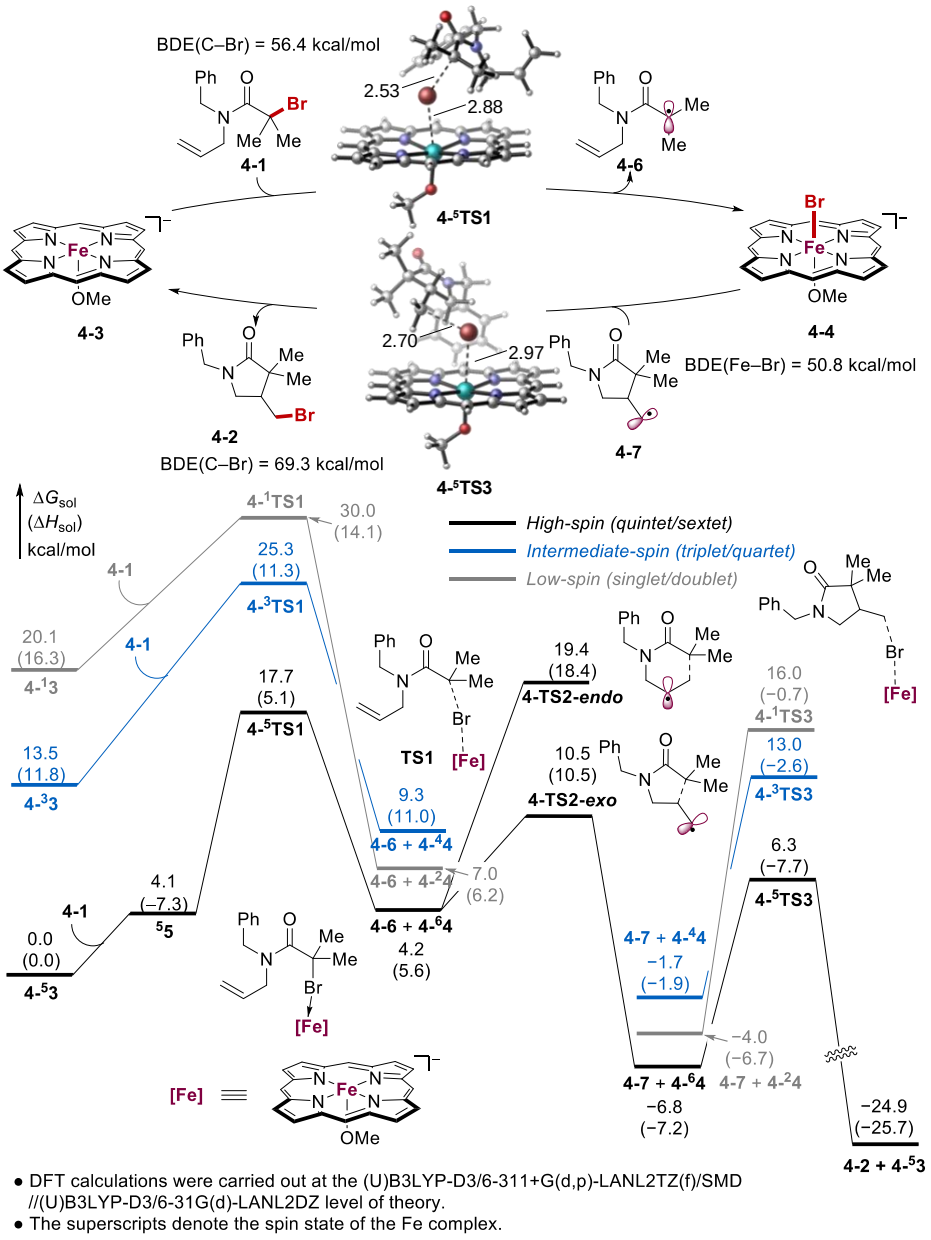

Figure 4-4 Reaction energy profile of the current biocatalytic atom transfer radical addition using a model system for the axial serine-ligated Fe-porphyrin catalyst.

4.3.2 Benchmark of DFT methods for spin-state energies of iron-porphyrin complexes

The performance of DFT methods for spin-state energies of iron complexes, including model iron-heme complexes, has been extensively studied.[149] Here, we performed benchmark

calculations of the Fe(II) complex **4-3** in singlet (**4-^{1}3**), triplet (**4-^{3}3**), and quintet (**4-^{5}3**) spin states and the Fe(III)–Br complex **4-4** in doublet (**4-^{2}4**), quartet (**4-^{4}4**), and sextet (**4-^{6}4**) spin states to identify suitable DFT methods for energetics of the iron-porphyrin complexes in the present system (Table 4-1). To obtain accurate single-point energies as references, we performed the explicitly correlated local coupled-cluster calculations (PNO-LCCSD(T)-F12) using the B3LYP-D3-optimized geometries. All benchmark calculations were performed in the gas phase.

PNO-LCCSD(T)-F12 calculations predicted that the high-spin state (quintet) of **4-3** is highly favorable. The quintet Fe(II) catalyst **4-^{5}3** is 22.1 kcal/mol more stable than the triplet **4-^{3}3** and 23.5 kcal/mol more stable than its singlet **4-^{1}3**. The Fe(III)–Br complex prefers the low-spin doublet state in the gas phase, although the sextet (**4-^{6}4**) is only 3.0 kcal/mol higher in energy than the doublet (**4-^{2}4**). The quartet (**4-^{4}4**) is 12.3 kcal/mol less stable than the sextet **4-^{6}4**. All DFT methods tested correctly predicted the high-spin quintet state of **4-3** is the most stable. However, only (U)B3LYP-D3, (U)OLYP[150], and (U)MN15[151] correctly predicted the lowest-energy spin state for **4-4**. (U)OPBE[29a] and (U)ωB97X-D[86] predicted the high-spin sextet state is slightly more stable than the doublet. (U)M06[152] significantly overestimated the stability of the high-spin sextet state of **4-4**. We chose (U)B3LYP-D3 in the following DFT calculations because it predicted the correct spin states for both **4-3** and **4-4** and provided the best agreement with the PNO-LCCSD(T)-F12 spin-state energies (*i.e.* with the smallest mean absolute error, MAE).

Table 4-1 Benchmark of DFT methods.

	PNO-CCSD(T)-F12	**B3LYP-D3**	OLYP	OPBE	ωB97X-D	M06	MN15
ΔE_{LH}(**4-3**)	−23.5	**−16.0**	−14.5	−15.8	−19.9	−38.2	−16.9
ΔE_{IH}(**4-3**)	−22.1	**−10.7**	−7.9	−7.9	−16.6	−16.3	−4.2
ΔE_{LH}(**4-4**)	3.0	**1.4**	0.2	−0.7	−0.1	−24.6	10.2
ΔE_{IH}(**4-4**)	−12.3	**−6.2**	−5.9	−7.3	−7.5	−16.6	2.8
MAE($\Delta\Delta E$)		**6.7**	8.1	7.7	4.3	13.1	11.7

[a]All energies are in kcal/mol. For **4-3**, $\Delta E_{LH} = E_{quintet} - E_{singlet}$, $\Delta E_{IH} = E_{quintet} - E_{triplet}$. For **4-4**, $\Delta E_{LH} = E_{sextet} - E_{doublet}$, $\Delta E_{IH} = E_{sextet} - E_{quartet}$, $\Delta\Delta E = \Delta E_{DFT} - \Delta E_{PNO\text{-}CCSD(T)\text{-}F12}$. Geometries were optimized at the (U)B3LYP/6-31G(d)–LANL2DZ level of theory in gas phase at the corresponding spin state.

The T1/D1 diagnostic values of all Fe complexes are below the threshold values (T1 < 0.05, D1 < 0.15), except for **4-^{2}4** where the D1 value (0.183) is slightly higher than the threshold (Table 4-2). The small T1/D1 diagnostic values of these iron complexes indicate their multireference character is not important, and thus the PNO-LCCSD(T)-F12 results are expected to be reliable as the energy references to benchmark DFT methods.

Table 4-2 Diagnostics of multireference character.

Diagnostics	**4-^{1}3**	**4-^{3}3**	**4-^{5}3**	**4-^{2}4**	**4-^{4}4**	**4-^{6}4**
T1	0.022	0.019	0.015	0.025	0.023	0.020
D1	0.137	0.099	0.056	0.183	0.145	0.114

4.3.3 Substrate Binding Modes and Unexpected Hydrogen Bonding Interaction with Key Residue Q263

To explore the substrate binding modes within the enzyme active site, we performed classical MD simulations of the enzyme–substrate complex. After docking substrate **4-1** into the

active site of $P450_{ATRCase1}$, we performed three replicas of 500 ns MD simulation without any restraint (unrestrained MD). We also performed another three replicas of 500 ns MD simulations by restraining the Fe–Br distance within 2.7–4.0 Å to mimic the near attack conformation (NAC)[122f] for bromine atom abstraction (restrained MD).

Both MD simulations revealed the existence of two dominant interaction modes with Q263 (Figure 4-4a), where the carbonyl group of the substrate forms a hydrogen bond with the NH_2 group of the side chain of Q263 (interaction mode **A**) or with a water molecule bridging Q263 and the substrate (interaction mode **B**). The unrestrained MD simulations describe that in most of the simulation time (63.9%), the N–H···O distance between the side chain NH_2 group in Q263 and the amide carbonyl oxygen of **4-1** is shorter than 3 Å. In the restrained MD simulations, this direct Q263–substrate hydrogen bond was observed in a smaller percentage of the simulation time (21.2 %), because the distance restriction between Fe and Br induces less favorable spatial arrangement for the hydrogen bond. Nonetheless, most snapshots maintain a relatively short distance between Q263 and the substrate (< 5 Å), with either a direct hydrogen bond with Q263's NH_2 group or water-bridged hydrogen bond between these two groups (Figure 4-5). These MD simulations suggest that hydrogen bonding interactions with Q263 are important for substrate binding and may be involved in subsequent steps of the catalytic cycle. This will be examined using QM/MM calculations in the next section.

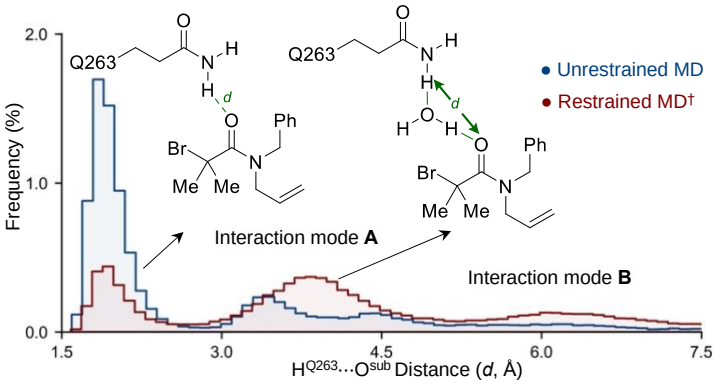

	Interaction mode A	Interaction mode B	No interaction with Q263
$H^{Q263}\cdots O^{sub}$ distance	< 3 Å	3–5 Å	> 5 Å
% in unrestrained MD trajectories	63.9 %	24.3 %	11.8 %
% in restrained MD trajectories†	21.3 %	42.7 %	36.0 %

† Fe–Br distance is restrained to 2.7–4.0 Å to mimic the near attack conformation (NAC).

Figure 4-5 Hydrogen bonding interactions between Q263 side chain and the substrate

Both unrestrained and restrained MD simulations describe a preferred binding pose of the substrate in which the *N*-benzyl group of **4-1** is placed in proximity to L437, establishing hydrophobic C–H···π interactions (Figure 4-6). Due to this stabilizing interaction, the *s-cis* conformer of the amide is strongly favored within the active site, as seen in greater than 93% of the simulation time. In the favored *s-cis* conformer, the *N*-allyl group is *cis* to the bromoalkyl group, a conformation required in the subsequent radical cyclization step. In the absence of enzyme scaffold, rotation along the amide bond led to less efficient ATRC of *N*-allyl α-haloamides,[153] demonstrating the templating effect of the protein scaffold in facilitating radical catalysis. Overall, the orientation of **4-1** in the active site remains relatively stable throughout the MD trajectories due to the hydrogen bonding interactions with the amide carbonyl and the C–H···π interactions with the *N*-benzyl group. These interactions not only promote substrate binding but also stabilize the *s-cis* conformer of the amide poised to undergo radical cyclization.

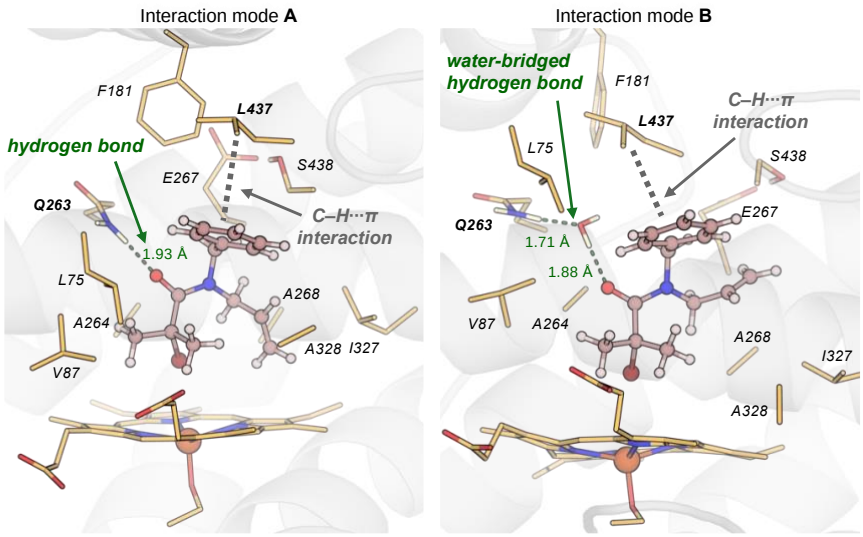

Figure 4-6 Representative MD snapshots of preferred binding pose of substrate 4-1 in P450ATRCase1 active site

MM-GBSA substrate–residue pair interaction calculations[154] were performed to analyze active site interactions with the substrate (Figure 4-7). These calculations revealed that Q263 and L437 are among residues establishing the most stabilizing interactions with the substrate, further highlighting their importance for the substrate binding via hydrogen bonding and C−H···π interactions with these residues, respectively.

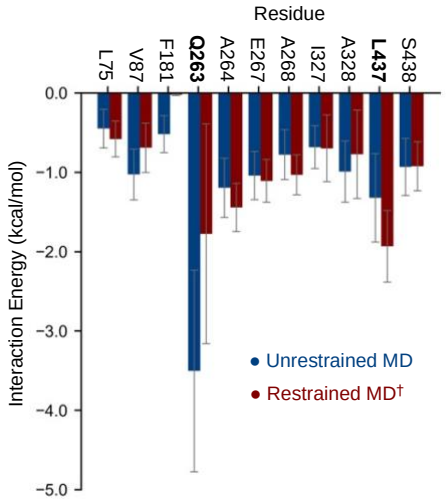

Figure 4-7 MM-GBSA substrate–residue pair interactions.

4.3.4 Reaction Energy Profiles from QM/MM Calculations and the Roles of Q263 on Reactivity of Substrate Activation

We next used QM/MM methods to compute the free energy profile of this biocatalytic ATRC process. QM/MM calculations were performed starting from the preferred substrate binding mode characterized from MD simulations, and considering interaction mode **A** with Q263 residue (Figure 4-8), where the amide side chain of Q263 engages the substrate in hydrogen bonding interactions. Open-shell singlet, triplet, quintet, and septet spin states of each intermediate and transition state structure were optimized using QM/MM. Gibbs free energy profiles involving the two most favorable spin states, quintet and septet, affording the major enantiomeric product **4-(*R*)-2** via radical addition to the (*Si*)-face of the alkene (**4-TS5-(*Si*)**) are shown in Figure 3. The quintet spin state was found to be the most favorable spin state for the enzyme–substrate and enzyme–product complexes and bromine atom abstraction and bromine atom rebound transition states (**4-TS4** and **4- (*R*)-TS6**), whereas the septet spin state was found to be the most stable in α-carbonyl radical **4-9**, radical cyclization transition state **4-TS5-(*Si*)**, and the succeeding cyclized primary radical **4- (*R*)-10**.

The QM/MM-computed energy profiles revealed several key mechanistic features critical for the reactivity and enantioselectivity of this enzymatic ATRC. First, the Fe(II)/Fe(III) metalloredox processes (**4-TS4** and **4- (*R*)-TS6**) are both kinetically facile. Although the radical initiation via bromine atom abstraction (**4-TS4**) is endergonic by 6.4 kcal/mol, it requires a relatively low activation free energy of 17.3 kcal/mol. The endergonicity of this step is comparable to the bromine atom abstraction step in Cu-catalyzed atom transfer radical polymerization (Cu-ATRP), which has an equilibrium constant of $K_{ATRP} = 10^{-9} \sim 10^{-4}$ in most common Cu-ATRP systems.[155] The relatively high HOMO energy of the heme cofactor (−3.3 eV, compared with −5.6

eV for $Cu(TPMA)^+$, a representative Cu-ATRP catalyst)[156] suggests that this Fe-mediated bromine atom abstraction is kinetically promoted due to effective metal-to-substrate charge transfer in the bromine atom abstraction transition state.[157] Because bromine atom abstraction is the rate-determining step in the QM/MM-computed catalytic cycle, a low kinetic barrier is essential for the reactivity of the ATRC. On the other hand, the exergonicity of the bromine atom rebound step enables rapid trapping of the enantioenriched cyclized primary radical intermediate **4-(*R*)-10** via **4-(*R*)-TS6**. Because the Gibbs free energy of **4-(*R*)-TS6** is lower than that of **4-TS5-(*Si*)**, the radical cyclization (**4-TS5-(*Si*)**) is irreversible, and thus determines the enantioselectivity.

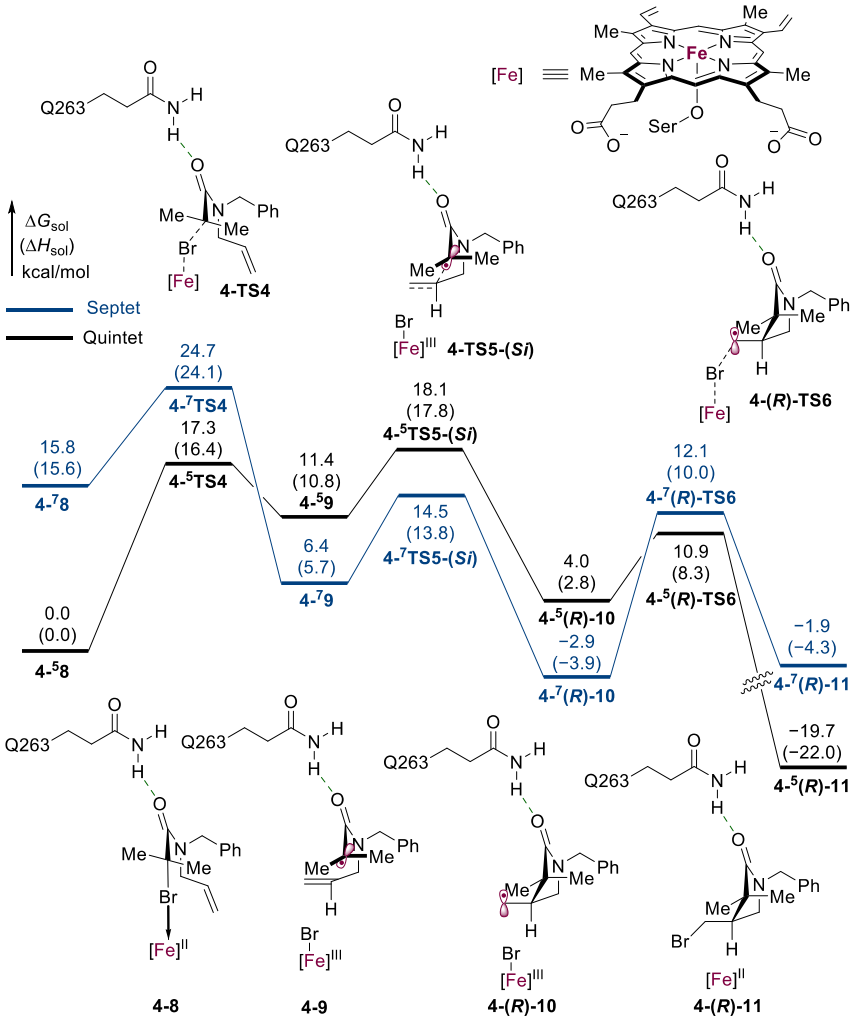

Figure 4-8 Computed Gibbs free energy profiles of the P450$_{ATRCase1}$-catalyzed ATRC from QM/MM calculations.

The reactivity of bromine atom abstraction is promoted by hydrogen bonding interaction between the amide side chain in Q263 and the carbonyl group of substrate **4-1**. This hydrogen bond persists throughout catalysis among all the QM/MM-optimized intermediate and transition state structures (Figure 4-9, and Figure 4-10). Furthermore, our QM/MM calculations showed slightly shorter N–H···O distances in bromine atom abstraction transition state **4-^{5}TS4** and α-carbonyl radical intermediate **4-^{7}9** compared to that in the enzyme–substrate complex **4-^{5}8**. These results indicate that this hydrogen bond not only promotes the substrate binding but also more

substantially stabilizes bromine atom abstraction TS and the radical being formed, promoting this rate-determining substrate activation step. The rate acceleration effect of Q263 is further evidenced by the computed bromine atom abstraction transition state from a MD snapshot without the hydrogen bond with Q263 (**4-TS4'**, Figure 4-9). The absence of hydrogen bonding with the Q263 side chain results in a bromine atom abstraction barrier of 1.9 kcal/mol higher than that involving Q263 via **4-TS4**.

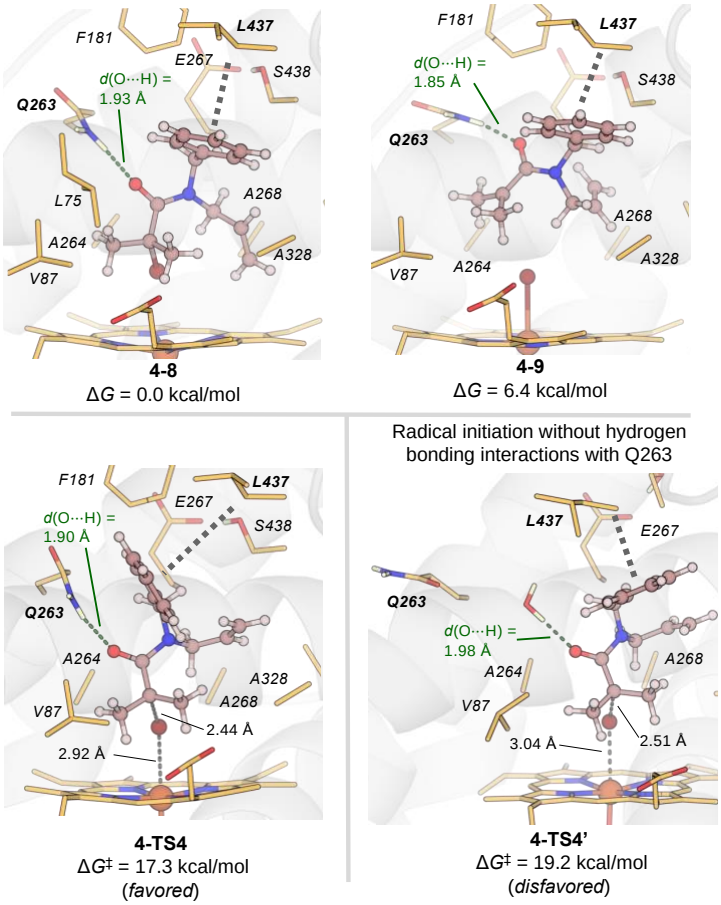

Figure 4-9 QM/MM-optimized structures of intermediates and transition state in the rate-determining radical initiation step and less favorable radical initiation transition state without hydrogen bonding interaction with Q263.

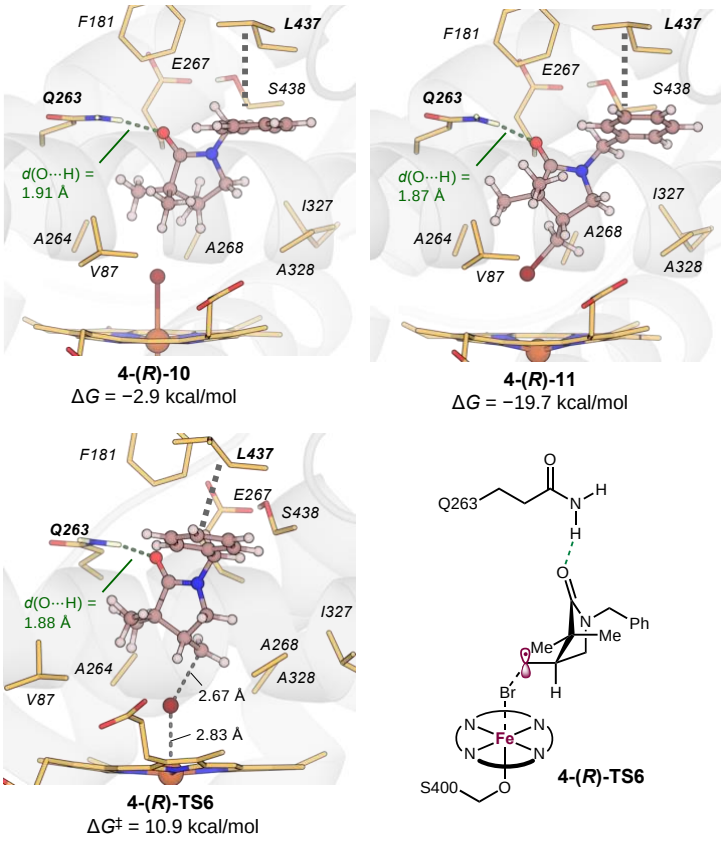

Figure 4-10 QM/MM-optimized structures of intermediates and transition state in the bromine atom rebound step.

These results show that the glutamine residue is an activating hydrogen-bond donor and can accelerate the rate-determining bromine atom abstraction step. Further calculations using truncated model systems showed that this hydrogen bonding interaction lowers the energy of the LUMO orbital of the α-bromoamide moiety, thereby weakening the α-C–Br bond (see Figure 4-11).

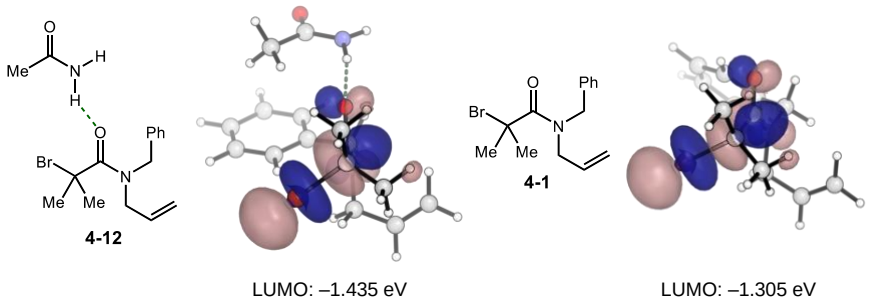

Figure 4-11 Effect of hydrogen bonding interaction on LUMO energies.

The I263Q mutation represents one of the most important beneficial mutations in our previously reported directed evolution effort, as it led to dramatically enhanced activity and enantioselectivity of P450$_{ATRCase1}$. Compared to its parent, the I263Q mutant increased the total turnover number (TTN) from 1810 to 5370 and enantiomeric ratio (e.r.) from 67:33 to 89:11.[3] Despite these results, the role of this I263Q mutation was not known at the time P450$_{ATRCase1}$ was engineered. The computational results disclosed herein rationalized the role of Q263 on the experimentally observed reactivity. The higher e.r. with the I263Q variant suggests that this residue also plays a key role in the enantioselectivity-determining step. This effect is discussed in the next section.

4.3.5 Origin of Enantioselectivity and the Cooperative Effects of Q263 and Heme Cofactor on Enantioinduction

In order to understand the origin of enantioselectivity, we performed QM/MM calculations to study the enantioselectivity-determining radical cyclization transition states (Figure 4-12). The transition state of radical addition to the (*Si*)-face of the alkenyl group **4-TS5-(*Si*)** leading to the experimentally observed major enantiomeric product **4-(*R*)-2** requires an activation free energy of

8.1 kcal/mol with respect to the α-carbonyl radical **4-9**. **4-TS5-(*Re*)** leading to the opposite enantiomeric product, **4-(*S*)-2**, is 2.5 kcal/mol higher in energy.

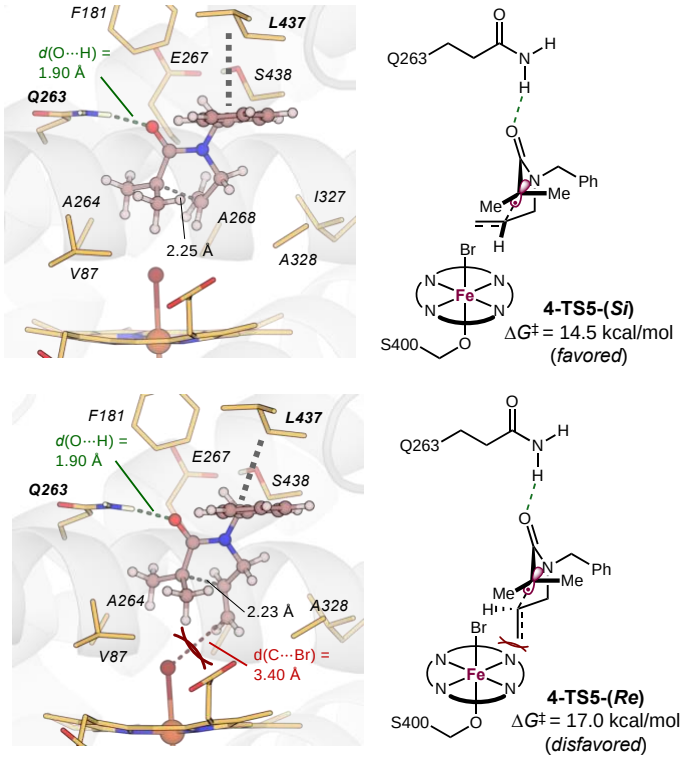

Figure 4-12 QM/MM-optimized structures of enantioselectivity-determining radical cyclization transition states.

Hydrogen bonding interactions between Q263 and the carbonyl group of substrate **4-1** and C–H···π interactions between L437 and the *N*-benzyl group on **4-1** are observed in both transition states **4-TS5-(*Si*)** and **4-TS5-(*Re*)** (Figure 4-12). These interactions restrained the positioning of the substrate in the active site, placing the α-carbonyl radical center relatively close to the heme cofactor. When approaching the α-carbonyl radical during the radical cyclization, the alkenyl group is placed closer to the heme cofactor. In the favored radical cyclization transition state **4-TS5-(*Si*)**, the alkenyl group points away from the heme, whereas in the disfavored transition state **4-TS5-(*Re*)**, the alkenyl group points towards the heme, leading to unfavorable steric repulsions.

This unfavorable steric effect is evidenced by the short distance between the terminal olefinic carbon and the bromine atom on heme (3.40 Å) in **4-TS5-(*Re*)**.

Next, we performed QM/MM metadynamics simulations to study the structural features along the radical cyclization reaction coordinate. The radical cyclization transition states characterized by QM/MM metadynamics (Figure 4-13) are structurally similar to those obtained from QM/MM geometry optimizations (Figure 4-12). The Gibbs free energies of activation estimated from the QM/MM metadynamics trajectories leading to products **4-(*R*)-2** and **4-(*S*)-2** are 8.1 and 13.3 kcal/mol with respect to the α-carbonyl radical intermediate, respectively. This is in line with QM/MM geometry optimizations indicating that formation of **4-(*R*)-2** is more favorable due to greater steric repulsions between the terminal alkenyl group and heme cofactor.

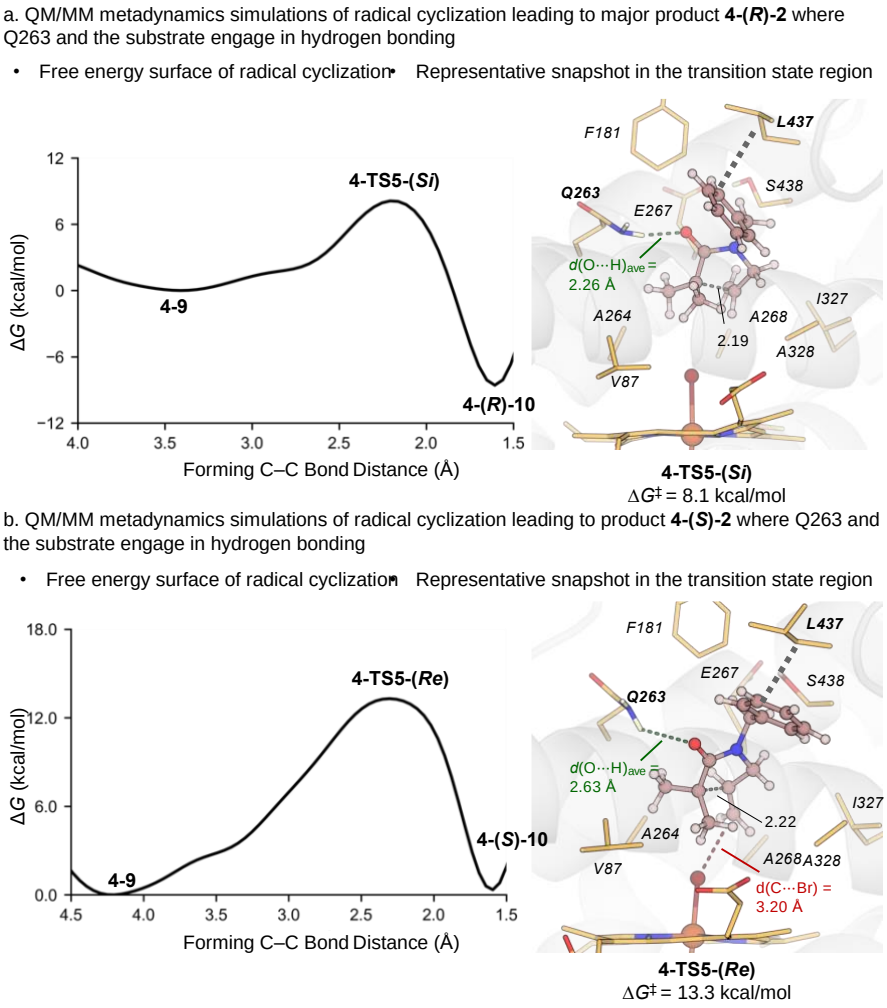

Figure 4-13 QM/MM metadynamics simulations of radical cyclization pathways involving a hydrogen bond between Q263 side chain and the carbonyl group on the substrate.

The $H^{Q263}\cdots O^{sub}$ distances of the hydrogen bond between Q263 and the carbonyl group on substrate **4-1** along these QM/MM metadynamics trajectories are shown in Figure 4-14.[158] The hydrogen bond along the radical cyclization pathway to form **4-(*R*)-2** via **4-TS5-(*Si*)** remains relatively strong with average $H^{Q263}\cdots O^{sub}$ distance smaller than 2.5 Å. On the other hand, the hydrogen bonding interaction with Q263 is weaker in the region near the disfavored transition state **4-TS5-(*Re*)**, evidenced by slightly longer $H^{Q263}\cdots O^{sub}$ distances explored along the radical cyclization pathway. The steric repulsions with heme lead to unfavorable distortion of **4-TS5-(*Re*)**,

weakening the hydrogen-bond with Q263, a key enzyme–substrate interaction. Overall, both the QM/MM and the metadynamics simulations highlighted the cooperative effects of the Q263 residue, hydrophobic active site residues, such as L437, and the heme cofactor in anchoring the substrate and exerting steric interactions to affect the enantioinduction in radical cyclization transition states.

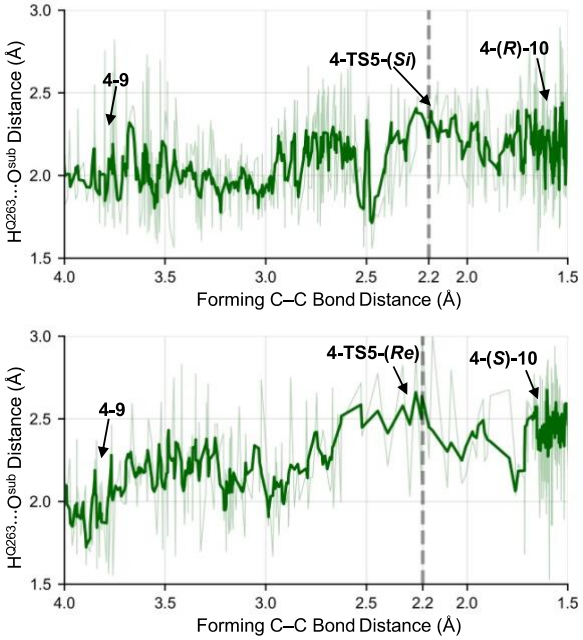

Figure 4-14 Q263 hydrogen bonding interactions along the radical cyclization pathways from QM/MM metadynamics simulations.

4.3.6 Classical MD and QM/MM Metadynamics Simulations on the Conformational Flexibility of the *N*-Allyl Group in Ground State Complexes

We performed molecular dynamics simulations using both classical MD and QM/MM metadynamics to explore the conformational flexibility of the *N*-allyl group in the enzyme–substrate complex **4-8** and the α-carbonyl radical intermediate **4-9** (Figures 4-15 and 4-16). We surmised that these simulations, in conjunction with the transition state modeling discussed above,

would reveal which of the two enantioinduction scenarios shown in Figure 4-14 is operative in this enzymatic ATRC. In particular, these ground-state simulations could reveal whether the allyl group rotation is restricted prior to the radical cyclization transition state, therefore offering a binding-based enantioinduction model for π-facial discrimination.

The conformations of the *N*-allyl group in the enzyme–substrate complex **4-8** observed along the unrestrained and restrained classical MD simulations are described in Figure 6a. These MD simulations showed four clusters of conformers (**4-8a-4-8d**) with almost equal distributions, resulting from rotations about the N–C(allyl) (θ) and the allylic C–C (ϕ) bond. In the centroids of each cluster, the allyl group and the carbonyl are anticlinal (θ is within 90~150º or −90~−150º) rather than having the synperiplanar conformation (θ = 30~−30º) in the radical cyclization transition states. The lack of sterically bulky residues around the *N*-allyl group allows for the facile conformational change in the enzyme–substrate complex. Due to this conformational flexibility of the *N*-allyl group, there is no clear preference for the (*Re*)- or the (*Si*)-face of the C=C double bond to be exposed to the α-bromoamide moiety.

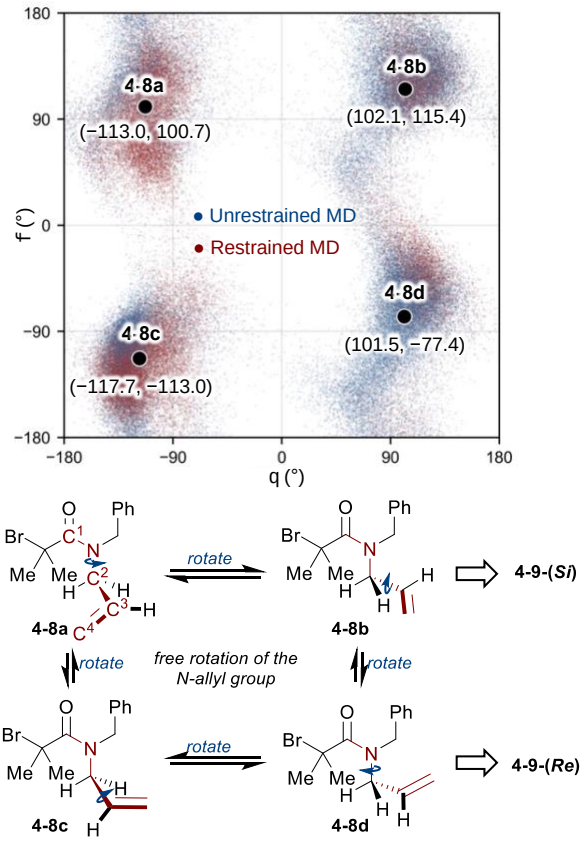

Figure 4-15 Conformational change of the *N*-allyl group in enzyme–substrate complex 4-8 and α-carbonyl radical intermediate 4-9 from classical MD.

Next, we performed QM/MM metadynamics simulations on the α-carbonyl radical intermediate **4-9** to investigate the rate of *N*-allyl group rotation once the radical is formed. In these simulations, we used the dihedral angles about the allylic C–C (ϕ) and N–C(allyl) (θ) bonds as the collective variables. Similar to conformers **4-8a-4-8d**, the allyl group and the carbonyl are anti- or synclinal in all of the low-energy conformers of **4-9** (Figure 4-15). These conformers isomerize to synperiplanar conformation, such as in **4-9'-(*Si*)** and **4-9'-(*Re*)**, via rotation about the N–C(allyl) (θ) bond prior to the radical cyclization transition state. Although **4-9'-(*Si*)** and **4-9'-(*Re*)** are not minima on the free energy surface, the conformational change to these synperiplanar structures is kinetically facile. The QM/MM metadynamics calculations indicate conformer **4-9-(*Si*)**, which leads to the favored (*Si*)-face radical cyclization after N–C(allyl) (θ) bond rotation and radical

addition, is 3.6 kcal/mol more stable than conformer **4-9-(*Re*)**, which leads to the less favorable radical cyclization with the (*Re*)-face of the olefin. Here, **4-9-(*Re*)** is destabilized by steric repulsions between the terminal alkenyl group and heme cofactor, similar to the steric effect that destabilizes **4-TS5-(*Re*)**. The low barrier to the interconversion between **4-9-(*Si*)** and **4-9-(*Re*)** via allylic C–C bond (ϕ) rotation **(**$\Delta G^{\ddagger}_{rot}$ = 5.2 kcal/mol**)** indicates that the *N*-allyl conformational change is much faster than the radical cyclization ($\Delta G^{\ddagger}$ = 8.1 kcal/mol via **4-TS5-(*Si*)**).

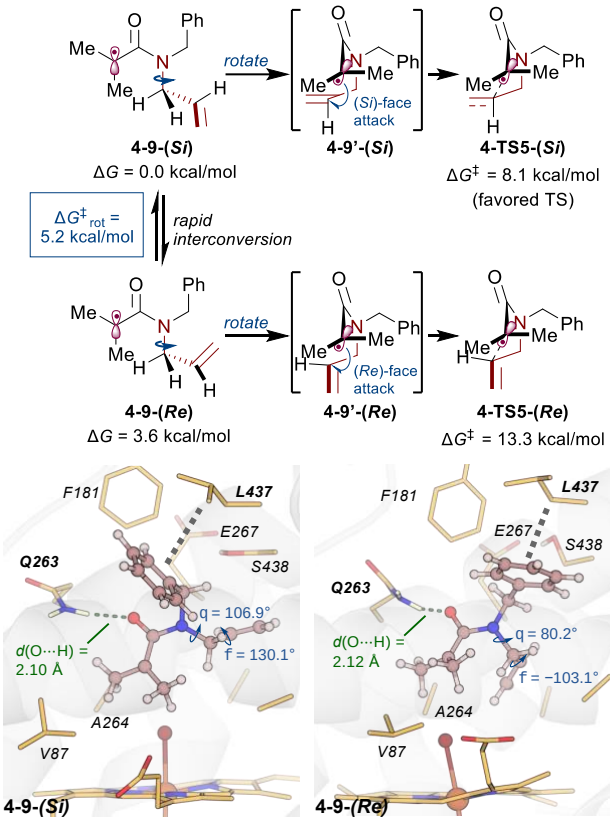

Figure 4-16 QM/MM metadynamics simulations of rotations of *N*-allyl groups in the α-carbonyl radical intermediate using allylic C–C (ϕ) and N–C(allyl) (θ) bonds as the collective variables.

The interconversion barrier between **4-9-(*Si*)** and **4-9-(*Re*)** is comparable to that of *N*-allylamide in the absence of the enzyme (Figure 4-17), indicating minimal interactions between the allyl group and active site residues in the α-carbonyl radical intermediate.

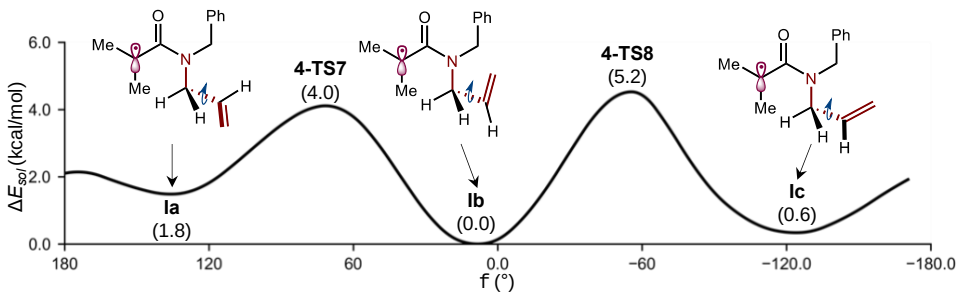

Figure 4-17 DFT calculated relative energies along the allylic C–C (*ϕ*) rotational coordinate of the *N*-allyl group in the α-carbonyl radical intermediate in the absence of the enzyme environment.

Overall, these simulations indicated a highly flexible *N*-allyl group in both the enzyme-bound substrate and the enzyme-bound α-carbonyl radical intermediate. Due to the rapid conformational interconversion of the *N*-allyl group in these ground state complexes, the enantioselectivity of this new-to-nature enzymatic ATRC process is solely determined by the radical cyclization transition state and not by the initial substrate conformation.

4.3.7 Experimental Investigations on the Importance of Residue 263 on Reactivity and Enantioselectivity

In light of the key role of residue Q263 uncovered by the computational studies, our collaborator from the Yang group generated $P450_{ATRCase1}$ Q263X mutants (X = R, K, N, S, A, I, and E) by site-directed mutagenesis and examined their catalytic activity and enantioselectivity in the radical cyclization of **4-1** (Table 4-3). In this study, other potential hydrogen bond donors, including arginine, lysine, asparagine, and serine, were evaluated in addition to residues lacking a hydrogen bond donor, including alanine, isoleucine, and glutamate.

Consistent with our computational insights, when Q263 was replaced by an appropriate alternative hydrogen bond donor residue, similar enzyme activity and enantioselectivity were

observed. The second-best residue at 263 was found to be arginine (R263, Table 1, entry 2), which bears a guanidine functional group that can potentially serve as a hydrogen bond donor. With this Q263R mutant, yield, total turnover number (TTN), and enantioselectivity very similar to the Q263 parent were observed. The Q263K mutant provided slightly further reduced enantioselectivity (entry 3). Interestingly, a further drop in e.r. was observed when this glutamine was replaced by an asparagine (entry 4), highlighting the importance of the tethering unit length for this hydrogen bond donor to engage the amide substrate. A263 lacking a hydrogen bond donor side chain and S263 with a much shorter hydrogen bond donor hydroxymethyl side chain provided greatly reduced enzyme activity and enantioselectivity (entries 5–6). Similar to the Q263A mutant, reverting this Q263 to I263 in native P450BM3 led to inferior enzyme performance (entry 7). The E263 mutant bearing a presumably deprotonated glutamate at residue 263 also provided low activity and enantioselectivity (entry 8). Together, these studies provided further evidence to support the essential role of residue Q263 of $P450_{ATRCase1}$, underscoring the importance of a hydrogen bond donor residue to both the enzyme activity and enantioselectivity.

Table 4-3 Experimental validation. Experimental studies were performed by Heyu Chen and Wenzhen Fu at the University of California, Santa Barbara.

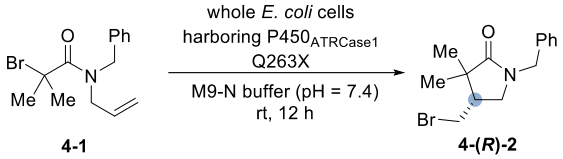

entry	mutation of $P450_{ATRCase1}$	yield (%)[a]	TTN	e.r.[a]
1	None	89 ± 2	4400 ± 100	96:4
2	Q263R	82 ± 3	3700 ± 100	95:5
3	Q263K	76 ± 2	3730 ± 90	91:9
4	Q263N	75 ± 0	4340 ± 20	84:16
5	Q263S	36 ± 1	2310 ± 50	78:22
6	Q263A	37 ± 1	2490 ± 70	79:21.5
7	Q263I	52 ± 8	1300 ± 200	87:13
8	Q263E	25 ± 0	1300 ± 10	66:34

[a] Yields and e.r.'s were determined by HPLC analysis. Reactions were carried out using whole *E. coli* cells harboring $P450_{ATRCase1}$ mutants.

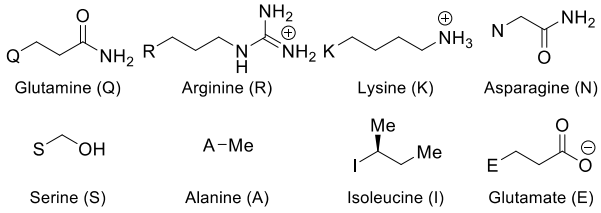

4.4 Conclusion

Using a combined computational and experimental approach, we elucidated the mechanism and the origin of enantioselectivity of our recently developed biocatalytic atom transfer radical cyclization using a laboratory-evolved P450 cyclase. QM/MM and classical MD

simulations showed that the substrate binds to the enzyme active site, establishing a stabilizing hydrogen-bonding interaction with Q263 and C–H···π interactions with L437. While these stabilizing interactions are maintained throughout the catalytic process, leading to a relatively rigid positioning of the substrate carbonyl within the enzyme active site, the *N*-allyl group of the substrate is highly flexible and undergoes rapid conformational change in enzyme-bound forms. The facile conformational change of the *N*-allyl group in ground state complexes makes the enantioselectivity entirely determined in the radical cyclization transition state. Notwithstanding the lack of conformational preference at the stage of various ground-state intermediates, high levels of enantioselectivity are achieved in the radical cyclization transition state where the olefin approaches the radical center, leading to further accentuated steric interactions with the heme cofactor. This study revealed the critical role of Q263 in promoting both reactivity and enantioselectivity, as it stabilizes substrate binding, promotes the rate-determining bromine atom abstraction, and controls the substrate orientation in the enantioselectivity-determining radical cyclization step. The multiple functions of Q263 were further corroborated by experiments evaluating the activity and enantioselectivity of enzyme variants generated by site-directed mutagenesis. Together, this study highlights the synergy between computations and experiments in providing to insights into the mechanism of enantioinduction in radical-mediated enzymatic reactions. We expect that these insights will guide the further engineering of stereoselective ATRCases and development of other asymmetric new-to-nature radical-mediated enzymatic reactions.

Appendix A List of Publications

1. Fu, Y.; Chen, H.; Fu, W.; Garcia-Borràs, M.; Yang, Y.; Liu, P. Engineered P450 Atom-Transfer Radical Cyclases Are Bifunctional Biocatalysts: Reaction Mechanism and Origin of Enantioselectivity. *J. Am. Chem. Soc.* **2022**, *144*, 13344–13355.
2. Fu, Y.; Zerull, E.; Schomaker, J.; Liu, P. Origins of Catalyst-Controlled Selectivity in the Ag-Catalyzed Regiodivergent C−H Amination. *J. Am. Chem. Soc.* **2022**, *144*, 2735–2746.
3. Xu, S.; Pozo, J. del; Romiti, F.; Fu, Y.; Mai, B. K.; Morrison, R. J.; Lee, K.; Hu, S.; Koh, M. J.; Lee, J.; Li, X.; Liu, P.; Hoveyda, A. H. Diastereo- and Enantioselective Synthesis of Compounds with a Trifluoromethyl- and Fluorosubstituted Carbon Center and Their Unusual Chemistry. *Nat. Chem.* **2022**, *in revision*.
4. Zhou, Q.; Chin, M.; Fu, Y.; Liu, P.; Yang, Y. Unnatural Metalloredox Biocatalysis Enables Enantio- and Diastereocontrolled Atom Transfer Radical Cyclization. *Science* **2021**, *374*, 1612–1616.
5. Fu, Y.; Bernasconi, L.; Liu, P. *Ab Initio* Molecular Dynamics Simulations of the S_N1/S_N2 Mechanistic Continuum in Glycosylation Reactions. *J. Am. Chem. Soc.* **2021**, *143*, 1577–1589.
6. Lin, Q.; Fu, Y.; Liu, P.; Diao, T. Monovalent Nickel-Mediated Radical Formation: A Concerted Halogen-Atom Dissociation Pathway Determined by Electroanalytical Studies. *J. Am. Chem. Soc.* **2021**, *143*, 14196–14206.
7. Wu, T.-F.; Zhang, Y.-J.; Fu, Y.; Liu, F.-J.; Tang, J.-T.; Liu, P.; Toste, F. D.; Ye, B. Zirconium-Redox-Shuttled Cross-Electrophile Coupling of Aromatic and Heteroaromatic Halides. *Chem* **2021**, *7*, 1963–1974.

8. Ma, X.; Zheng, Z.; Fu, Y.; Zhu, X.; Liu, P.; Zhang, L. A “Traceless” Directing Group Enables Catalytic SN2 Glycosylation toward 1,2-Cis-Glycopyranosides. *J. Am. Chem. Soc.* **2021**, *143*, 11908–11913.

9. Lipshultz, J. M.; Fu, Y.; Liu, P.; Radosevich, A. T. Organophosphorus-Catalyzed Relay Oxidation of H-Bpin: Electrophilic C–H Borylation of Heteroarenes. *Chem. Sci.* **2021**, *12*, 1031-1037.

10. Li, Z.-Q.; Fu, Y.; Deng, R.; Tran, V. T.; Gao, Y.; Liu, P.; Engle, K. M. Ligand-Controlled Regiodivergence in Nickel-Catalyzed Hydroarylation and Hydroalkenylation of Alkenyl Carboxylic Acids. *Angew. Chem. Int. Ed.* **2020**, *59*, 23306–23312.

11. Wang, Q.; Fu, Y.; Zhu, W.; An, S.; Zhou, Q.; Zhu, S.-F.; He, G.; Liu, P.; Chen, G. Total Synthesis of C-α-Mannosyl Tryptophan via Palladium-catalyzed C–H Glycosylation. *CCS Chem.* **2020**, *2*, 1729–1736.

12. Leng, L.; Fu, Y.; Liu, P.; Ready, J. M. Regioselective, Photocatalytic α-Functionalization of Amines. *J. Am. Chem. Soc.* **2020**, *142*, 11972-11977.

13. Deng, L.; Fu, Y.; Lee, S. Y.; Wang, C.; Liu, P.; Dong, G. Kinetic Resolution via Rh-Catalyzed C–C Activation of Cyclobutanones at Room Temperature. *J. Am. Chem. Soc.* **2019**, *141*, 16260-16265.

Bibliography

[1] (a) Zhu, X.; Schmidt, R. R. New Principles for Glycoside-Bond Formation. *Angew. Chemie Int. Ed.* **2009**, *48*, 1900–1934. (b) Zhen, W.; S., C. Z.; G., A. S.; Wenjie, P.; Ryan, M.; P., de V. R.; John, G.; C., P. J.; Geert-Jan, B. A General Strategy for the Chemoenzymatic Synthesis of Asymmetrically Branched N-Glycans. *Science* **2013**, *341*, 379–383. (c) Danishefsky, S. J.; Shue, Y.-K.; Chang, M. N.; Wong, C.-H. Development of Globo-H Cancer Vaccine. *Acc. Chem. Res.* **2015**, *48*, 643–652.

[2] Frihed, T. G.; Bols, M.; Pedersen, C. M. Mechanisms of Glycosylation Reactions Studied by Low-Temperature Nuclear Magnetic Resonance. *Chem. Rev.* **2015**, *115*, 4963–5013.

[3] Hansen, T.; Lebedel, L.; Remmerswaal, W. A.; Van Der Vorm, S.; Wander, D. P. A.; Somers, M.; Overkleeft, H. S.; Filippov, D. V.; Désiré, J.; Mingot, A.; Bleriot, Y.; Van Der Marel, G. A.; Thibaudeau, S.; Codée, J. D. C. Defining the S_N1 Side of Glycosylation Reactions: Stereoselectivity of Glycopyranosyl Cations. *ACS Cent. Sci.* **2019**, *5*, 781–788.

[4] (a) Fang, T.; Gu, Y.; Huang, W.; Boons, G. J. Mechanism of Glycosylation of Anomeric Sulfonium Ions. *J. Am. Chem. Soc.* **2016**, *138*, 3002–3011. (b) Zhuo, M. H.; Wilbur, D. J.; Kwan, E. E.; Bennett, C. S. Matching Glycosyl Donor Reactivity to Sulfonate Leaving Group Ability Permits SN2 Glycosylations. *J. Am. Chem. Soc.* **2019**, *141*, 16743–16754.

[5] Park, Y.; Kim, Y.; Chang, S. Transition Metal-Catalyzed C–H Amination: Scope, Mechanism, and Applications. *Chem. Rev.* **2017**, *117*, 9247–9301.

[6] (a) Alderson, J. M.; Corbin, J. R.; Schomaker, J. M. Tunable, Chemo- and Site-Selective Nitrene Transfer Reactions through the Rational Design of Silver(I) Catalysts. *Acc. Chem. Res.*

2017, *50*, 2147–2158. (b) Ju, M.; Huang, M.; Vine, L. E.; Dehghany, M.; Roberts, J. M.; Schomaker, J. M. Tunable Catalyst-Controlled Syntheses of β- and γ-Amino Alcohols Enabled by Silver-Catalysed Nitrene Transfer. *Nat. Catal.* **2019**, *2*, 899–908. (c) Vine, L. E.; Zerull, E. E.; Schomaker, J. M. Taming Nitrene Reactivity with Silver Catalysts. *Synlett* **2021**, *32*, 30–44.

[7] Alderson, J. M.; Phelps, A. M.; Scamp, R. J.; Dolan, N. S.; Schomaker, J. M. Ligand-Controlled, Tunable Silver-Catalyzed C–H Amination. *J. Am. Chem. Soc.* **2014**, *136*, 16720–16723.

[8] Huang, M.; Yang, T.; Paretsky, J. D.; Berry, J. F.; Schomaker, J. M. Inverting Steric Effects: Using "Attractive" Noncovalent Interactions to Direct Silver-Catalyzed Nitrene Transfer. *J. Am. Chem. Soc.* **2017**, *139*, 17376–17386.

[9] (a) Huh, S.; Hong, S. Y.; Chang, S. Synthetic Utility of N-Benzoyloxyamides as an Alternative Precursor of Acylnitrenoids for γ-Lactam Formation. *Org. Lett.* **2019**, *21*, 2808–2812. (b) Jung, H.; Keum, H.; Kweon, J.; Chang, S. Tuning Triplet Energy Transfer of Hydroxamates as the Nitrene Precursor for Intramolecular C(Sp3)–H Amidation. *J. Am. Chem. Soc.* **2020**, *142*, 5811–5818.

[10] Zhou, Q.; Chin, M.; Fu, Y.; Liu, P.; Yang, Y. Stereodivergent Atom-Transfer Radical Cyclization by Engineered Cytochromes P450. *Science* **2021**, *374*, 1612–1616.

[11] For reviews: (a) Sibi, M. P.; Manyem, S.; Zimmerman, J. Enantioselective Radical Processes. *Chem. Rev.* **2003**, *103*, 3263–3296. (b) Proctor, R. S. J.; Colgan, A. C.; Phipps, R. J. Exploiting Attractive Non-Covalent Interactions for the Enantioselective Catalysis of Reactions Involving Radical Intermediates. *Nat. Chem.* **2020**, *12*, 990–1004. (c) Mondal, S.; Dumur, F.; Gigmes, D.; Sibi, M. P.; Bertrand, M. P.; Nechab, M. Enantioselective Radical Reactions Using Chiral

Catalysts. *Chem. Rev.* **2022**, *122*, 5842–5976.

[12] (a) Yang, D.; Gu, S.; Yan, Y.-L.; Zhu, N.-Y.; Cheung, K.-K. Highly Enantioselective Atom-Transfer Radical Cyclization Reactions Catalyzed by Chiral Lewis Acids. *J. Am. Chem. Soc.* **2001**, *123*, 8612–8613. (b) Chen, B.; Fang, C.; Liu, P.; Ready, J. M. Rhodium-Catalyzed Enantioselective Radical Addition of CX4 Reagents to Olefins. *Angew. Chem. Int. Ed.* **2017**, *56*, 8780–8784.

[13] Stick, R. V.; Williams, S. J. *Carbohydrates: The Essential Molecules of Life*, 2nd ed.; Elsevier: Amsterdam, 2009.

[14] (a) Crich, D. Mechanism of a Chemical Glycosylation Reaction. *Acc. Chem. Res.* **2010**, *43*, 1144–1153. (b) Mong, K. K. T.; Nokami, T.; Tran, N. T. T.; Nhi, P. B. Solvent Effect on Glycosylation. In *Selective Glycosylations: Synthetic Methods and Catalysts*; Bennett, C. S., Ed.; Wiley-VCH: Weinheim, 2017; pp 59−77.

[15] Seeberger, P. H. The Logic of Automated Glycan Assembly. *Acc. Chem. Res.* **2015**, *48*, 1450–1463.

[16] Chatterjee, S.; Moon, S.; Hentschel, F.; Gilmore, K.; Seeberger, P. H. An Empirical Understanding of the Glycosylation Reaction. *J. Am. Chem. Soc.* **2018**, *140*, 11942–11953.

[17] (a) Kozmon, S.; Tvaroška, I. Catalytic Mechanism of Glycosyltransferases: Hybrid Quantum Mechanical/Molecular Mechanical Study of the Inverting N-Acetylglucosaminyltransferase I. *J. Am. Chem. Soc.* **2006**, *128*, 16921–16927. (b) Krupička, M.; Tvaroška, I. Hybrid Quantum Mechanical/Molecular Mechanical Investigation of the *β*-1,4-Galactosyltransferase-I Mechanism. *J. Phys. Chem. B* **2009**, *113*, 11314–11319. (c) Biarnes, X.; Ardevol, A.; Iglesias-Fernández, J.; Planas, A.; Rovira, C. Catalytic Itinerary in 1,3-1,4-β-Glucanase Unraveled by QM/MM Metadynamics. Charge Is Not yet Fully Developed at the Oxocarbenium Ion-like

Transition State. *J. Am. Chem. Soc.* **2011**, *133*, 20301–20309. (d) Ardèvol, A.; Rovira, C. Reaction Mechanisms in Carbohydrate-Active Enzymes: Glycoside Hydrolases and Glycosyltransferases. Insights from *ab Initio* Quantum Mechanics/Molecular Mechanics Dynamic Simulations. *J. Am. Chem. Soc.* **2015,** *137*, 7528-7547. (e) Iglesias-Fernández, J.; Hancock, S. M.; Lee, S. S.; Khan, M.; Kirkpatrick, J.; Oldham, N. J.; McAuley, K.; Fordham-Skelton, A.; Rovira, C.; Davis, B. G. A front-face 'SNi synthase' engineered from a retaining 'double-S_N2' hydrolase. *Nat. Chem. Biol.* **2017,** *13*, 874-881. (f) Adero, P. O.; Amarasekara, H.; Wen, P.; Bohé, L.; Crich, D., The Experimental Evidence in Support of Glycosylation Mechanisms at the S_N1-S_N2 Interface. *Chem. Rev.* **2018,** *118*, 8242-8284.

[18] (a) Bohé, L.; Crich, D. A Propos of Glycosyl Cations and the Mechanism of Chemical Glycosylation. *C. R. Chim.* **2011**, *14*, 3–16. (b) Park, Y.; Harper, K. C.; Kuhl, N.; Kwan, E. E.; Liu, R. Y.; Jacobsen, E. N. Macrocyclic bis-thioureas catalyze stereospecific glycosylation reactions. *Science* **2017,** *355*, 162-166. (c) Leng, W. L.; Yao, H.; He, J. X.; Liu, X. W., Venturing beyond Donor-Controlled Glycosylation: New Perspectives toward Anomeric Selectivity. *Acc. Chem. Res.* **2018**, *51*, 628-639. (d) Santana, A. G.; Montalvillo-Jiménez, L.; Díaz-Casado, L.; Corzana, F.; Merino, P.; Cañada, F. J.; Jiménez-Osés, G.; Jiménez-Barbero, J.; Gómez, A. M.; Asensio, J. L. Dissecting the Essential Role of Anomeric β-Triflates in Glycosylation Reactions. *J. Am. Chem. Soc.* **2020**, *142*, 12501-12514.

[19] Ma, X.; Zheng, Z.; Fu, Y.; Zhu, X.; Liu, P.; Zhang, L. A “Traceless” Directing Group Enables Catalytic SN2 Glycosylation toward 1,2-Cis-Glycopyranosides. *J. Am. Chem. Soc.* **2021**, *143*, 11908–11913.

[20] (a) Yang, Z.; Doubleday, C.; Houk, K. N. QM/MM Protocol for Direct Molecular Dynamics of Chemical Reactions in Solution: The Water-Accelerated Diels-Alder Reaction. *J. Chem.*

Theory Comput. **2015**, *11*, 5606–5612. (b) Moors, S. L.; Brigou, B.; Hertsen, D.; Pinter, B.; Geerlings, P.; Van Speybroeck, V.; Catak, S.; De Proft, F. Influence of Solvation and Dynamics on the Mechanism and Kinetics of Nucleophilic Aromatic Substitution Reactions in Liquid Ammonia. *J. Org. Chem.* **2016,** *81*, 1635-1644. (c) Nieves-Quinones, Y.; Singleton, D. A. Dynamics and the Regiochemistry of Nitration of Toluene. *J. Am. Chem. Soc.* **2016**, *138*, 15167–15176. (d) Yang, Z.; Yang, S.; Yu, P.; Li, Y.; Doubleday, C.; Park, J.; Patel, A.; Jeon, B. sun; Russell, W. K.; Liu, H. wen; Russell, D. H.; Houk, K. N. Influence of Water and Enzyme SpnF on the Dynamics and Energetics of the Ambimodal [6+4]/[4+2] Cycloaddition. *Proc. Natl. Acad. Sci. U. S. A.* **2018**, *115*, E848–E855.

[21] (a) Barone, V.; Cossi, M. Quantum Calculation of Molecular Energies and Energy Gradients in Solution by a Conductor Solvent Model. *J. Phys. Chem. A* **1998**, *102*, 1995–2001. (b) Marenich, A. V.; Cramer, C. J.; Truhlar, D. G. Universal Solvation Model Based on Solute Electron Density and on a Continuum Model of the Solvent Defined by the Bulk Dielectric Constant and Atomic Surface Tensions. *J. Phys. Chem. B* **2009**, *113*, 6378–6396.

[22] Plata, R. E.; Singleton, D. A. A Case Study of the Mechanism of Alcohol-Mediated Morita Baylis-Hillman Reactions. the Importance of Experimental Observations. *J. Am. Chem. Soc.* **2015**, *137*, 3811–3826.

[23] (a) Kirschner, K. N.; Woods, R. J. Solvent Interactions Determine Carbohydrate Conformation. *Proc. Natl. Acad. Sci. U. S. A.* **2001**, *98*, 10541–10545. (b) Satoh, H.; Hansen, H. S.; Manabe, S.; van Gunsteren, W. F.; Hünenberger, P. H. Theoretical Investigation of Solvent Effects on Glycosylation Reactions: Stereoselectivity Controlled by Preferential Conformations of the Intermediate Oxacarbenium-Counterion Complex. *J. Chem. Theory Comput.* **2010,** *6*, 1783-1797. (c) Kafle, A.; Liu, J.; Cui, L. Controlling the Stereoselectivity of Glycosylation via

Solvent Effects. *Can. J. Chem.* **2016**, *94*, 894–901.

[24] Radu, I.; Peter, M.; E., T. M. Ab Initio Molecular Dynamics: Concepts, Recent Developments, and Future Trends. *Proc. Natl. Acad. Sci.* **2005**, *102*, 6654–6659.

[25] (a) Stubbs, J. M.; Marx, D., Glycosidic Bond Formation in Aqueous Solution: On the Oxocarbenium Intermediate. *J. Am. Chem. Soc.* **2003,** *125*, 10960-10962. (b) Stubbs, J. M.; Marx, D. Aspects of Glycosidic Bond Formation in Aqueous Solution: Chemical Bonding and the Role of Water. *Chem. - Eur. J.* **2005**, *11*, 2651–2659. (c) Peltzer, R. M.; Eisenstein, O.; Nova, A.; Cascella, M. How Solvent Dynamics Controls the Schlenk Equilibrium of Grignard Reagents: A Computational Study of CH_3MgCl in Tetrahydrofuran. *J. Phys. Chem. B* **2017**, *121*, 4226–4237. (d) Scalambra, F.; Holzmann, N.; Bernasconi, L.; Imberti, S.; Romerosa, A. Water Participation in Catalysis: An Atomistic Approach to Solvent Effects in the Catalytic Isomerization of Allylic Alcohols. *ACS Catal.* **2018**, *8*, 3812–3819. (e) Da Silva, G. C. Q.; Cardozo, T. M.; Amarante, G. W.; Abreu, C. R. A.; Horta, B. A. C. Solvent Effects on the Decarboxylation of Trichloroacetic Acid: Insights from: Ab Initio Molecular Dynamics Simulations. *Phys. Chem. Chem. Phys.* **2018**, *20*, 21988–21998.

[26] (a) Ensing, B.; Klein, M. L. Perspective on the Reactions between F^- and CH_3CH_2F: The Free Energy Landscape of the E2 and S_N2 Reaction Channels. *Proc. Natl. Acad. Sci. U. S. A.* **2005**, *102*, 6755–6759. (b) Gunaydin, H.; Houk, K. N. Molecular Dynamics Prediction of the Mechanism of Ester Hydrolysis in Water. *J. Am. Chem. Soc.* **2008,** *130*, 15232-15233. (c) Perez, D.; Uberuaga, B. P.; Shim, Y.; Amar, J. G.; Voter, A. F. Chapter 4 Accelerated Molecular Dynamics Methods: Introduction and Recent Developments. *Annu. Rep. Comput. Chem.* **2009**, *5*, 79–98. (d) Kuo, I. F. W.; Grant, C. D.; Gee, R. H.; Chinn, S. C.; Love, A. H. Determination of the Surface Effects on Sarin Degradation. *J. Phys. Chem. C* **2012**, *116*, 9631–9635. (e)

Tiwary, P.; van de Walle, A. A Review of Enhanced Sampling Approaches for Accelerated Molecular Dynamics. In *Multiscale Materials Modeling for Nanomechanics*; Weinberger, C. R., Tucker, G. J., Eds.; Springer International Publishing: Cham, 2016; pp 195−221. (f) Peltzer, R. M.; Gauss, J.; Eisenstein, O.; Cascella, M., The Grignard Reaction – Unraveling a Chemical Puzzle. *J. Am. Chem. Soc.* **2020,** *142*, 2984-2994.

[27] (a) Ensing, B.; De Vivo, M.; Liu, Z.; Moore, P.; Klein, M. L. Metadynamics as a Tool for Exploring Free Energy Landscapes of Chemical Reactions. *Acc. Chem. Res.* **2006**, *39*, 73–81. (b) Valsson, O.; Tiwary, P.; Parrinello, M. Enhancing Important Fluctuations: Rare Events and Metadynamics from a Conceptual Viewpoint. *Annu. Rev. Phys. Chem.* **2016**, *67*, 159–184. (c) Bussi, G.; Laio, A.; Tiwary, P. Metadynamics: A Unified Framework for Accelerating Rare Events and Sampling Thermodynamics and Kinetics. In *Handbook of Materials Modeling: Methods: Theory and Modeling*, Andreoni, W.; Yip, S., Eds. Springer International Publishing: Cham, 2020; pp 565-595.

[28] (a) Laio, A.; Gervasio, F. L. Metadynamics: A Method to Simulate Rare Events and Reconstruct the Free Energy in Biophysics, Chemistry and Material Science. *Reports Prog. Phys.* **2008**, *71*. (b) Galib, M.; Hanna, G. Mechanistic Insights into the Dissociation and Decomposition of Carbonic Acid in Water via the Hydroxide Route: An Ab Initio Metadynamics Study. *J. Phys. Chem. B* **2011**, *115*, 15024–15035.

[29] (a) Perdew, J. P.; Burke, K.; Ernzerhof, M. Generalized Gradient Approximation Made Simple. *Phys. Rev. Lett.* **1996**, *77*, 3865–3868. (b) Grimme, S.; Antony, J.; Ehrlich, S.; Krieg, H. A Consistent and Accurate *Ab Initio* Parametrization of Density Functional Dispersion Correction (DFT-D) for the 94 Elements H-Pu. *J. Chem. Phys.* **2010**, *132*, 154104.

[30] Anderson, J. A.; Tschumper, G. S. Characterizing the Potential Energy Surface of the Water Dimer with DFT: Failures of Some Popular Functionals for Hydrogen Bonding. *J. Phys. Chem. A* **2006**, *110*, 7268–7271.

[31] Towns, J.; Cockerill, T.; Dahan, M.; Foster, I.; Gaither, K.; Grimshaw, A.; Hazlewood, V.; Lathrop, S.; Lifka, D.; Peterson, G. D.; Roskies, R.; Scott, J. R.; Wilkins-Diehr, N. XSEDE: Accelerating Scientific Discovery. *Comput. Sci. Eng.* **2014**, *16*, 62–74.

[32] Frisch, M. J.; Trucks, G. W.; Schlegel, H. B.; Scuseria, G. E.; Robb, M. A.; Cheeseman, J. R.; Scalmani, G.; Barone, V.; Petersson, G. A.; Nakatsuji, H.; Li, X.; Caricato, M.; Marenich, A. V.; Bloino, J.; Janesko, B. G.; Gomperts, R.; Mennucci, B.; Hratchian, H. P.; Ortiz, J. V.; Izmaylov, A. F.; Sonnenberg, J. L.; Williams-Young, D.; Ding, F.; Lipparini, F.; Egidi, F.; Goings, J.; Peng, B.; Petrone, A.; Henderson, T.; Ranasinghe, D.; Zakrzewski, V. G.; Gao, J.; Rega, N.; Zheng, G.; Liang, W.; Hada, M.; Ehara, M.; Toyota, K.; Fukuda, R.; Hasegawa, J.; Ishida, M.; Nakajima, T.; Honda, Y.; Kitao, O.; Nakai, H.; Vreven, T.; Throssell, K.; Montgomery, J. A.; Peralta, J. E.; Ogliaro, F.; Bearpark, M. J.; Heyd, J. J.; Brothers, E. N.; Kudin, K. N.; Staroverov, V. N.; Keith, T. A.; Kobayashi, R.; Normand, J.; Raghavachari, K.; Rendell, A. P.; Burant, J. C.; Iyengar, S. S.; Tomasi, J.; Cossi, M.; Millam, J. M.; Klene, M.; Adamo, C.; Cammi, R.; Ochterski, J. W.; Martin, R. L.; Morokuma, K.; Farkas, O.; Foresman, J. B.; Fox, D. J., *Gaussian 16 Rev. C.01*, Wallingford, CT, 2016.

[33] Luchini, G.; Alegre-Requena, J. V.; Funes-Ardoiz, I.; Paton, R. S. *F1000 Research*, **2020**, *9*, 291.

[34] CYLview, 1.0b; Legault, C. Y., Université de Sherbrooke, **2009** (http://www.cylview.org)

[35] Pracht, P.; Bohle, F.; Grimme, S. Automated Exploration of the Low-Energy Chemical Space with Fast Quantum Chemical Methods. *Phys. Chem. Chem. Phys.* **2020**, *22*, 7169–7192.

[36] Bannwarth, C.; Ehlert, S.; Grimme, S. GFN2-xTB—An Accurate and Broadly Parametrized Self-Consistent Tight-Binding Quantum Chemical Method with Multipole Electrostatics and Density-Dependent Dispersion Contributions. *J. Chem. Theory Comput.* **2019**, *15*, 1652–1671.

[37] Yepes, D.; Neese, F.; List, B.; Bistoni, G. Unveiling the Delicate Balance of Steric and Dispersion Interactions in Organocatalysis Using High-Level Computational Methods. *J. Am. Chem. Soc.* **2020**, *142*, 3613–3625.

[38] (a) Krack, M.; Parrinello, M. In *QUICKSTEP:* Make the Atoms Dance; NIC Series; Forschungszentrum Jülich, 2004; p 29. (b) VandeVondele, J.; Krack, M.; Mohamed, F.; Parrinello, M.; Chassaing, T.; Hutter, J. Quickstep: Fast and Accurate Density Functional Calculations Using a Mixed Gaussian and Plane Waves Approach. *Comput. Phys. Commun.* **2005**, *167*, 103–128. (c) www.cp2k.org. CP2K Open Source Molecular Dynamics. https://www.cp2k.org/quickstep

[39] Lippert, G.; Hutter, J.; Parrinello, M. A Hybrid Gaussian and Plane Wave Density Functional Scheme. *Mol. Phys.* **1997**, *92*, 477–488.

[40] VandeVondele, J.; Hutter, J. Gaussian Basis Sets for Accurate Calculations on Molecular Systems in Gas and Condensed Phases. *J. Chem. Phys.* **2007**, *127*, 114105.

[41] Goedecker, S.; Teter, M.; Hutter, J. Separable Dual-Space Gaussian Pseudopotentials. *Phys. Rev. B* **1996**, *54*, 1703–1710.

[42] Marx, D.; Hutter, J. *Ab Initio Molecular Dynamics: Basic Theory and Advanced Methods;* Cambridge University Press: Cambridge, U.K., 2009.

[43] (a) Nosé, S. A Unified Formulation of the Constant Temperature Molecular Dynamics Methods. *J. Chem. Phys.* **1984**, *81*, 511–519. (b) Hoover, W. G. Canonical Dynamics: Equilibrium Phase-Space Distributions. *Phys. Rev. A* **1985**, *31*, 1695–1697. (c) Martyna, G. J.;

Klein, M. L.; Tuckerman, M. Nosé–Hoover Chains: The Canonical Ensemble via Continuous Dynamics. *J. Chem. Phys.* **1992**, *97*, 2635–2643.

[44] (a) Laio, A.; Parrinello, M. Escaping Free-Energy Minima. *Proc. Natl. Acad. Sci. U. S. A.* **2002**, *99*, 12562-12566. (b) Hutter, J.; Iannuzzi, M.; Schiffmann, F.; VandeVondele, J. Cp2k: Atomistic Simulations of Condensed Matter Systems. *WIREs Comput. Mol. Sci.* **2014**, *4*, 15–25.

[45] Iannuzzi, M.; Laio, A.; Parrinello, M. Efficient Exploration of Reactive Potential Energy Surfaces Using Car-Parrinello Molecular Dynamics. *Phys. Rev. Lett.* **2003**, *90*, 4.

[46] (a) Doubleday, C.; Bolton, K.; Hase, W. L. Direct Dynamics Quasiclassical Trajectory Study of the Thermal Stereomutations of Cyclopropane. *J. Phys. Chem. A* **1998**, *102*, 3648–3658. (b) Black, K.; Liu, P.; Xu, L.; Doubleday, C.; Houk, K. N. Dynamics, Transition States, and Timing of Bond Formation in Diels-Alder Reactions. *Proc. Natl. Acad. Sci. U. S. A.* **2012**, *109*, 12860–12865. (c) Patel, A.; Chen, Z.; Yang, Z.; Gutiérrez, O.; Liu, H. W.; Houk, K. N.; Singleton, D. A. Dynamically Complex [6+4] and [4+2] Cycloadditions in the Biosynthesis of Spinosyn A. *J. Am. Chem. Soc.* **2016**, *138*, 3631–3634. (d) Yu, P.; Yang, Z.; Liang, Y.; Hong, X.; Li, Y.; Houk, K. N. Distortion-Controlled Reactivity and Molecular Dynamics of Dehydro-Diels-Alder Reactions. *J. Am. Chem. Soc.* **2016**, *138*, 8247–8252.

[47] Khamar, D.; Zeglinski, J.; Mealey, D.; Rasmuson, A. C. Investigating the Role of Solvent-Solute Interaction in Crystal Nucleation of Salicylic Acid from Organic Solvents. *J. Am. Chem. Soc.* **2014**, *136*, 11664–11673.

[48] To save computational cost, the methylated donor **2-7** was used in the AIMD simulations as a model of the benzylated donor **2-5**.

[49] Qiao, Y.; Ge, W.; Jia, L.; Hou, X.; Wang, Y.; Pedersen, C. M. Glycosylation Intermediates

Studied Using Low Temperature 1H- and 19F-DOSY NMR: New Insight into the Activation of Trichloroacetimidates. *Chem. Commun.* **2016**, *52*, 11418–11421.

[50] Our simulation performed at room temperature with higher concentration of donor (~0.3 M) and acceptor (~0.3 M) is likely to be more favorable for S_N2-type mechanism. Stronger nucleophiles and lower temperatures favor to produce the stereo-inverted products.

[51] Although not included in the AIMD simulations in the present study, counterions, especially those can potentially coordinate to oxocarbenium ions, may affect the glycosylation mechanisms and stereoselectivity (see, for example, entries 2 and 3 in Table 1). AIMD studies of counterion effects are currently ongoing in our laboratories.

[52] (a) Bussi, G.; Branduardi, D. Free-Energy Calculations with Metadynamics: Theory and Practice. *Rev. Comput. Chem.* **2015**, 28, 1–49. (b) Laio, A.; Rodriguez-Fortea, A.; Gervasio, F. L.; Ceccarelli, M.; Parrinello, M. Assessing the Accuracy of Metadynamics. *J. Phys. Chem. B* **2005,** *109*, 6714-6721. (c) Bussi, G.; Laio, A. Using metadynamics to explore complex free-energy landscapes. *Nat. Rev. Phys.* 2020, **2**, 200-212.

[53] These distances were obtained from the saddle point on the FES shown in Figure 2-7b. It should be noted that the representative snapshot of **TS1-a** in Figure 2-7c has slightly different bond distances because the snapshot is close to but not on the exact saddle point. Similarly, in the following discussions, the bond distances of representative snapshots may slightly deviate from the bond distances of the stationary points on the FES.

[54] (a) Huang, M.; Garrett, G. E.; Birlirakis, N.; Bohé, L.; Pratt, D. A.; Crich, D. Dissecting the Mechanisms of a Class of Chemical Glycosylation Using Primary ^{13}C Kinetic Isotope Effects. *Nat. Chem.* **2012**, *4*, 663–667. (b) Chan, J.; Sannikova, N.; Tang, A.; Bennet, A. J. Transition-State Structure for the Quintessential S_N2 Reaction of a Carbohydrate: Reaction of *α*-

Glucopyranosyl Fluoride with Azide Ion in Water. *J. Am. Chem. Soc.* **2014,** *136*, 12225-12228.

[55] (a) Jiménez-Osés, G.; Liu, P.; Matute, R. A.; Houk, K. N. Competition between Concerted and Stepwise Dynamics in the Triplet Di-π-Methane Rearrangement. *Angew. Chem. Int. Ed.* **2014**, *53*, 8664–8667. (b) Collins, P.; Kramer, Z. C.; Carpenter, B. K.; Ezra, G. S.; Wiggins, S. Nonstatistical Dynamics on the Caldera. *J. Chem. Phys.* **2014**, *141*, 034111-034117. (c) Carpenter, B. K.; Harvey, J. N.; Orr-Ewing, A. J. The Study of Reactive Intermediates in Condensed Phases. *J. Am. Chem. Soc.* **2016**, *138*, 4695–4705. (d) Pratihar, S.; Ma, X.; Homayoon, Z.; Barnes, G. L.; Hase, W. L. Direct Chemical Dynamics Simulations. *J. Am. Chem. Soc.* **2017**, *139*, 3570–3590. (e) Aziz, H. R.; Singleton, D. A. Concert along the Edge: Dynamics and the Nature of the Border between General and Specific Acid-Base Catalysis. *J. Am. Chem. Soc.* **2017**, *139*, 5965–5972. (f) Bailey, J. O.; Singleton, D. A. Failure and Redemption of Statistical and Nonstatistical Rate Theories in the Hydroboration of Alkenes. *J. Am. Chem. Soc.* **2017**, *139*, 15710–15723. (g) Liu, X.; Zhang, J.; Yang, L.; Hase, W. L. How a Solvent Molecule Affects Competing Elimination and Substitution Dynamics. Insight into Mechanism Evolution with Increased Solvation. *J. Am. Chem. Soc.* **2018**, *140*, 10995–11005. (h) Roytman, V. A.; Jin, S.; Nguyen, V. T.; Nguyen, V. D.; Haug, G. C.; Larionov, O. V.; Singleton, D. A. Bond Memory in Dynamically Determined Stereoselectivity. *J. Am. Chem. Soc.* **2020**, *142*, 85–88.

[56] (a) Xu, L.; Doubleday, C. E.; Houk, K. N. Dynamics of carbene cycloadditions. *J. Am. Chem. Soc.* **2011,** *133*, 17848-17854. (b) Törk, L.; Jiménez-Osés, G.; Doubleday, C.; Liu, F.; Houk, K. N. Molecular dynamics of the Diels-Alder reactions of tetrazines with alkenes and N_2 extrusions from adducts. *J. Am. Chem. Soc.* **2015,** *137*, 4749-4758. (c) Yang, Z.; Jamieson, C. S.; Xue, X. S.; Garcia-Borràs, M.; Benton, T.; Dong, X.; Liu, F.; Houk, K. N. Mechanisms and

Dynamics of Reactions Involving Entropic Intermediates. *Trends Chem.* **2019**, *1*, 22–34.

[57] (a) Liu, F.; Yang, Z.; Mei, Y.; Houk, K. N. QM/QM′ Direct Molecular Dynamics of Water-Accelerated Diels-Alder Reaction. *J. Phys. Chem. B* **2016**, *120*, 6250–6254. (b) Grayson, M. N.; Yang, Z.; Houk, K. N. Chronology of CH···O Hydrogen Bonding from Molecular Dynamics Studies of the Phosphoric Acid-Catalyzed Allylboration of Benzaldehyde. *J. Am. Chem. Soc.* **2017**, *139*, 7717–7720. (c) Roytman, V. A.; Singleton, D. A. Solvation Dynamics and the Nature of Reaction Barriers and Ion-Pair Intermediates in Carbocation Reactions. *J. Am. Chem. Soc.* **2020**, *142*, 12865–12877.

[58] (a) Dellago, C.; Bolhuis, P. G.; Chandler, D. Efficient Transition Path Sampling: Application to Lennard-Jones Cluster Rearrangements. *J. Chem. Phys.* **1998**, *108*, 9236–9245. (b) Bolhuis, P. G.; Chandler, D.; Dellago, C.; Geissler, P. L. Transition Path Sampling: Throwing Ropes over Rough Mountain Passes, in the Dark. *Annu. Rev. Phys. Chem.* **2002**, *53*, 291–318. (c) Jung, H.; Okazaki, K. I.; Hummer, G. Transition Path Sampling of Rare Events by Shooting from the Top. *J. Chem. Phys.* **2017**, *147*, 152716.

[59] Although the $^4C_1$ (chair) conformation of the product is expected to be more stable, conformational change from $^1S_3$ (skew boat) to $^4C_1$ (chair) was not observed during the 1 ps simulation, indicating such process occurs on a longer timescale. For detailed discussions on the relative stabilities of conformers of β-D-glucose see: Ref. 17d.

[60] Baldwin, J. E.; Fleming, R. H. Allene-Olefin and Allene-Allene Cycloadditions Methylenecyclobutane and 1,2-Dimethylenecyclobutane Degenerate Rearrangements. *Fortsch. Chem. Forschung* **1970**, 15, 281.

[61] Moon, S.; Chatterjee, S.; Seeberger, P. H.; Gilmore, K. Predicting Glycosylation Stereoselectivity Using Machine Learning. *Chem. Sci.* **2021**, *12*, 2931–2939.

[62] (a) Pougny, J. R.; Sinaÿ, P. Reaction d'imidates de Glucopyranosyle Avec l'acetonitrile. Applications Synthetiques. *Tetrahedron Lett.* **1976**, *17*, 4073–4076. (b) Ratcliffe, A. J.; Fraser-Reid, B. Generation of α-D-Glucopyranosylacetonitrilium Ions. Concerning the Reverse Anomeric Effect. *J. Chem. Soc. Perkin Trans. 1* **1990**, No. 3, 747–750. (c) Braccini, I.; Derouet, C.; Esnault, J.; de Penhoat, C. H.; Mallet, J. M.; Michon, V.; Sinaÿ, P. Conformational Analysis of Nitrilium Intermediates in Glycosylation Reactions. *Carbohydr. Res.* **1993**, *246*, 23–41.

[63] Doubleday, C.; Boguslav, M.; Howell, C.; Korotkin, S. D.; Shaked, D. Trajectory Calculations for Bergman Cyclization Predict H/D Kinetic Isotope Effects Due to Nonstatistical Dynamics in the Product. *J. Am. Chem. Soc.* **2016**, *138*, 7476–7479.

[64] (a) Zhu, J.; Bennet, A. J. Hydrolysis of (2-Deoxy-α-D-Glucopyranosyl)Pyridinium Salts: The 2- Deoxyglucosyl Oxocarbenium Is Not Solvent-Equilibrated in Water. *J. Am. Chem. Soc.* **1998**, *120*, 3887–3893. (b) Amyes, T. L.; Jencks, W. P. Lifetimes of Oxocarbenium Ions in Aqueous Solution from Common Ion Inhibition of the Solvolysis of *α*-Azido Ethers by Added Azide Ion. *J. Am. Chem. Soc.* **1989**, *111*, 7888–7900.

[65] Chan, J.; Tang, A.; Bennet, A. J. A Stepwise Solvent-Promoted S_Ni Reaction of α-D-Glucopyranosyl Fluoride: Mechanistic Implications for Retaining Glycosyltransferases. *J. Am. Chem. Soc.* **2012**, *134*, 1212–1220.

[66] The solvent/solute interaction energies ($\Delta E_{sol\text{-}interaction}$) were calculated in the same fashion to those reported in Figure 2-13D. The same C^1–O^{LG} and C^1–O^{Nu} distances were used for the S_N2-transition state-type structure and the oxocarbenium intermediate. These distances are slightly different from those in **Int-d**. As a result, the free energy of the oxocarbenium intermediate reported in Figure 2-15D is slightly higher than that of **Int-d** in Figure 2-15B.

[67] The median lifetime of the oxocarbenium intermediate in MTBE cannot be obtained from the

BOMD-QCT simulations because more than 50% of the trajectories remained in the oxocarbenium region after the 5 ps simulation. According to the activation free energies of **TS1-d** and **TS2-d** from the metadynamics simulations (9.8 and 9.2 kcal/mol with respect to **Int-d**), the lifetime of the oxocarbenium intermediate **Int-d** is on the order of nanosecond (10^{-9} s) if the reaction followed statistical dynamics as described by the Eyring equation.

[68] (a) Kalikanda, J.; Li, Z. Study of the Stereoselectivity of 2-Azido-2-Deoxygalactosyl Donors: Relationship to the Steric Factors of Glycosyl Acceptors. *Carbohydr. Res.* **2011**, *346*, 2380–2383. (b) van der Vorm, S.; Hansen, T.; Overkleeft, H. S.; van der Marel, G. A.; Codée, J. D. C. The Influence of Acceptor Nucleophilicity on the Glycosylation Reaction Mechanism. *Chem. Sci.* **2017**, *8*, 1867–1875. (c) van der Vorm, S.; Overkleeft, H. S.; van der Marel, G. A.; Codée, J. D. C. Stereoselectivity of Conformationally Restricted Glucosazide Donors. *J. Org. Chem.* **2017**, *82*, 4793–4811. (d) van der Vorm, S.; van Hengst, J. M. A.; Bakker, M.; Overkleeft, H. S.; van der Marel, G. A.; Codée, J. D. C. Mapping the Relationship between Glycosyl Acceptor Reactivity and Glycosylation Stereoselectivity. *Angew. Chem. Int. Ed.* **2018**, *57*, 8240–8244.

[69] Doubleday, C.; Suhrada, C. P.; Houk, K. N. Dynamics of the Degenerate Rearrangement of Bicyclo[3.1.0]Hex-2-Ene. *J. Am. Chem. Soc.* **2006**, *128*, 90–94.

[70] (a) Müller, P.; Fruit, C. Enantioselective catalytic aziridinations and asymmetric nitrene insertions into C–H bonds. *Chem. Rev.* **2003**, *103*, 2905–2920. (b) Díaz-Requejo, M. M.; Belderraín, T. R.; Nicasio, M. C.; Trofimenko, S.; Pérez, P. J. Cyclohexane and Benzene Amination by Catalytic Nitrene Insertion into C−H Bonds with the Copper-Homoscorpionate Catalyst TpBr3Cu(NCMe). *J. Am. Chem. Soc.* **2003**, *125*, 12078–12079. (c) Li, Z.; Capretto, D. A.; Rahaman, R.; He, C. Silver-Catalyzed Intermolecular Amination of C−H Groups.

Angew. Chemie Int. Ed. **2007**, *46*, 5184–5186. (d) Roizen, J. L.; Harvey, M. E.; Du Bois, J. Metal-Catalyzed Nitrogen-Atom Transfer Methods for the Oxidation of Aliphatic C–H Bonds. *Acc. Chem. Res.* **2012**, *45*, 911–922. (e) Hazelard, D.; Nocquet, P. A.; Compain, P. Catalytic C–H amination at its limits: challenges and solutions. *Org. Chem. Front.* **2017**, *4,* 2500–2521. (f) Lang, K.; Torker, S.; Wojtas, L.; Zhang, X. P. Asymmetric Induction and Enantiodivergence in Catalytic Radical C–H Amination via Enantiodifferentiative H-Atom Abstraction and Stereoretentive Radical Substitution. *J. Am. Chem. Soc.* **2019**, *141*, 12388–12396. (g) Lang, K.; Li, C.; Kim, I.; Zhang, X. P. Enantioconvergent Amination of Racemic Tertiary C–H Bonds. *J. Am. Chem. Soc.* **2020**, *142*, 20902–20911.

[71] Sun, Y.; Tang, H.; Chen, K.; Hu, L.; Yao, J.; Shaik, S.; Chen, H. Two-State Reactivity in Low-Valent Iron-Mediated C–H Activation and the Implications for Other First-Row Transition Metals. *J. Am. Chem. Soc.* **2016**, *138*, 3715–3730.

[72] Park, S. H.; Kwak, J.; Shin, K.; Ryu, J.; Park, Y.; Chang, S. Mechanistic Studies of the Rhodium-Catalyzed Direct C–H Amination Reaction Using Azides as the Nitrogen Source. *J. Am. Chem. Soc.* **2014**, *136*, 2492–2502.

[73] (a) Lin, X.; Zhao, C.; Che, C.-M.; Ke, Z.; Phillips, D. L. A DFT Study on the Mechanism of Rh2II,II-Catalyzed Intramolecular Amidation of Carbamates. *Chem. – An Asian J.* **2007**, *2*, 1101–1108. (b) Lin, X.; Sun, J.; Xi, Y.; Pang, B. Computational Interpretation of the Stereoselectivity for a Dirhodium Tetracarboxylate-Catalyzed Amidation Reaction. *Comput. Theor. Chem.* **2011**, *963*, 284–289. (c) Roca-Sabio, A.; Regueiro-Figueroa, M.; Esteban-Gómez, D.; de Blas, A.; Rodríguez-Blas, T.; Platas-Iglesias, C. Density Functional Dependence of Molecular Geometries in Lanthanide(III) Complexes Relevant to Bioanalytical and Biomedical Applications. *Comput. Theor. Chem.* **2012**, *999*, 93–104.

[74] Guo, Z.; Guan, X.; Huang, J.-S.; Tsui, W.-M.; Lin, Z.; Che, C.-M. Bis(Sulfonylimide)Ruthenium(VI) Porphyrins: X-Ray Crystal Structure and Mechanism of C–H Bond Amination by Density Functional Theory Calculations. *Chem. – A Eur. J.* **2013**, *19*, 11320–11331.

[75] Aguila, M. J. B.; Badiei, Y. M.; Warren, T. H. Mechanistic Insights into C–H Amination via Dicopper Nitrenes. *J. Am. Chem. Soc.* **2013**, *135*, 9399–9406.

[76] Lyaskovskyy, V.; Suarez, A. I. O.; Lu, H.; Jiang, H.; Zhang, X. P.; De Bruin, B. Mechanism of Cobalt(II) Porphyrin-Catalyzed C-H Amination with Organic Azides: Radical Nature and H-Atom Abstraction Ability of the Key Cobalt(III)-Nitrene Intermediates. *J. Am. Chem. Soc.* **2011**, *133*, 12264–12273.

[77] Liu, Y.; Guan, X.; Wong, E. L.-M.; Liu, P.; Huang, J.-S.; Che, C.-M. Nonheme Iron-Mediated Amination of C(Sp3)–H Bonds. Quinquepyridine-Supported Iron-Imide/Nitrene Intermediates by Experimental Studies and DFT Calculations. *J. Am. Chem. Soc.* **2013**, *135*, 7194–7204.

[78] Harvey, M. E.; Musaev, D. G.; Du Bois, J. A Diruthenium Catalyst for Selective, Intramolecular Allylic C–H Amination: Reaction Development and Mechanistic Insight Gained through Experiment and Theory. *J. Am. Chem. Soc.* **2011**, *133*, 17207–17216.

[79] Barman, D. N.; Liu, P.; Houk, K. N.; Nicholas, K. M. On the Mechanism of Ligand-Assisted, Copper-Catalyzed Benzylic Amination by Chloramine-T. *Organometallics* **2010**, *29*, 3404–3412.

[80] (a) Sigman, M. S.; Harper, K. C.; Bess, E. N.; Milo, A. The Development of Multidimensional Analysis Tools for Asymmetric Catalysis and Beyond. *Acc. Chem. Res.* **2016**, *49*, 1292–1301. (b) Williams, W. L.; Zeng, L.; Gensch, T.; Sigman, M. S.; Doyle, A. G.; Anslyn, E. V. The Evolution of Data-Driven Modeling in Organic Chemistry. *ACS Cent. Sci.* **2021**, *7*, 1622–1637.

[81] Sigman, M. S.; Harper, K. C.; Bess, E. N.; Milo, A. The Development of Multidimensional Analysis Tools for Asymmetric Catalysis and Beyond. *Acc. Chem. Res.* **2016**, *49*, 1292–1301.

[82] (a) Liu, F.; Yang, Z.; Yu, Y.; Mei, Y.; Houk, K. N. Bimodal Evans-Polanyi Relationships in Dioxirane Oxidations of Sp3 C-H: Non-Perfect Synchronization in Generation of Delocalized Radical Intermediates. *J. Am. Chem. Soc.* **2017**, *139*, 16650–16656. (b) Liu, F.; Ma, S.; Lu, Z.; Nangia, A.; Duan, M.; Yu, Y.; Xu, G.; Mei, Y.; Bietti, M.; Houk, K. N. Hydrogen Abstraction by Alkoxyl Radicals: Computational Studies of Thermodynamic and Polarity Effects on Reactivities and Selectivities. *J. Am. Chem. Soc.* **2022**, *144*, 6802–6812.

[83] (a) Chen, M. S.; White, M. C. Combined Effects on Selectivity in Fe-Catalyzed Methylene Oxidation. *Science* **2010**, *327*, 566–571. (b) Gormisky, P. E.; White, M. C. Catalyst-Controlled Aliphatic C–H Oxidations with a Predictive Model for Site-Selectivity. *J. Am. Chem. Soc.* **2013**, *135*, 14052–14055. (c) Paradine, S. M.; Griffin, J. R.; Zhao, J.; Petronico, A. L.; Miller, S. M.; Christina White, M. A Manganese Catalyst for Highly Reactive yet Chemoselective Intramolecular C(Sp 3)-H Amination. *Nat. Chem.* **2015**, *7*, 987–994. (d) Clark, J. R.; Feng, K.; Sookezian, A.; White, M. C. Manganese-Catalysed Benzylic C(Sp3)–H Amination for Late-Stage Functionalization. *Nat. Chem.* **2018**, *10*, 583–591. (e) White, M. C.; Zhao, J. Aliphatic C–H Oxidations for Late-Stage Functionalization. *J. Am. Chem. Soc.* **2018**, *140*, 13988–14009.

[84] Dolan, N. S.; Scamp, R. J.; Yang, T.; Berry, J. F.; Schomaker, J. M. Catalyst-Controlled and Tunable, Chemoselective Silver-Catalyzed Intermolecular Nitrene Transfer: Experimental and Computational Studies. *J. Am. Chem. Soc.* **2016**, *138*, 14658–14667.

[85] Alderson, J. M.; Corbin, J. R.; Schomaker, J. M. Investigation of Transition Metal-Catalyzed Nitrene Transfer Reactions in Water. *Bioorg. Med. Chem.* **2018**, *26*, 5270–5273.

[86] Chai, J.-D.; Head-Gordon, M. Long-Range Corrected Hybrid Density Functionals with

Damped Atom–Atom Dispersion Corrections. *Phys. Chem. Chem. Phys.* **2008**, *10*, 6615–6620.

[87] Ma, Q.; Schwilk, M.; Köppl, C.; Werner, H.-J. Scalable Electron Correlation Methods. 4. Parallel Explicitly Correlated Local Coupled Cluster with Pair Natural Orbitals (PNO-LCCSD-F12). *J. Chem. Theory Comput.* **2017**, *13*, 4871–4896.

[88] Ma, Q.; Werner, H.-J. Scalable Electron Correlation Methods. 7. Local Open-Shell Coupled-Cluster Methods Using Pair Natural Orbitals: PNO-RCCSD and PNO-UCCSD. *J. Chem. Theory Comput.* **2020**, *16*, 3135–3151.

[89] (a) Werner, H.-J.; Knowles, P. J.; Knizia, G.; Manby, F. R.; Schütz, M. Molpro: A General-Purpose Quantum Chemistry Program Package. *WIREs Comput. Mol. Sci.* **2012**, *2*, 242–253. (b) Werner, H.-J.; Knowles, P. J.; Manby, F. R.; Black, J. A.; Doll, K.; Heßelmann, A.; Kats, D.; Köhn, A.; Korona, T.; Kreplin, D. A.; Ma, Q.; Miller, T. F.; Mitrushchenkov, A.; Peterson, K. A.; Polyak, I.; Rauhut, G.; Sibaev, M. The Molpro Quantum Chemistry Package. *J. Chem. Phys.* **2020**, *152*, 144107.

[90] Ma, Q.; Werner, H. J. Scalable Electron Correlation Methods. 8. Explicitly Correlated Open-Shell Coupled-Cluster with Pair Natural Orbitals PNO-RCCSD(T)-F12 and PNO-UCCSD(T)-F12. *J. Chem. Theory Comput.* **2021**, *17*, 902–926.

[91] Ma, Q.; Werner, H.-J. Accurate Intermolecular Interaction Energies Using Explicitly Correlated Local Coupled Cluster Methods [PNO-LCCSD(T)-F12]. *J. Chem. Theory Comput.* **2019**, *15*, 1044–1052.

[92] Jiang, W.; DeYonker, N. J.; Wilson, A. K. Multireference Character for 3d Transition-Metal-Containing Molecules *J. Chem. Theory Comput.* **2012**, *8*, 460–468.

[93] Pierloot, K.; Phung, Q. M.; Domingo, A. Spin State Energetics in First-Row Transition Metal Complexes: Contribution of (3s3p) Correlation and Its Description by Second-Order

Perturbation Theory. *J. Chem. Theory Comput.* **2017**, *13*, 537–553.

[94] (a) Fdez. Galván, I.; Vacher, M.; Alavi, A.; Angeli, C.; Aquilante, F.; Autschbach, J.; Bao, J. J.; Bokarev, S. I.; Bogdanov, N. A.; Carlson, R. K.; Chibotaru, L. F.; Creutzberg, J.; Dattani, N.; Delcey, M. G.; Dong, S. S.; Dreuw, A.; Freitag, L.; Frutos, L. M.; Gagliardi, L.; Gendron, F.; Giussani, A.; González, L.; Grell, G.; Guo, M.; Hoyer, C. E.; Johansson, M.; Keller, S.; Knecht, S.; Kovačević, G.; Källman, E.; Li Manni, G.; Lundberg, M.; Ma, Y.; Mai, S.; Malhado, J. P.; Malmqvist, P. Å.; Marquetand, P.; Mewes, S. A.; Norell, J.; Olivucci, M.; Oppel, M.; Phung, Q. M.; Pierloot, K.; Plasser, F.; Reiher, M.; Sand, A. M.; Schapiro, I.; Sharma, P.; Stein, C. J.; Sørensen, L. K.; Truhlar, D. G.; Ugandi, M.; Ungur, L.; Valentini, A.; Vancoillie, S.; Veryazov, V.; Weser, O.; Wesołowski, T. A.; Widmark, P.-O.; Wouters, S.; Zech, A.; Zobel, J. P.; Lindh, R. OpenMolcas: From Source Code to Insight. *J. Chem. Theory Comput.* **2019**, *15*, 5925–5964. (b) Aquilante, F.; Autschbach, J.; Baiardi, A.; Battaglia, S.; Borin, V. A.; Chibotaru, L. F.; Conti, I.; De Vico, L.; Delcey, M.; Fdez. Galván, I.; Ferré, N.; Freitag, L.; Garavelli, M.; Gong, X.; Knecht, S.; Larsson, E. D.; Lindh, R.; Lundberg, M.; Malmqvist, P. Å.; Nenov, A.; Norell, J.; Odelius, M.; Olivucci, M.; Pedersen, T. B.; Pedraza-González, L.; Phung, Q. M.; Pierloot, K.; Reiher, M.; Schapiro, I.; Segarra-Martí, J.; Segatta, F.; Seijo, L.; Sen, S.; Sergentu, D.-C.; Stein, C. J.; Ungur, L.; Vacher, M.; Valentini, A.; Veryazov, V. Modern Quantum Chemistry with [Open]Molcas. *J. Chem. Phys.* **2020**, *152*, 214117.

[95] (a) Gómez-Emeterio, B. P.; Urbano, J.; Díaz-Requejo, M. M.; Pérez, P. J. Easy Alkane Catalytic Functionalization. *Organometallics* **2008**, *27*, 4126–4130. (b) Collet, F.; Lescot, C.; Dauban, P. Catalytic C–H Amination: The Stereoselectivity Issue. *Chem. Soc. Rev.* **2011**, *40*, 1926–1936.

[96] For κ^2-coordinated Cu nitrene complexes, see: (a) Moegling, J.; Hoffmann, A.; Thomas, F.;

Orth, N.; Liebhäuser, P.; Herber, U.; Rampmaier, R.; Stanek, J.; Fink, G.; Ivanović-Burmazović, I.; Herres-Pawlis, S. Designed To React: Terminal Copper Nitrenes and Their Application in Catalytic C−H Aminations. *Angew. Chemie Int. Ed.* **2018**, *57*, 9154–9159. (b) Thomas, F.; Oster, M.; Schön, F.; Göbgen, K. C.; Amarouch, B.; Steden, D.; Hoffmann, A.; Herres-Pawlis, S. A New Generation of Terminal Copper Nitrenes and Their Application in Aromatic C–H Amination Reactions. *Dalt. Trans.* **2021**, *50*, 6444–6462.

[97] Because PhIO is insoluble, mass-transport may also be the rate-determining step. Previously reported nonideal kinetic behavior suggested that the solubility of PhIO may affect the reaction rate. See: *Organometallics* **2017**, *36*, 1649.

[98] To the best of our knowledge, Ag nitrene intermediates in Ag NT reactions have not been isolated. For characterization of Rh nitrene complexes, see: (a) Das, A.; Chen, Y.-S.; Reibenspies, J. H.; Powers, D. C. Characterization of a Reactive Rh2 Nitrenoid by Crystalline Matrix Isolation. *J. Am. Chem. Soc.* **2019**, *141*, 16232–16236. (b) Das, A.; Wang, C.-H.; Van Trieste, G. P.; Sun, C.-J.; Chen, Y.-S.; Reibenspies, J. H.; Powers, D. C. In Crystallo Snapshots of Rh2-Catalyzed C–H Amination. *J. Am. Chem. Soc.* **2020**, *142*, 19862–19867.

[99] Maestre, L.; Sameera, W. M. C.; Díaz-Requejo, M. M.; Maseras, F.; Pérez, P. J. A General Mechanism for the Copper- and Silver-Catalyzed Olefin Aziridination Reactions: Concomitant Involvement of the Singlet and Triplet Pathways. *J. Am. Chem. Soc.* **2013**, *135*, 1338–1348.

[100] Short, M. A.; Blackburn, J. M.; Roizen, J. L. Modifying Positional Selectivity in C–H Functionalization Reactions with Nitrogen-Centered Radicals: Generalizable Approaches to 1,6-Hydrogen-Atom Transfer Processes. *Synlett* **2020**, *31*, 102–116.

[101] Chen, M. S.; White, M. C. A Predictably Selective Aliphatic C–H Oxidation Reaction for Complex Molecule Synthesis. *Science* **2007**, *318*, 783–787.

[102] Badiei, Y. M.; Dinescu, A.; Dai, X.; Palomino, R. M.; Heinemann, F. W.; Cundari, T. R.; Warren, T. H. Copper–Nitrene Complexes in Catalytic C–H Amination. *Angew. Chemie Int. Ed.* **2008**, *47*, 9961–9964.

[103] For bimodal relationships between C–H BDE and the reactivity of dioxirane-mediated C–H oxidations, see: Liu, F.; Yang, Z.; Yu, Y.; Mei, Y.; Houk, K. N. Bimodal Evans–Polanyi Relationships in Dioxirane Oxidations of Sp3 C–H: Non-Perfect Synchronization in Generation of Delocalized Radical Intermediates. *J. Am. Chem. Soc.* **2017**, *139*, 16650–16656.

[104] Salamone, M.; Galeotti, M.; Romero-Montalvo, E.; van Santen, J. A.; Groff, B. D.; Mayer, J. M.; DiLabio, G. A.; Bietti, M. Bimodal Evans–Polanyi Relationships in Hydrogen Atom Transfer from C(Sp3)–H Bonds to the Cumyloxyl Radical. A Combined Time-Resolved Kinetic and Computational Study. *J. Am. Chem. Soc.* **2021**, *143*, 11759–11776.

[105] (a) Espino, C. G.; Fiori, K. W.; Kim, M.; Du Bois, J. Expanding the Scope of C−H Amination through Catalyst Design. *J. Am. Chem. Soc.* **2004**, *126*, 15378–15379. (b) Kurokawa, T.; Kim, M.; Du Bois, J. Synthesis of 1,3-Diamines Through Rhodium-Catalyzed C−H Insertion. *Angew. Chemie Int. Ed.* **2009**, *48*, 2777–2779. (c) Lu, H.; Jiang, H.; Wojtas, L.; Zhang, X. P. Selective Intramolecular C−H Amination through the Metalloradical Activation of Azides: Synthesis of 1,3-Diamines under Neutral and Nonoxidative Conditions. *Angew. Chemie Int. Ed.* **2010**, *49*, 10192–10196. (d) Lu, H.; Hu, Y.; Jiang, H.; Wojtas, L.; Zhang, X. P. Stereoselective Radical Amination of Electron-Deficient C(Sp3)–H Bonds by Co(II)-Based Metalloradical Catalysis: Direct Synthesis of α-Amino Acid Derivatives via α-C–H Amination. *Org. Lett.* **2012**, *14*, 5158–5161. (e) Duhamel, T.; Martínez, M. D.; Sideri, I. K.; Muñiz, K. 1,3-Diamine Formation from an Interrupted Hofmann–Löffler Reaction: Iodine Catalyst Turnover through Ritter-Type Amination. *ACS Catal.* **2019**, *9*, 7741–7745. (f) Short, M. A.; Shehata, M.

F.; Sanders, M. A.; Roizen, J. L. Sulfamides Direct Radical-Mediated Chlorination of Aliphatic C–H Bonds. *Chem. Sci.* **2020**, *11*, 217–223.

[106] Lu, H.; Lang, K.; Jiang, H.; Wojtas, L.; Zhang, X. P. Intramolecular 1,5-C(Sp3)–H Radical Amination via Co(Ii)-Based Metalloradical Catalysis for Five-Membered Cyclic Sulfamides. *Chem. Sci.* **2016**, *7*, 6934–6939.

[107] Vorberg, R.; Trapp, N.; Carreira, E. M.; Müller, K. Bicyclo[3.2.0]Heptane as a Core Structure for Conformational Locking of 1,3-Bis-Pharmacophores, Exemplified by GABA. *Chem. – Eur. J.* **2017**, *23*, 3126–3138.

[108] (a) Wheeler, S. E.; Houk, K. N.; Schleyer, P. v. R.; Allen, W. D. A Hierarchy of Homodesmotic Reactions for Thermochemistry. *J. Am. Chem. Soc.* **2009**, *131*, 2547–2560. (b) Bach, R. D. Ring Strain Energy in the Cyclooctyl System. The Effect of Strain Energy on [3 + 2] Cycloaddition Reactions with Azides. *J. Am. Chem. Soc.* **2009**, *131*, 5233–5243. (c) Zhang, X.; Lu, G.; Sun, M.; Mahankali, M.; Ma, Y.; Zhang, M.; Hua, W.; Hu, Y.; Wang, Q.; Chen, J.; He, G.; Qi, X.; Shen, W.; Liu, P.; Chen, G. A General Strategy for Synthesis of Cyclophane-Braced Peptide Macrocycles via Palladium-Catalysed Intramolecular Sp3 C−H Arylation. *Nat. Chem.* **2018**, *10*, 540–548.

[109] Another factor that may impact the catalyst-controlled regioselectivity is whether a mononuclear or dinuclear Ag nitrene is involved in the C–H amination. For example, He *et al.* reported *β*-selective amination of carbamates catalyzed by a dinuclear Ag catalyst (ref. 70c). The more crowded steric environment of the dimeric Ag catalyst may contribute to the *β*-selectivity due to steric effects similar to mononuclear Ag catalysts supported by multidentate ligands.

[110] Ess, D. H.; Nielsen, R. J.; Goddard III, W. A.; Periana, R. A. Transition-State Charge Transfer

Reveals Electrophilic, Ambiphilic, and Nucleophilic Carbon−Hydrogen Bond Activation. *J. Am. Chem. Soc.* **2009**, *131*, 11686–11688.

[111] For Hammett studies of C-H amination via nitrene transfer catalyzed by other transition metal catalysts, see: (a) Fiori, K. W.; Espino, C. G.; Brodsky, B. H.; Du Bois, J. A Mechanistic Analysis of the Rh-Catalyzed Intramolecular C–H Amination Reaction. *Tetrahedron* **2009**, *65*, 3042–3051. (b) Bagchi, V.; Paraskevopoulou, P.; Das, P.; Chi, L.; Wang, Q.; Choudhury, A.; Mathieson, J. S.; Cronin, L.; Pardue, D. B.; Cundari, T. R.; Mitrikas, G.; Sanakis, Y.; Stavropoulos, P. A Versatile Tripodal Cu(I) Reagent for C-N Bond Construction via Nitrene-Transfer Chemistry: Catalytic Perspectives and Mechanistic Insights on C–H Aminations/Amidinations and Olefin Aziridinations. *J. Am. Chem. Soc.* **2014**, *136*, 11362–11381.

[112] For reviews: (a) Reetz, M. T. Laboratory Evolution of Stereoselective Enzymes: A Prolific Source of Catalysts for Asymmetric Reactions. *Angew. Chemie Int. Ed.* **2011**, *50*, 138–174. (b) Bornscheuer, U. T.; Huisman, G. W.; Kazlauskas, R. J.; Lutz, S.; Moore, J. C.; Robins, K. Engineering the Third Wave of Biocatalysis. *Nature* **2012**, *485*, 185–194. (c) Devine, P. N.; Howard, R. M.; Kumar, R.; Thompson, M. P.; Truppo, M. D.; Turner, N. J. Extending the Application of Biocatalysis to Meet the Challenges of Drug Development. *Nat. Rev. Chem.* **2018**, *2*, 409–421. (d) Bornscheuer, U. T.; Hauer, B.; Jaeger, K. E.; Schwaneberg, U. Directed Evolution Empowered Redesign of Natural Proteins for the Sustainable Production of Chemicals and Pharmaceuticals. *Angew. Chem. Int. Ed.* **2019**, *58*, 36–40. (e) Zetzsche, L. E.; Chakrabarty, S.; Narayan, A. R. H. The Transformative Power of Biocatalysis in Convergent Synthesis. *J. Am. Chem. Soc.* **2022**, *144*, 5214–5225.

[113] For reviews: (a) Renata, H.; Wang, Z. J.; Arnold, F. H. Expanding the Enzyme Universe:

Accessing Non-Natural Reactions by Mechanism-Guided Directed Evolution. *Angew. Chemie Int. Ed.* **2015**, *54*, 3351–3367. (b) Leveson-Gower, R. B.; Mayer, C.; Roelfes, G. The Importance of Catalytic Promiscuity for Enzyme Design and Evolution. *Nat. Rev. Chem.* **2019**, *3*, 687–705. (c) Chen, K.; Arnold, F. H. Engineering New Catalytic Activities in Enzymes. *Nat. Catal.* **2020**, *3*, 203–213. (d) Miller, D. C.; Athavale, S. V; Arnold, F. H. Combining Chemistry and Protein Engineering for New-to-Nature Biocatalysis. *Nat. Synth.* **2022**, *1*, 18–23. (e) Klaus, C.; Hammer, S. C. New Catalytic Reactions by Enzyme Engineering. *Trends Chem.* **2022**, *4*, 363–366.

[114] Lu, Y.; Yeung, N.; Sieracki, N.; Marshall, N. M. Design of Functional Metalloproteins. *Nature* **2009**, *460*, 855–862.

[115] (a) Denisov, I. G.; Makris, T. M.; Sligar, S. G.; Schlichting, I. Structure and Chemistry of Cytochrome P450. *Chem. Rev.* **2005**, *105*, 2253–2278. (b) Shaik, S.; Kumar, D.; de Visser, S. P.; Altun, A.; Thiel, W. Theoretical Perspective on the Structure and Mechanism of Cytochrome P450 Enzymes. *Chem. Rev.* **2005**, *105*, 2279–2328. (c) Kovaleva, E. G.; Lipscomb, J. D. Versatility of Biological Non-Heme Fe(II) Centers in Oxygen Activation Reactions. *Nat. Chem. Biol.* **2008**, *4*, 186–193. (d) Poulos, T. L. Heme Enzyme Structure and Function. *Chem. Rev.* **2014**, *114*, 3919–3962.

[116] (a) Banerjee, R. Radical Carbon Skeleton Rearrangements: Catalysis by Coenzyme B12-Dependent Mutases. *Chem. Rev.* **2003**, *103*, 2083–2094. (b) Brown, K. L. Chemistry and Enzymology of Vitamin B12. *Chem. Rev.* **2005**, *105*, 2075–2150.

[117] Solomon, E. I.; Heppner, D. E.; Johnston, E. M.; Ginsbach, J. W.; Cirera, J.; Qayyum, M.; Kieber-Emmons, M. T.; Kjaergaard, C. H.; Hadt, R. G.; Tian, L. Copper Active Sites in Biology. *Chem. Rev.* **2014**, *114*, 3659–3853.

[118] Phillips, I. R.; Shephard, E. A.; Ortiz de Montellano, P. R.: *Cytochrome P450 Protocols*; Humana; Springer: Totowa, N.J.; London, 2013.

[119] For reviews on new-to-nature carbene and nitrene transfer: (a) Brandenberg, O. F.; Fasan, R.; Arnold, F. H. Exploiting and Engineering Hemoproteins for Abiological Carbene and Nitrene Transfer Reactions. *Curr. Opin. Biotechnol.* **2017**, *47*, 102–111. (b) Yang, Y.; Arnold, F. H. Navigating the Unnatural Reaction Space: Directed Evolution of Heme Proteins for Selective Carbene and Nitrene Transfer. *Acc. Chem. Res.* **2021**, *54*, 1209–1225.

[120] (a) Biegasiewicz, K. F.; Cooper, S. J.; Gao, X.; Oblinsky, D. G.; Kim, J. H.; Garfinkle, S. E.; Joyce, L. A.; Sandoval, B. A.; Scholes, G. D.; Hyster, T. K. Photoexcitation of Flavoenzymes Enables a Stereoselective Radical Cyclization. *Science* **2019**, *364*, 1166–1169. (b) Page, C. G.; Cooper, S. J.; Dehovitz, J. S.; Oblinsky, D. G.; Biegasiewicz, K. F.; Antropow, A. H.; Armbrust, K. W.; Ellis, J. M.; Hamann, L. G.; Horn, E. J.; Oberg, K. M.; Scholes, G. D.; Hyster, T. K. Quaternary Charge-Transfer Complex Enables Photoenzymatic Intermolecular Hydroalkylation of Olefins. *J. Am. Chem. Soc.* **2021**, *143*, 97–102. (c) Gao, X.; Turek-Herman, J. R.; Choi, Y. J.; Cohen, R. D.; Hyster, T. K. Photoenzymatic Synthesis of α-Tertiary Amines by Engineered Flavin-Dependent "Ene"-Reductases. *J. Am. Chem. Soc.* **2021**, *143*, 19643–19647. (d) Nicholls, B. T.; Qiao, T.; Hyster, T. K. A Photoenzyme for Challenging Lactam Radical Cyclizations. *Synlett* **2022**, *33*, 1204–1208. (e) Nicholls, B. T.; Oblinsky, D. G.; Kurtoic, S. I.; Grosheva, D.; Ye, Y.; Scholes, G. D.; Hyster, T. K. Engineering a Non-Natural Photoenzyme for Improved Photon Efficiency. *Angew. Chemie Int. Ed.* **2022**, *61*, e202113842. (f) For a review: Ye, Y.; Fu, H.; Hyster, T. K. Activation Modes in Biocatalytic Radical Cyclization Reactions. *J. Ind. Microbiol. Biotechnol.* **2021**, *48*, kuab021.

[121] (a) Huang, X.; Wang, B.; Wang, Y.; Jiang, G.; Feng, J.; Zhao, H. Photoenzymatic

Enantioselective Intermolecular Radical Hydroalkylation. *Nature* **2020**, *584*, 69–74. (b) For a review: Harrison, W.; Huang, X.; Zhao, H. Photobiocatalysis for Abiological Transformations. *Acc. Chem. Res.* **2022**, *55*, 1087–1096.

[122] (a) Su, H.; Ma, G.; Liu, Y. Theoretical Insights into the Mechanism and Stereoselectivity of Olefin Cyclopropanation Catalyzed by Two Engineered Cytochrome P450 Enzymes. *Inorg. Chem.* **2018**, *57*, 11738–11745. (b) Biler, M.; Crean, R. M.; Schweiger, A. K.; Kourist, R.; Kamerlin, S. C. L. Ground-State Destabilization by Active-Site Hydrophobicity Controls the Selectivity of a Cofactor-Free Decarboxylase. *J. Am. Chem. Soc.* **2020**, *142*, 20216–20231. (c) Nakano, Y.; Black, M. J.; Meichan, A. J.; Sandoval, B. A.; Chung, M. M.; Biegasiewicz, K. F.; Zhu, T.; Hyster, T. K. Photoenzymatic Hydrogenation of Heteroaromatic Olefins Using 'Ene'-Reductases with Photoredox Catalysts. *Angew. Chemie Int. Ed.* **2020**, *59*, 10484–10488. (d) Hall, M. Enzymatic Strategies for Asymmetric Synthesis. *RSC Chem. Biol.* **2021**, *2*, 958–989. (e) Coleman, T.; Kirk, A. M.; Chao, R. R.; Podgorski, M. N.; Harbort, J. S.; Churchman, L. R.; Bruning, J. B.; Bernhardt, P. V; Harmer, J. R.; Krenske, E. H.; De Voss, J. J.; Bell, S. G. Understanding the Mechanistic Requirements for Efficient and Stereoselective Alkene Epoxidation by a Cytochrome P450 Enzyme. *ACS Catal.* **2021**, *11*, 1995–2010. (f) Gergel, S.; Soler, J.; Klein, A.; Schülke, K. H.; Hauer, B.; Garcia-Borràs, M.; Hammer, S. C. Directed Evolution of a Ketone Synthase for Efficient and Highly Selective Functionalization of Internal Alkenes by Accessing Reactive Carbocation Intermediates. *ChemRxiv* **2022**. DOI: 10.26434/chemrxiv-2022-dp94p.

[123] For reviews: (a) Sheng, X.; Kazemi, M.; Planas, F.; Himo, F. Modeling Enzymatic Enantioselectivity Using Quantum Chemical Methodology. *ACS Catal.* **2020**, *10*, 6430–6449. (b) Reetz, M. T.; Garcia-Borràs, M. The Unexplored Importance of Fleeting Chiral

Intermediates in Enzyme-Catalyzed Reactions. *J. Am. Chem. Soc.* **2021**, *143*, 14939–14950.

[124] (a) Tang, W.; Jiménez-Osés, G.; Houk, K. N.; van der Donk, W. A. Substrate Control in Stereoselective Lanthionine Biosynthesis. *Nat. Chem.* **2015**, *7*, 57–64. (b) Bauer, P.; Carlsson, Å. J.; Amrein, B. A.; Dobritzsch, D.; Widersten, M.; Kamerlin, S. C. L. Conformational Diversity and Enantioconvergence in Potato Epoxide Hydrolase 1. *Org. Biomol. Chem.* **2016**, *14*, 5639–5651. (c) Sun, Z.; Wu, L.; Bocola, M.; Chan, H. C. S.; Lonsdale, R.; Kong, X.-D.; Yuan, S.; Zhou, J.; Reetz, M. T. Structural and Computational Insight into the Catalytic Mechanism of Limonene Epoxide Hydrolase Mutants in Stereoselective Transformations. *J. Am. Chem. Soc.* **2018**, *140*, 310–318. (d) Sato, M.; Kishimoto, S.; Yokoyama, M.; Jamieson, C. S.; Narita, K.; Maeda, N.; Hara, K.; Hashimoto, H.; Tsunematsu, Y.; Houk, K. N.; Tang, Y.; Watanabe, K. Catalytic Mechanism and Endo-to-Exo Selectivity Reversion of an Octalin-Forming Natural Diels–Alderase. *Nat. Catal.* **2021**, *4*, 223–232. (e) Dong, Y.; Li, T.; Zhang, S.; Sanchis, J.; Yin, H.; Ren, J.; Sheng, X.; Li, G.; Reetz, M. T. Biocatalytic Baeyer–Villiger Reactions: Uncovering the Source of Regioselectivity at Each Evolutionary Stage of a Mutant with Scrutiny of Fleeting Chiral Intermediates. *ACS Catal.* **2022**, *12*, 3669–3680.

[125] For previous computational studies on the roles of active site hydrogen bonding interactions, see: (a) Herschlag, D.; Eckstein, F.; Cech, T. R. The Importance of Being Ribose at the Cleavage Site in the Tetrahymena Ribozyme Reaction. *Biochemistry* **1993**, *32*, 8312–8321. (b) Adalsteinsson, H.; Maulitz, A. H.; Bruice, T. C. Calculation of the Potential Energy Surface for Intermolecular Amide Hydrogen Bonds Using Semiempirical and Ab Initio Methods. *J. Am. Chem. Soc.* **1996**, *118*, 7689–7693. (c) Shan, S.; Herschlag, D. The Change in Hydrogen Bond Strength Accompanying Charge Rearrangement: Implications for Enzymatic Catalysis. *Proc. Natl. Acad. Sci.* **1996**, *93*, 14474–14479. (d) Khade, R. L.; Zhang, Y. Catalytic and

Biocatalytic Iron Porphyrin Carbene Formation: Effects of Binding Mode, Carbene Substituent, Porphyrin Substituent, and Protein Axial Ligand. *J. Am. Chem. Soc.* **2015**, *137*, 7560–7563. (e) Mehmood, R.; Qi, H. W.; Steeves, A. H.; Kulik, H. J. The Protein's Role in Substrate Positioning and Reactivity for Biosynthetic Enzyme Complexes: The Case of SyrB2/SyrB1. *ACS Catal.* **2019**, *9*, 4930–4943. (f) Vennelakanti, V.; Qi, H. W.; Mehmood, R.; Kulik, H. J. When Are Two Hydrogen Bonds Better than One? Accurate First-Principles Models Explain the Balance of Hydrogen Bond Donors and Acceptors Found in Proteins. *Chem. Sci.* **2021**, *12*, 1147–1162. (g) Liu, Z.; Calvó-Tusell, C.; Zhou, A. Z.; Chen, K.; Garcia-Borràs, M.; Arnold, F. H. Dual-Function Enzyme Catalysis for Enantioselective Carbon–Nitrogen Bond Formation. *Nat. Chem.* **2021**, *13*, 1166–1172.

[126] (a) Lee, C.; Yang, W.; Parr, R. G. Development of the Colle-Salvetti Correlation-Energy Formula into a Functional of the Electron Density. *Phys. Rev. B* **1988**, *37*, 785–789. (b) Becke, A. D. Density-Functional Thermochemistry. III. The Role of Exact Exchange. *J. Chem. Phys.* **1993**, *98*, 5648–5652. (c) Grimme, S. Semiempirical GGA-Type Density Functional Constructed with a Long-Range Dispersion Correction. *J. Comput. Chem.* **2006**, *27*, 1787–1799.

[127] Roy, L. E.; Hay, P. J.; Martin, R. L. Revised Basis Sets for the LANL Effective Core Potentials. *J. Chem. Theory Comput.* **2008**, *4*, 1029–1031.

[128] (a) Li, C.; Wu, W.; Cho, K.-B.; Shaik, S. Oxidation of Tertiary Amines by Cytochrome P450—Kinetic Isotope Effect as a Spin-State Reactivity Probe. *Chem. – A Eur. J.* **2009**, *15*, 8492–8503. (b) Usharani, D.; Janardanan, D.; Shaik, S. Does the TauD Enzyme Always Hydroxylate Alkanes, While an Analogous Synthetic Non-Heme Reagent Always Desaturates Them? *J. Am. Chem. Soc.* **2011**, *133*, 176–179.

[129] (a) Sharon, D. A.; Mallick, D.; Wang, B.; Shaik, S. Computation Sheds Insight into Iron Porphyrin Carbenes' Electronic Structure, Formation, and N-H Insertion Reactivity. *J. Am. Chem. Soc.* **2016**, *138*, 9597–9610. (b) Haatveit, K.; Garcia-Borràs, M.; Houk, K. N. Computational Protocol to Understand P450 Mechanisms and Design of Efficient and Selective Biocatalysts. *Front. Chem.* **2019**, 663. (c) D., L. R.; Marc, G.-B.; J., C. M.; R., B. A.; N., H. K.; Jennifer, K. S. B.; H., A. F. Catalytic Iron-Carbene Intermediate Revealed in a Cytochrome c Carbene Transferase. *Proc. Natl. Acad. Sci.* **2018**, *115*, 7308–7313.

[130] (a) Karplus, M.; McCammon, J. A. Molecular Dynamics Simulations of Biomolecules. *Nat. Struct. Biol.* **2002**, *9*, 646–652. (b) Adcock, S. A.; McCammon, J. A. Molecular Dynamics: Survey of Methods for Simulating the Activity of Proteins. *Chem. Rev.* **2006**, *106*, 1589–1615.

[131] Coelho, P. S.; Wang, Z. J.; Ener, M. E.; Baril, S. A.; Kannan, A.; Arnold, F. H.; Brustad, E. M. A Serine-Substituted P450 Catalyzes Highly Efficient Carbene Transfer to Olefins in Vivo. *Nat. Chem. Biol.* **2013**, *9*, 485–487.

[132] *PyMOL Molecular Graphics System*, version 2.0; Schrödinger, LLC, 2017.

[133] Case, D. A.; Aktulga, H. M.; Belfon, K.; Ben-Shalom, I. Y.; Brozell, S. R.; Cerutti, D. S.; Cheatham, T. E.; Cisneros, G.A.; Cruzeiro, V. W. D.; Darden, T. A.; Duke, R. E.; Giambasu, G.; Gilson, M. K.; Gohlke, H.; Goetz, A. W.; Harris, R.; Izadi, S.; Izmailov, S. A.; Jin, C.; Kasavajhala, K.; Kaymak, M. C.; King, E.; Kovalenko, A.; Kurtzman, T.; Lee, T. S.; LeGrand, S.; Li, P.; Lin, C.; Liu, J.; Luchko, T.; Luo, R.; Machado,M.; Man, V.; Manathunga, M.; Merz, K. M.; Miao, Y.; Mikhailovskii, O.; Monard, G.; Nguyen, H.; O'Hearn, K. A.; Onufriev, A.; Pan, F.; Pantano, S.; Qi, R.; Rahnamoun, A.; Roe, D. R.; Roitberg, A.; Sagui, C.; Schott-Verdugo, S.; Shen, J.; Simmerling, C. L.; Skrynnikov, N. R.; Smith, J.; Swails, J.; Walker, R. C.; Wang, J.; Wei, H.; Wolf, R. M.; Wu, X.; Xue, Y.; York, D. M.; Zhao, S.; Kollman, P. A.

AMBER 2020; University of California: San Francisco, 2020.

[134] Li, P.; Merz, K. M. MCPB.Py: A Python Based Metal Center Parameter Builder. *J. Chem. Inf. Model.* **2016**, *56*, 599–604.

[135] Wang, J.; Wolf, R. M.; Caldwell, J. W.; Kollman, P. A.; Case, D. A. Development and Testing of a General Amber Force Field. *J. Comput. Chem.* **2004**, *25*, 1157–1174.

[136] Maier, J. A.; Martinez, C.; Kasavajhala, K.; Wickstrom, L.; Hauser, K. E.; Simmerling, C. ff14SB: Improving the Accuracy of Protein Side Chain and Backbone Parameters from Ff99SB. *J. Chem. Theory Comput.* **2015**, *11*, 3696–3713.

[137] Knapp, B.; Ospina, L.; Deane, C. M. Avoiding False Positive Conclusions in Molecular Simulation: The Importance of Replicas. *J. Chem. Theory Comput.* **2018**, *14*, 6127–6138.

[138] Roe, D. R.; Cheatham, T. E. PTRAJ and CPPTRAJ: Software for Processing and Analysis of Molecular Dynamics Trajectory Data. *J. Chem. Theory Comput.* **2013**, *9*, 3084–3095.

[139] Morris, G. M.; Huey, R.; Lindstrom, W.; Sanner, M. F.; Belew, R. K.; Goodsell, D. S.; Olson, A. J. AutoDock4 and AutoDockTools4: Automated Docking with Selective Receptor Flexibility. *J. Comput. Chem.* **2009**, *30*, 2785–2791.

[140] (a) Knorrscheidt, A.; Soler, J.; Hünecke, N.; Püllmann, P.; Garcia-Borràs, M.; Weissenborn, M. J. Accessing Chemo- and Regioselective Benzylic and Aromatic Oxidations by Protein Engineering of an Unspecific Peroxygenase. *ACS Catal.* **2021**, *11*, 7327–7338. (b) Garcia-Borràs, M.; Kan, S. B. J.; Lewis, R. D.; Tang, A.; Jimenez-Osés, G.; Arnold, F. H.; Houk, K. N. Origin and Control of Chemoselectivity in Cytochrome c Catalyzed Carbene Transfer into Si–H and N–H Bonds. *J. Am. Chem. Soc.* **2021**, *143*, 7114–7123. (c) Soler, J.; Gergel, S.; Hammer, S.; Garcia-Borràs, M. Enzymatic Control Over Reactive Intermediates Enables Direct Oxidation of Alkenes to Carbonyls by a P450 Iron-Oxo Species. *ChemRxiv* **2022**.

DOI: 10.26434/chemrxiv-2022-6lpjf.

[141] Senn, H. M.; Thiel, W. QM/MM Methods for Biomolecular Systems. *Angew. Chem. Int. Ed.* **2009**, *48*, 1198–1229.

[142] Chung, L. W.; Sameera, W. M. C.; Ramozzi, R.; Page, A. J.; Hatanaka, M.; Petrova, G. P.; Harris, T. V.; Li, X.; Ke, Z.; Liu, F.; Li, H.-B.; Ding, L.; Morokuma, K. The ONIOM Method and Its Applications. *Chem. Rev.* **2015**, *115*, 5678–5796.

[143] Vreven, T.; Frisch, M. J.; Kudin, K. N.; Schlegel, H. B.; Morokuma, K. Geometry Optimization with QM/MM Methods II: Explicit Quadratic Coupling. *Mol. Phys.* **2006**, *104*, 701–714.

[144] Lin, H.; Truhlar, D. G. QM/MM: What Have We Learned, Where Are We, and Where Do We Go from Here? *Theor. Chem. Acc.* **2006**, *117*, 185.

[145] Araújo, J. Q.; Carneiro, J. W. de M.; Araujo, M. T. de; Leite, F. H. A.; Taranto, A. G. Interaction between Artemisinin and Heme. A Density Functional Theory Study of Structures and Interaction Energies. *Bioorg. Med. Chem.* **2008**, *16*, 5021–5029.

[146] (a) Laio, A.; VandeVondele, J.; Rothlisberger, U. A Hamiltonian Electrostatic Coupling Scheme for Hybrid Car–Parrinello Molecular Dynamics Simulations. *J. Chem. Phys.* **2002**, *116*, 6941–6947. (b) Laino, T.; Mohamed, F.; Laio, A.; Parrinello, M. An Efficient Real Space Multigrid QM/MM Electrostatic Coupling. *J. Chem. Theory Comput.* **2005**, *1*, 1176–1184.

[147] Becke, A. D. Density-Functional Exchange-Energy Approximation with Correct Asymptotic Behavior. *Phys. Rev. A* **1988**, *38*, 3098–3100.

[148] Yang, Y.; Cho, I.; Qi, X.; Liu, P.; Arnold, F. H. An Enzymatic Platform for the Asymmetric Amination of Primary, Secondary and Tertiary C(Sp3)–H Bonds. *Nat. Chem.* **2019**, *11*, 987–993.

[149] (a) Swart, M. Accurate Spin-State Energies for Iron Complexes. *J. Chem. Theory Comput.* **2008**, *4*, 2057–2066. (b) Radoń, M. Benchmarking Quantum Chemistry Methods for Spin-State Energetics of Iron Complexes against Quantitative Experimental Data. *Phys. Chem. Chem. Phys.* **2019**, *21*, 4854–4870.

[150] (a) Miehlich, B.; Savin, A.; Stoll, H.; Preuss, H. Results Obtained with the Correlation Energy Density Functionals of Becke and Lee, Yang and Parr. *Chem. Phys. Lett.* **1989**, *157*, 200–206. (b) Handy, N. C.; Cohen, A. J. Left-Right Correlation Energy. *Mol. Phys.* **2001**, *99*, 403–412.

[151] Yu, H. S.; He, X.; Li, S. L.; Truhlar, D. G. MN15: A Kohn-Sham Global-Hybrid Exchange-Correlation Density Functional with Broad Accuracy for Multi-Reference and Single-Reference Systems and Noncovalent Interactions. *Chem. Sci.* **2016**, *7*, 5032–5051.

[152] Zhao, Y.; Truhlar, D. G. The M06 Suite of Density Functionals for Main Group Thermochemistry, Thermochemical Kinetics, Noncovalent Interactions, Excited States, and Transition Elements: Two New Functionals and Systematic Testing of Four M06-Class Functionals and 12 Other Functionals. *Theor. Chem. Acc.* **2008**, *120*, 215–241.

[153] Curran, D. P.; Tamine, J. Effects of Temperature on Atom Transfer Cyclization Reactions of Allylic α-Iodo Esters and Amides. *J. Org. Chem.* **1991**, *56*, 2746–2750.

[154] Miller, B. R.; McGee, T. D.; Swails, J. M.; Homeyer, N.; Gohlke, H.; Roitberg, A. E. MMPBSA.Py: An Efficient Program for End-State Free Energy Calculations. *J. Chem. Theory Comput.* **2012**, *8*, 3314–3321.

[155] (a) Tang, W.; Kwak, Y.; Braunecker, W.; Tsarevsky, N. V.; Coote, M. L.; Matyjaszewski, K. Understanding Atom Transfer Radical Polymerization: Effect of Ligand and Initiator Structures on the Equilibrium Constants. *J. Am. Chem. Soc.* **2008**, *130*, 10702–10713. (b) Lin, C. Y.; Coote, M. L.; Gennaro, A.; Matyjaszewski, K. Ab Initio Evaluation of the

Thermodynamic and Electrochemical Properties of Alkyl Halides and Radicals and Their Mechanistic Implications for Atom Transfer Radical Polymerization. *J. Am. Chem. Soc.* **2008**, *130*, 12762−12774.

[156] The HOMO energies of a model Fe–porphine complex and $Cu(TMPA)^+$ (TPMA: tris(2-pyridylmethyl)-amine) were computed at the B3LYP-D3/6-311+G(d,p)-LANL2TZ(f)/SMD(chlorobenzene)//B3LYP-D3/6-31G(d)-LANL2DZ level of theory. See Ref. 10.

[157] For a computational study on the effects of HOMO energy of the transition metal complex on the rate of bromine atom abstraction, see: Fang, C.; Fantin, M.; Pan, X.; de Fiebre, K.; Coote, M. L.; Matyjaszewski, K.; Liu, P. Mechanistically Guided Predictive Models for Ligand and Initiator Effects in Copper-Catalyzed Atom Transfer Radical Polymerization (Cu-ATRP). *J. Am. Chem. Soc.* **2019**, *141*, 7486–7497.

[158] The hydrogen bond distances in the metadynamics trajectories are longer than those in the QM/MM-optimized structures shown in Figures 4-9–4-12, because kinetic and potential energies were added to simulate the reaction at room temperature, whereas the QM/MM geometry optimizations obtain stationary points on the electronic energy surface.